Insights into Crystalline and Material Solids from Ultrafast Magic Angle Spinning NMR Spectroscopy

by

Joshua T. Damron

A dissertation submitted in partial fulfillment
of the requirements for the degree of
Doctor of Philosophy
(Chemistry)
in the University of Michigan
2018

Doctoral Committee:

Professor Ayyalusamy Ramamoorthy, Chair
Professor Charles L. Brooks III
Professor Eitan Geva
Professor Kevin Kubarych
Professor Adam J. Matzger

Joshua T. Damron
jtda@umich.edu
ORCID: 0000-0003-3409-0190

Acknowledgements

First and foremost I would like to thank my advisor Professor Ayyalusamy Ramamoorthy. His advice, encouragement, and leadership has developed me further as a scientist and given me the skills to embark on the next stages of my career. In addition, I would like to thank my committee members professors Adam Matzger, Eitan Geva, Charles Brooks, and Kevin Kubarych for their time, energy, and guidance. I would like to especially acknowledge and thank Dr. Matzger for his role as an extensive collaborator and additional mentorship he provided me throughout my PhD.

A number of collaborators and lab mates were instrumental in the completion of this work. First, I would like to thank Jialiu Ma and Kortney Kersten of the Matzger group who were instrumental in the sample preparation and performing complementary analysis on investigated systems. In addition, I would like to thank Manoj Pandey, Yusuke Nishiyama and the Jeol Riken collaboration center for hosting me and allowing me to complete a number of the fast MAS experiments there. I am grateful to Kay Saalwächter and the expertise of NMR institute at the Martin-Luther Universität for generously hosting me as well and guiding me in the early stages of the MOF experiments. In particular, I would to recognize Ricardo Kurz and Alexey Krushelnitzky for their special involvement.

Many thanks to the members of the Ramamoorthy over the last few years for creating a fun, productive, and intellectually enriching work environment. Special acknowledgements to Rongchun Zhang, Kamal Mroue, and Kazutoshi Yamamoto for their involvement and guidance as the solid-state guys and Dr. Vivek Subramanian for the NMR support at Michigan.

I would like mention the special role of Dr. Jeffery White at Oklahoma State University for introducing me to scientific research and solid-state NMR early on as undergraduate. Also, Dr. Lance Gill for much of the practical training and early mentorship as a NMR spectroscopist.

Of course, I would be nowhere without my parents Drs. Steve and Rebecca Damron. Their constant love, encouragement, and guidance throughout this process has been the same as any other major endeavor in my life and an unquestionable source of strength for me. Also, my little sister Aubry who has always possessed the masterful skill of providing much needed advice and perspective to her older brother. Many people have greatly enriched my time at Michigan. A special thanks to Andy Vitek, Ben Meinen, Alex Burnap, Zach Huttinger, Oliver Scheiner and Manu Schreckenbach for being a part of such a rich and stimulating community of friends. Finally, my wonderful fiancée Alexandra Markel who always challenges me to be better and is constant source of support. Thank you for everything.

Contents

List of Figures

List of Tables

List of Appendices

Abstract

While tremendous progress has been made in the development of tools used to probe the molecular world, a number of shortcoming persist in many of the commonly used techniques highlighting the importance for the development of new approaches for molecular inquiry. For example, X-ray diffraction, which is considered to be the gold standard for probing molecular structure, is limited in its ability to achieve atomic resolution for non-crystalline or heterogeneous systems including intrinsically disordered proteins, amorphous polymers or other multiphase systems. In addition, only limited dynamic information can be obtained by X-ray diffraction. Solution-state Nuclear Magnetic Resonance (NMR) is a complementary technique which can address a number of these issues including the ability to probe dynamics and detect disordered systems with high resolution. However, this requires good solubility of the sample and is limited by molecular size before spectral line-widths become too broad to be detected for slow-tumbling macromolecules. Magic Angle Spinning (MAS) NMR is not bound by the limitation of molecular size, opening up many new avenues for applications including the ability to detect signals from solid or semi-solid systems. Solid-state MAS NMR is a versatile and informative spectroscopy due to the rich and highly manipulable nuclear spin interactions. In contrast to solution NMR, orientation dependent contributions to the spin state are present in solids which reflect structural characteristics at the atomic and molecular levels. While the increased complexity of solid-state systems provides an opportunity for rich insight, challenges do exist in effectively utilizing solid state signals due to severe spectral broadening. The spectral resolution is limited by the MAS frequency, is dependent on the structural heterogeneity of the sample, and varies with the spin physics of the detected nucleus. Indeed,until recently, solid-state NMR spectra have rarely achieved the resolution obtained in solution. Typically, nuclei with lower gyromagnetic ratios (γ) are better resolved under MAS, however, the sensitivity of the detected signal reduces with γ necessitating more data collection to obtain the same signal to noise. This is compounded by the fact that many nuclei of interest have low natural-abundance (e.g. ^{13}C is approximately 1%) either requiring isotopic labeling or extended data acquisition, which is not suitable for many systems or is simply cost prohibitive.

Simultaneously addressing sensitivity and resolution is a major goal in modern solid-state NMR spectroscopy. To this end, recent innovations in MAS technology combined with refined approaches for pulse sequence design have made a substantial impact. The topic of this dissertation focuses on the application of these approaches to crystalline and material systems. The main thrust of the work describes ^{1}H-based techniques under fast MAS frequencies (60-100 kHz). Under these spinning speeds, ^{1}H/^{1}H dipolar couplings are heavily suppressed thereby reducing

spectral broadening and, in many cases, achieving chemical shift resolution to render "solution-like" proton NMR spectra. It is advantageous to detect protons as the large gyromagnetic ratio and near 100% natural-abundance can dramatically reduce the experimental time or the required sample quantity. New approaches utilizing ^{1}H-detected fast MAS are presented and employed in the interrogation of structural differences for crystalline polymorphs and hydrates with a particular focus on ^{1}H chemical shift anisotropy tensors. Valuable insights are gleaned from experimentally measured tensorial NMR parameters reflective of the distinct structural features complementing X-ray data. The inclusion of structured water in hydrate crystals is explored where differences in hydrogen bonding versus kinetic trapping is effectively characterized for mercaptopurine hydrates. In the second part, novel dynamic insights are presented by way of ^{13}C-detected slow MAS approaches in Metal-Organic Frameworks (MOFs). The quantification of ^{13}C-^{1}H heteronuclear dipolar coupling constants is used as proxy for dynamics in microporous structure. This was completed for a series of Zr, terephthalate based MOFs, known as UiO66, with different chemical functionalization on the terephthalate ring. The dynamic evolution of the ring is shown to span several orders of magnitude depending on the nature of the functional group. As demonstrated in this study, the dramatic reduction in the required sample quantity and considerable enhancements in spectral resolution and sensitivity by ultrafast-MAS are bound to enable a plethora of investigations on numerous exciting classes of chemical and biological materials without any constraints on the molecular size and nature of the sample. Therefore, we believe that the methods and results reported in this thesis will be useful for a variety of other systems as well.

Chapter 1

Introduction

Nuclear Magnetic Resonance (NMR) spectroscopy has made important contributions over several decades to many fields of inquiry including medicine, chemistry, biology, physics, material science, and related fields. This is in large part due to the wealth of information which can be obtained in a selective and non-invasive manner by the technique. The "heart" of NMR spectroscopy is the chemical shift, which has been instrumental to chemical and biological sciences in identifying bonding and structure as well as monitoring chemical reactions. In conjunction with the chemical shift, other contributions to the spin Hamiltonian can be utilized to elucidate structure and dynamics at multiple time and length scales to probe atomic and molecular degree of freedoms, global structural rearrangments in macromolecules, inter and intramolecular constraints, and diffusive process. A somewhat different but no less important application of NMR is imaging (MRI), where spin states are encoded with a gradient of energies along spatial directions, which is then utilized to reverse construct 3D images providing *in vivo* mapping of tissue crucial to medicinal science and applications to other fields.

The spectroscopic flexibility of NMR is due to the generous spin Hamiltonian which is permissive to extensive manipulation. Generally, nuclei experience rather weak coupling to their environment translating into long-lived (μs– min.) excited states, which can then be subjected to multiple subsequent manipulations. This enables multidimensional experiments, where specific Hamiltonians of interest can be encoded in various dimensions. As such, endless combinations of experimental design become possible resulting in a rather extensive literature which now boasts some tens of thousands of pulse sequences.

Certain divisions occur under the umbrella of NMR with a major split existing between solution and solid-state NMR. In solution, the anisotropic behavior of the spin interactions is almost completely averaged to isotropic terms due to fast molecular motion and can largely be neglected. This simplifies the spin Hamiltonian and results in narrow spectral lines sufficiently resolved to discern chemical shift offsets and J-couplings of just a few Hz. In solids the internal spin interactions adopt a strong geometric or anisotropic dependence from which bond orientations, nuclear

distances, and electrostatic interactions can be quantified. This provides an additional level of information content, which comes at the cost of increased complexity imposing practical challenges for detection. For example, in typical solids the anisotropic terms are significant sources of line-broadening upwards of kHz to MHz in magnitude. This can be so severe that spectral lines are broadened beyond detection. As such, the trade-off for anisotropic information comes with the loss of distinct chemical shifts or the challenge of obtaining even remotely useful solid-state spectra. The major focus of this dissertation is dedicated to methodology and applications of solid-state NMR to address these very issues and get the best of both worlds.

1.1 Magic Angle Spinning

Perhaps the most important development in the history of solid-state NMR was the advent of approaches that exploit the *magic angle* condition which provides the means to gain chemical shift resolution in solid state spectra. This ushered in a new era of possibilities from a methodological standpoint as well as opening the door to study many new systems. These techniques take advantage of the fact that, to first order, the dominant NMR interactions in the solid state—dipole/dipole, quadrupolar, chemical shift anisotropy—have a geometric dependence of $3cos^2\theta - 1$ where θ is the angle between the external magnetic field B_0 and the axis of alignment relevant to each interaction (e.g. the vector between two spins for dipole/dipole interactions).[1] Setting this term to zero and solving for θ results in 54.7356°, at which the anisotropy completely disappears. The term "Magic Angle" was first coined by Cornelius Gorter at the Ampere congress in Pisa in 1960 to describe this condition [39]. The magic angle condition can be achieved by *spin* manipulations through radio frequency pulses, such as Lee-Goldburg irradiation [63] or multiple pulse trains (WAHUHA [112], Magic Sandwich Echo [88], etc.). Alternatively, one can *spatially* fulfill the condition by means of mechanical rotation of the sample along the magic angle (see Figure 1.2), known as Magic Angle Sample Spinning (MASS often shortened to MAS). The first demonstrations of MAS was shown in work by Andrew and co-workers [6] and independently by Lowe [65]. Each approach has its own advantages and disadvantages. Spin based approaches often require precise pulse calibration and be can highly sensitive to inhomogeneities in the Radio Frequency (RF) circuitry used to excite and detect nuclear spins. Another issue is that if the ^{1}H RF channel is preoccupied with pulses dedicated to meeting the magic angle condition, then it is difficult to use it for other means. That is, if one is interested in obtaining ^{1}H specific information that requires r.f. manipulations away from the magic angle, this becomes rather prohibitive. These techniques also generally come with a scaling factor on the observed magnetization reducing the signal to noise ratio. MAS is not subject to these constraints; however, the major downsides of MAS are that it

[1] Quadrupolar couplings are strong enough that the second order term also which has a different geometric dependence with singularity at 74°. In this case, one actually spin around two axes in a double rotation probe.

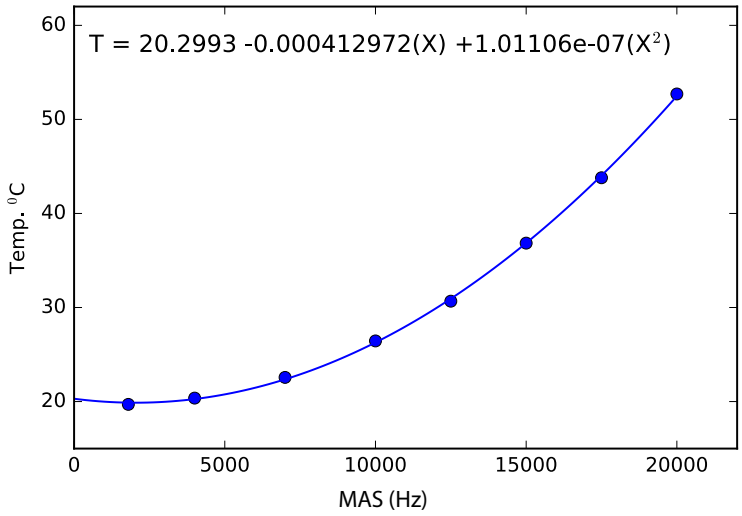

FIGURE 1.1: Sample temperature as a function of MAS rates. The curve was calibrated for the 3.2 mm rotor shown in Figure 1.4 from the chemical shift value of ^{79}Br in a KBr sample according to the procedure by Tycko [105].

requires special equipment (rotors, a spinning probe, good air supply, etc.), mechanical rotation results in substantial centrifugal forces on the sample, and spinning is a significant source of friction causing sample heating. Figure 1.1 shows, for instance, a typical temperature response as a function of MAS speeds on a 3.2 mm Bruker system. One may ask why spinning is required at all, given the downsides. The reason is that there is always a distribution of orientations for the spin interactions in real samples as shown in Figure 1.2. Alignment of the sample at the magic angle macroscopically does not translate to all microscopic orientations of spin interactions within the system. Therefore, for any given sample only some fraction of spin interactions will actually be at the magic angle.[2] As such, there is typically a distribution of vectors, referred to as the powder average—in reference to a "powder" sample with many crystallite orientations. The role of sample rotation about the magic angle is to drive all non-aligned vectors to precess about the symmetry of the magic angle. When spun at sufficiently fast frequencies, defined by the strength of the interaction, the non-aligned orientations appear to collapse to the magic angle condition illustrated by the red ellipses in Figure 1.2. The necessary MAS rates needed to achieve this depends on the type and strength of the interaction involved. For complete averaging of the anisotropic dependence, the spinning rates must theoretically be 3 to 4 times faster than the coupling strength. This is not necessary for most practical applications and often spinning close to or somewhat faster

[2]One can use single crystals and carefully align them in the magnetic field to achieve this but this is tedious and inherently limited to certain types of samples.

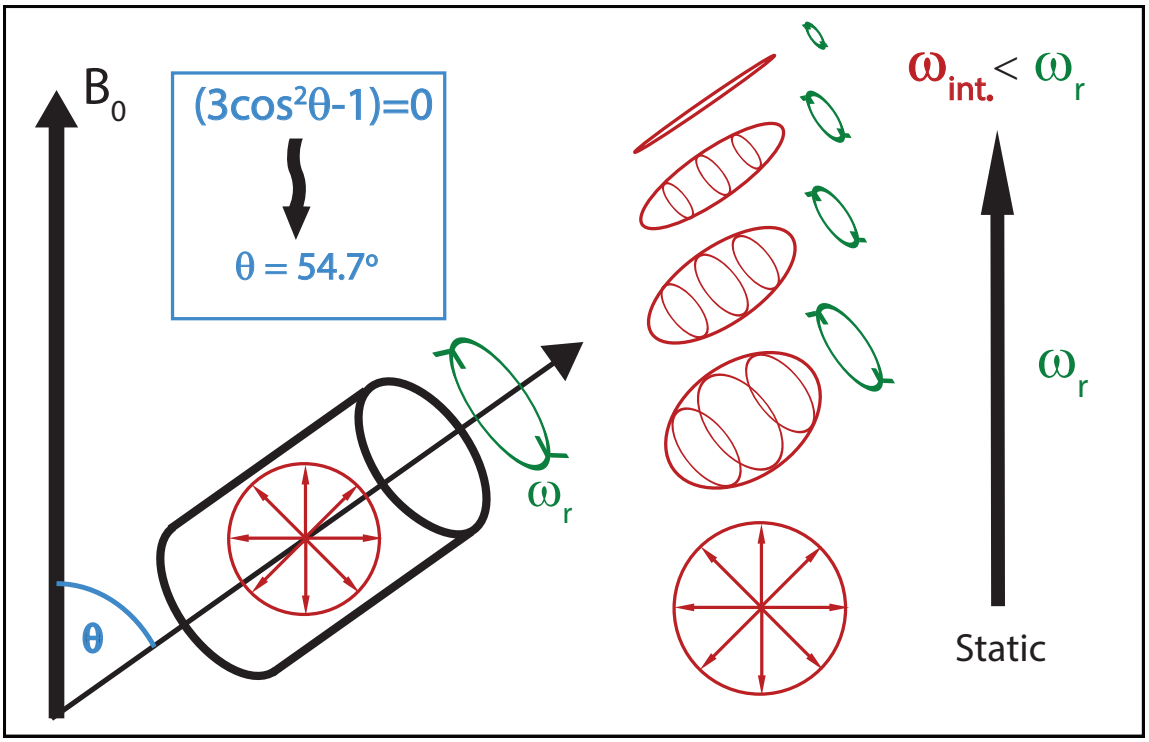

FIGURE 1.2: Depiction of MAS. At the magic angle (θ), the internal interactions (ω_{int}) go to zero. In a powder sample a distribution of interaction orientations are present requiring sample spinning (ω_r), which, when sufficiently fast, effectively collapses the non-oriented vectors to the magic angle. The dominant interactions in the solid state subject to this effect are dipole/dipole interactions, chemical shift anisotropy, and quadrupolar interactions.

than the coupling strength is sufficient for most purposes. On the other hand, slow (relative to the interaction) sampling spinning results in spinning-sidebands at multiples of the spinning frequency ($n\omega_r$) and persistent line-broadening. This is shown in Figure 1.3 for a $^1H/^1H$ spin pair. Typical interaction strengths in rigid solids can range from tens of kHz for heteronuclear dipole interactions between bonded ^1H and ^{13}C or ^{15}N nuclei, to well over 100 kHz for $^1H/^1H$ dipole or quadrupolar interactions. This wide range of possible interaction strengths means rather different spinning speeds are needed for different sample types depending on the rigidity of the molecular structure and chemical species involved. It is important to note that the interaction strengths are almost always scaled to some degree by molecular dynamics, though not to the extent of solution, and can be utilized as a probe for molecular dynamics. This will be demonstrated in Chapter 4. For relatively mobile systems or semi-solids, there may be a substantial reduction requiring much lower MAS rates. In essence, the effect of MAS is to impose a macroscopic manipulation of the sample that serves as a substitute for the role that microscopic molecular motion plays in solution NMR. Principally, MAS could be an even more efficient averaging process than the solution environment at high spinning speeds.

1.2 The Pursuit of Ever Faster Spinning

Hydrogen atoms are abundant and play extremely important roles in many systems, making the detection of ^1H nuclei with chemical shift resolution highly desirable. Beyond this general consideration, a significant practical advantage of ^1H-based NMR is that they possess the largest nuclear gyromagnetic ratios and are close to 100% naturally abundance. This translates into excellent signal-to-noise ratios and can dramatically reduce experimental times by overcoming perhaps the largest handicap to NMR— sensitivity. However, $^1H/^1H$ couplings are dominant in the solid-state which, when combined the relatively narrow CS range, are a major hindrance for resolution. As such, the ^1H dipole interaction has been a major impetus in the pursuit of faster spinning frequencies. Figure 1.3 shows a simulation of a ^1H spin pair situated at a distance of 1Å as a function of spinning speed. The extremely broad line-shape for the static case (bottom left) is just over 100 kHz. For comparison, the typical ^1H chemical shift range is around 20 ppm, which on a 600 MHz spectrometer is 24 kHz. This is even further exasperated by the presence of a network of ^1H spin couplings which is typical of real samples making spin diffusion extremely efficient. In the spin pair case, sample rotation at 100 kHz significantly reduces the broadening; however, even at 150 kHZ small spinning sidebands still persist. The technical challenge of achieving 100+ kHz sample spinning frequencies is far from trivial. For perspective, most cars redline around 8000 rpm or 133 Hz and ultracentrifuges max around 1700 Hz. Spinning capabilities have largely been a technological matter, with tremendous progress being made in the last couple of decades. Currently,

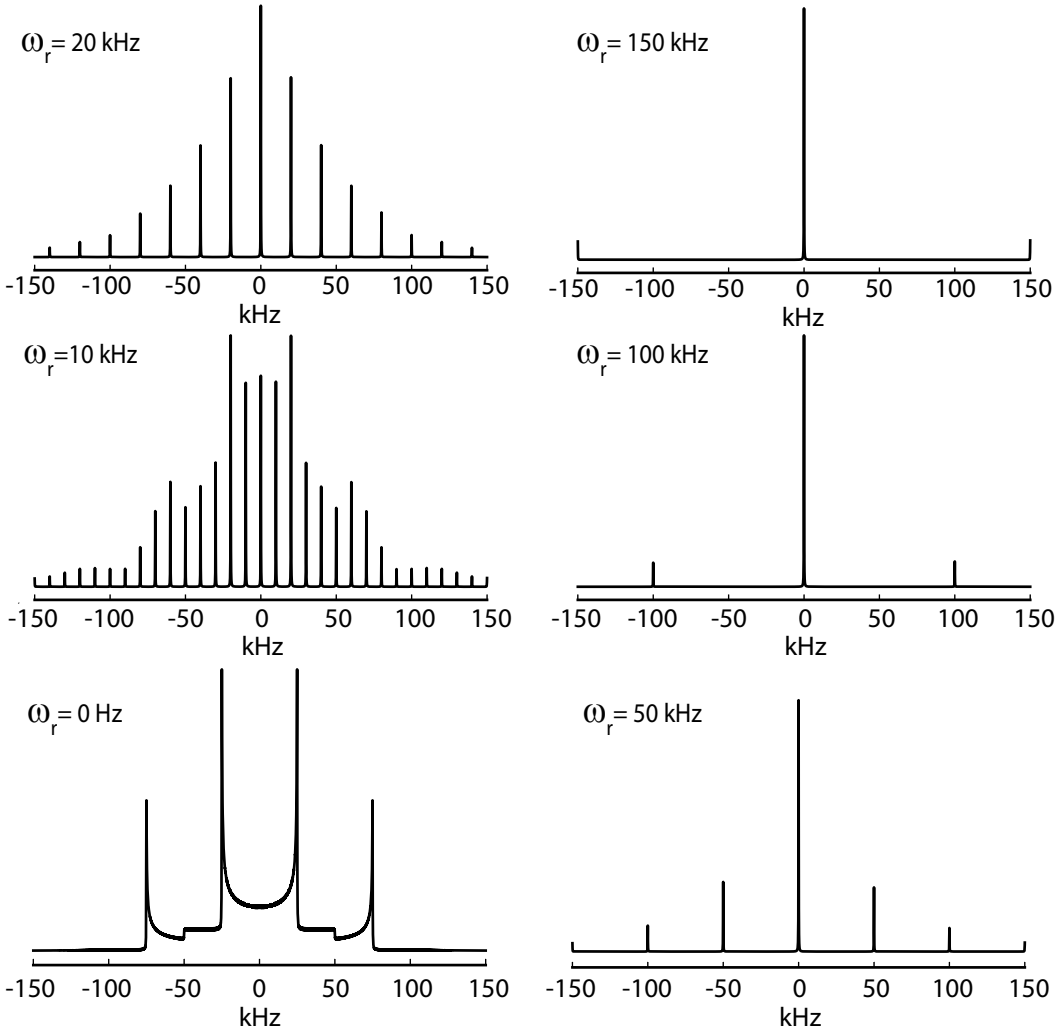

FIGURE 1.3: Numerical simulations of a dipolar Pake-pattern using SIMPSON[8] software for a ^{1}H/^{1}H spin pair as a function of spinning speed ω_r. The simulated interaction strength was set 100 kHz which translates to an internuclear distance of approximately 1 Å. As can be seen, spinning speeds approaching or exceeding the strength of the coupling constant must be used to achieve sharp spectral lines.

FIGURE 1.4: Bruker MAS rotors. The diameters from left to right are: 4 mm, 3.2 mm, 2.5 mm, and 0.7mm. Maximum spinning speeds increase with decreasing rotor sizes. 4 mm rotors typically max around 15 kHz while the 0.7 mm rotor has an upper limit of 111 kHz set by the manufacture. The quarter is included for reference.

commercial probes capable 110 kHz are available[3] and new limits in test probes have reached 150 kHz. This is achieved by spinning a rotor, shown in Figure 1.4, with pressurized air. Bearing axis air pressure is applied to float/lubricate the rotor while a drive pressure is applied to catch the grooved teeth of the cap and rotate the sample. This must be achieved with enough stability not to damage or scrape the radio frequency coil, which is situated to cover the middle portion of the rotor. If any stability does occur, the rotor can crash and cause extensive damage to the coil. The upper limits of spinning are restricted by a number of factors including rotor tensile strength, air friction, centrifugal forces, etc. Estimated maximum speeds at the rotor surface are around 75% the speed of sound [20, 81]. The primary way to increase spinning speeds is to reduce the rotor diameter. Figure 1.4 shows various Bruker rotor designs varying in diameter from standard 4 mm to the latest 0.7 mm rotor. These can achieve maximum spinning rates of approximately 15 to 111 kHz, respectively. Many practical factors including sample packing efficiency, quality of rotor and caps, moisture in spinning air, consistency in air pressure, and probe imperfections can heavily influence the actual achieved rotor rates. Given that the current technology has can achieve speeds on the order of ^{1}H dipolar couplings, this has dramatically improved the situation for ^{1}H NMR in the solid state. It is now possible to achieve atomic resolution in even the most rigid systems [81]. The consequence has been a dramatic surge in the number of ^{1}H-detected methodologies and studies in literature, which span from small crystalline systems to large proteins.

[3]These are cap limits by the producers. On a good day, these probes can reach upwards of 130 kHz for limited experimental times.

1.3 Recoupling

Much is gained by utilizing MAS to average the anisotropic interactions and achieve isotropic chemical shift resolution. However, this too means a loss of the anisotropic terms which are useful for molecular insights. Exploiting both seems inherently incompatible. The solution comes by the way of *recoupling*, an important concept that allows us to "have our cake and eat it too" under MAS. Unlike solution NMR, MAS is a systematic way of mimicking the effect if molecular motion in solution to achieve narrow lines. In solution-state, molecular motion is typically a Brownian process with no chance of reversal. Under MAS the user has control over this process and one can take advantage of the periodic nature of MAS to selectively recouple the spin interactions of interest when desired. Indeed, this can be accomplished by the application of cleverly timed RF pulses with respect to the rotor period. The basic concept is illustrated in Figure 1.5, which demonstrates the basis for REDOR, an early and well-known example of a recoupling sequence. This sequence recouples the heteronuclear dipolar Hamiltonian between two spins I and S coupled by a coupling constant D_{IS}, which is orientation and time-dependent under MAS. A simplified view of D_{IS} under MAS is shown in the left portion of the Figure 1.5. Over the rotor period, the interaction runs through all orientations about the rotor axis symmetry. When $\omega_r >> \omega_{int.}$ the local interaction goes to zero.[4] The spin part of the Hamiltonian $I_z S_z$ can be independently manipulated by RF pulses, represented by the vector picture model in the right portion of the figure. Bulk magnetization starts at equilibrium along the external magnetic field B_0 or Z axis. The application of RF π-pulse flips the sign of the Hamiltonian when applied to only one of the nuclei (I_z in the figure). If the π pulse is placed in the middle of the rotor period $\tau_r/2$, it changes the sign of the Hamiltonian as the symmetry of the geometric portion $D_{IS}(\theta, \omega_r, t)$ is also reflected by sample rotation. The combined effect results in a non-zero heteronuclear interaction over a full rotor period depicted in bottom left corner.

The example illustrates the basic idea for any recoupling sequence under MAS: by utilizing the periodicity of MAS and applying RF pulses with specific timings, the Hamiltonian of interest can be selectively re-introduced. In practice, one often uses a time-period t_1 during the pulse sequence to encode the recoupled interaction and then a detection period t_2 with the usual free induction decay expressing the chemical shift. One can then increment t_1 and detect of series of FIDs which now encode the recoupled Hamiltonian. Taking the Fourier transform in t_1 and t_2 will then correlate the isotropic chemical in one dimension with the anisotropic interaction in the other. In this way, the anisotropic dependence is recovered without loss of atomic resolution. Due to the $1/r^3$ mutual distance dependence of dipole/dipole interaction, REDOR has been used extensively to measure internuclear distances. There are many recoupling sequences and variations in the literature including RFDR, USEME, DRAMA, DRAWS, SEDOR, REDOR, ODESSA, BABA, just to name a few.

[4] A detailed account of the time and orientation dependence under MAS is given in Chapter 2

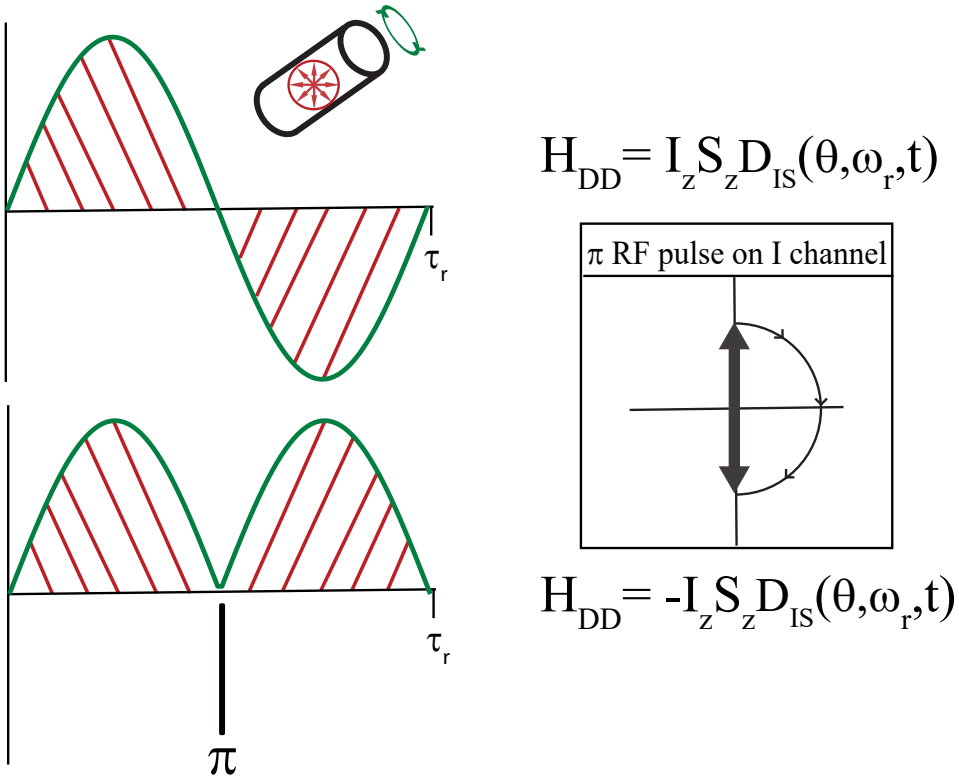

FIGURE 1.5: Illustration of Recoupling sequence for the heteronuclear dipolar coupling Hamiltonian H_{DD} between I and S and spins (e.g. ^{1}H and ^{13}C.)

Central to the effeciveness of recoupling is the use of symmetry with regard to the geometric and spin portion of the Hamiltonian under MAS. The evaluation of recoupling based on symmetry principles was formalized by Malcolm Levitt and co-workers [64]. Levitt proposed a framework, known as symmetry-based recoupling, to generate any pulse sequence from first principles by casting the spin and spatial portions of into irreducible spherical tensor operators and spherical tensor functions, respectively. The advantage is that the terms of the Hamiltonian are sorted into groups which have the same symmetry under rotations, convenient for MAS. Based on the selection rules and the symmetry numbers of the pulse sequence, the rational design of pulse sequences can be performed. In Chapter 3 one such sequence is employed to measure the ^{1}H Chemical Shift Anisotropy (CSA) in small molecule polymorphs and hydrates.

1.4 Outline for the Remainder of the Dissertation

The remainder of the dissertation will explore different applications of magic angle spinning NMR. In Chapter 2, a more rigorous treatment of the time and geometric dependence of Hamiltonians under MAS is presented. Chapter 3 is concerned with ^{1}H-detected fast MAS NMR. Most of the experiments presented were done between 60 and 90 kHz MAS and focused on applications to polymorphs of acetaminophen and hydrates of mercaptopurine. A slightly different use of MAS is shown in Chapter 4, where slow MAS is utilized for dynamic measures in a series of Metal Organic Frameworks.

Chapter 2

Theoretical Background

2.1 Time-Dependent Hamiltonians

The following gives a brief description of the theoretical background with a focus on interactions under MAS. Excellent treatments of the basic foundations presented here can be found in the books of Ernst, Bodenhausen, and Wokaun [26], Gerstein and Dybowski [33], and Abragam [1]. The MAS specific derivations can be found in the books of Duer [25], Spiess and Schmidt-Rohr [94]. Mehring's book [70] is also an excellent resource on the foundations of solid-state NMR.

The time evolution of the density operator ρ is given by the Liouville-von Neumann equation [26]:

$$\frac{d\hat{\rho}}{dt} = -i[\hat{H}, \hat{\rho}]$$

. For a time-independent Hamiltonian the solution is:

$$\hat{\rho}(t) = e^{-i\hat{H}t}\hat{\rho}(0)e^{i\hat{H}t} \tag{2.1}$$

where the exponential is referred to as the time propagator. For a time-dependent Hamiltonian the integral of the Hamiltonian over the relevant time period must be accounted for:

$$\hat{\rho}(t) = Te^{-i\int_0^{t'}\hat{H}(t')dt}\hat{\rho(0)}e^{i\int_0^{t}\hat{H}(t)dt'} \tag{2.2}$$

And T is the Dyson ordering parameter which is needed when $\hat{H}(t)$ does not commute with itself at different time points. For any general observable operator A the expectation value is given by:

$$A = Tr(A\rho(t))$$

Consider when $\rho(0) = \hat{I}_x$. When $\hat{I}_x$ is subject to the chemical shift and in an external magnetic field B_0 the Hamiltonian is given by

$$\hat{H} = \hat{H}_0 + \hat{H}_{CS} = \omega_0(1 - C_{zz})\hat{I}_z \tag{2.3}$$

The chemical shift frequency being defined by $\omega_{CS} = \omega_0(1 - C_{zz})$ where C_{zz} is the secular chemical shift tensor. Evaluating Eqn 2.1 requires an expansion of the exponential operators into the time evolution or Baker-Campbell-Hausdorff series from which the real and imaginary components can often be recombined into geometric functions sine and cosine [33]. For the simple case given here this gives:

$$\hat{\rho}(t) = \hat{I}_x cos(\omega_{CS}t) + \hat{I}_y sin(\omega_{CS}t) \tag{2.4}$$

Which is the quantum mechanical analogue of the Bloch equations. The time-dependence of the signals are thus encoded by the Hamiltonian. The difficulty of calculating the action of the pulse sequence depends strongly on complexity of the Hamiltonian. Let's now consider the situation in solid-state NMR where tensorial interactions need to be considered.

2.2 Solid-State Hamiltonians in NMR

In contrast to solution-state NMR, the internal interactions of the nucleus exhibit a geometric dependence or anisotropy in solid samples. These interactions can be represented by 2nd rank tensors and the Hamiltonians take the general form of [70]:

$$\hat{\mathcal{H}} = \mathbf{I} \cdot \tilde{\mathbf{A}} \cdot \mathbf{S} = \begin{pmatrix} I_x & I_y & I_z \end{pmatrix} \begin{pmatrix} A_{xx} & A_{xy} & A_{xz} \\ A_{yx} & A_{yy} & A_{yz} \\ A_{zx} & A_{zy} & A_{zz} \end{pmatrix} \begin{pmatrix} S_x \\ S_y \\ S_z \end{pmatrix}$$

where the tensor $\tilde{\mathbf{A}}$ captures the spatial portion of the interaction. The chemical shielding tensor, for instance, can be written as $\hat{\mathcal{H}} = \gamma \mathbf{I_z} \cdot \tilde{\mathbf{C}} \cdot \mathbf{B_o}$ for some spin $\mathbf{I}$ in the external magnetic field $\mathbf{B_0}$ where only the Z-component contributes $\mathbf{B_0} = [0, 0, B_0]$ known as the secular approximation. The chemical shift tensor $\tilde{\mathbf{C}}$ can be decomposed into a symmetric tensor[1] and cast into a diagonal coordinate frame known as the principal axes system $\mathbf{C} \Rightarrow \mathbf{C}^{PAS}$. In this frame, the frequency of the chemical shift ω can be computed as:

$$\omega = -\omega_0 \, \mathbf{b_0^{PAS}} \cdot \tilde{\mathbf{C}}^{\mathbf{PAS}} \cdot \mathbf{b_0^{PAS}} \tag{2.5}$$

[1] The asymmetric components do not contribute to the signal.

Or written explicitly as:

$$\begin{pmatrix} cos\phi sin\theta & sin\phi sin\theta & cos\theta \end{pmatrix} \begin{pmatrix} \delta_{xx} & 0 & 0 \\ 0 & \delta_{yy} & 0 \\ 0 & 0 & \delta_{zz} \end{pmatrix} \begin{pmatrix} cos\phi sin\theta \\ sin\phi sin\theta \\ cos\theta \end{pmatrix}$$

where $\mathbf{b_0^{PAS}}$ expresses the $\mathbf{B_0}$ direction in the **PAS**. It is common convention to define the asymmetry parameter $\eta = (\delta_{yy} - \delta_{xx})/\delta$ and the anisotropy $\delta = \delta_{zz} - \delta_{iso}$ with $|\delta_{zz} - \delta_{iso}| \geq |\delta_{xx} - \delta_{iso}| \geq |\delta_{yy} - \delta_{iso}|$ and δ_{iso} equaling the trace of the tensor. We will now discuss the role of MAS on the chemical shift anisotropy tensor.

2.3 Magic Angle Spinning

To account for sample rotation around the magic angle, we must consider the form of the time evolution propagator $e^{i\omega t}$ under MAS [69, 94]. The frequency component ω adopts a time dependence due to the geometric modulation of the internal interactions:

$$e^{i\int_0^{t'} \omega(t')dt'} \tag{2.6}$$

The encoding of the time-dependence is conveniently represented in the *rotor frame*, which is given by the assuming $\tilde{\mathbf{Z}}_R$ along the rotor axis set at 54.7° from the external magnetic field B_0. A rotation from the laboratory frame of reference, B_0 to the rotor frame of reference is given by:

$$\mathbf{b_0^R}(t) = \begin{pmatrix} sin\theta cos\omega_r t \\ sin\theta sin\omega_r t \\ cos\theta \end{pmatrix} \tag{2.7}$$

analogous to our transformation in the **PAS** introduced above. This takes the components of the lab frame into to the rotor frame where only the x and y components in the rotor frame exhibit a time-dependence (i.e. θ is constant in time). When $\theta = 54.7°$ this simplifies to:

$$\tilde{\mathbf{b}}_{\mathbf{0}}^{R}(t) = \sqrt{\frac{2}{3}} \begin{pmatrix} cos\omega_r t \\ sin\omega_r t \\ \frac{1}{\sqrt{2}} \end{pmatrix}$$

Now consider the the chemical shielding tensor $\tilde{\mathbf{C}}$ in the rotor frame, the frequency adopts a time-dependence and can be calculated by evaluating an expression similar to equation 2.5:

$$\omega(t) = \gamma\, B_0\, \mathbf{b_0^R}(\mathbf{t})\tilde{\mathbf{C}}^{\mathbf{R}}\mathbf{b_0^R}(\mathbf{t}) \tag{2.8}$$

Using the principal components of chemical shift tensor δ_{xx}, δ_{yy}, δ_{zz} with the definition of the isotropic chemical shift $\delta_{iso} = \frac{1}{3}[\delta_{xx} + \delta_{yy} + \delta_{zz}]$ Eqn. 2.8 becomes:

$$\omega(t) = -\omega_0\Big[\delta_{iso} + \frac{1}{2}(3cos^2\theta - 1)(\delta^R_{zz} - \delta_{iso}) + sin^2\theta\Big(\frac{1}{2}(\delta^R_{xx} - \delta^R_{yy})cos(\omega_r t) + \delta^R_{xy}sin(\omega_r t)\Big) \\ +2sin\theta cos\theta(\delta^R_{xz}cos(\omega_r t) + \delta^R_{yz}sin(\omega_r t)\Big]$$

Aligning θ at the magic angle further simplifies the expression to:

$$\omega(t) = -\delta_{iso} + \frac{2}{3}\Big(\frac{1}{2}(\delta^R_{xx} - \delta^R_{yy})cos(\omega_r t) + \delta^R_{xy}sin(\omega_r t)\Big) + \sqrt{2}\Big(\delta^R_{xz}cos(\omega_r t) + \delta^R_{yz}sin(\omega_r t)\Big)$$

At fast ω_r the anisotropic terms contribute very little to the spectrum and we regain only the isotropic chemical shift. At intermediate or slow spinning frequencies, we see how the chemical shift frequency is weighted by terms dependent on the spinning frequency and the anisotropy. This is the source of the spinning sidebands seen in MAS spectra. This can be used in Eqn. 2.6 to evaluate the time-depedence according to Eqn. 2.2. Components aligned along Z^R have no time-dependence with MAS.

2.3.1 Euler Angles

Thus far, we have considered a single orientation of a chemical shift tensor, which we arbitrarily aligned along the rotor axis. As mentioned in the introduction, this is not general for actual solid samples. That is, there is always a distribution of angles that must taken into account. This can be done by encoding the geometric relation between the rotor frame and any arbitrary orientation of the principal axes of the chemical shift. This is achieved by employing the Euler rotation matrices. Any rotation in 3D dimension space, be it passive or active, can be performed by the operation of rotations matrices through the so called Euler angles, $\alpha,\ \beta, \gamma$. The procedure is to first complete a rotation about the Z axis by angle α, followed by a second rotation by angle β about the Y axis, and finally a third about about Z again through γ. These rotations get used quite often in NMR when going from the molecular to the rotating frame. To rotate a Cartesian tensor $T(x, y, z)$, which can describe physical quantity including the chemical shift or the dipolar coupling, into another frame $T(X, Y, Z)$ (say molecular frame) we then perform the operation $T(X, Y, Z) = R^{-1}T(x, y, z)R$ with $R = R_Z(\alpha)R_Y(\beta)R_Z(\gamma)$. The explicit operations are defined as by rotations about Z axis:

$$R_z(\gamma) = \begin{pmatrix} \cos\gamma & -sin\gamma & 0 \\ sin\gamma & cos\gamma & 0 \\ 0 & 0 & 1 \end{pmatrix}$$

Rotations about Y axis:

$$R_y(\beta) = \begin{pmatrix} cos\beta & 0 & sin\beta \\ 0 & 1 & 0 \\ -sin\beta & 0 & cos\beta \end{pmatrix}$$

Rotations about Z again:

$$R_z(\gamma) = \begin{pmatrix} \cos\alpha & -sin\alpha & 0 \\ sin\alpha & cos\alpha & 0 \\ 0 & 0 & 1 \end{pmatrix}$$

For the chemical tensor we can then write:

$$\tilde{\mathbf{C}}^{\mathbf{R}} = \tilde{\mathbf{R}}(\alpha,\beta,\gamma)\tilde{\mathbf{C}}^{\mathbf{PAS}}\tilde{\mathbf{R}}^{-\mathbf{1}}(\alpha,\beta,\gamma) \tag{2.9}$$

After evaluating the Euler rotation matrices a general expression for the measured frequency accounting for any given orientation defined by the Euler angles:

$$\begin{aligned} \omega(\alpha,\beta,\gamma,t) = C_1 cos(\gamma+\omega_r t) + C_2 cos(2\gamma+2\omega_r t) \\ + S_1 sin(\gamma+\omega_r t) + S_2 sin(2\gamma+2\omega_r t) \end{aligned} \tag{2.10}$$

The coefficients C_i and S_i are given in Table 2.1.

TABLE 2.1: Coefficients describing the relationship between the rotor frame of reference to the principal axis system.

$C_1(\alpha,\beta) = -\delta\sqrt{2}\frac{1}{2}sin2\beta(1+\frac{1}{3}\eta cos2\alpha)$
$C_2(\alpha,\beta) = \delta\left[\frac{1}{2}sin^2\beta - \frac{1}{6}\eta(1+cos^2\beta)cos2\alpha\right]$
$S_1 = \delta\eta\frac{1}{3}\sqrt{2}sin\beta sin2\alpha$
$S_2 = \delta\eta\frac{1}{3}cos\beta\sin 2\alpha$

Notice how the γ angle is the only Euler angle that enters into the time-dependence. This differentiates between two major classes of γ or non γ-encoded recoupling sequences, which we will encounter later. With the above results we are now set to calculate the free induction decay $g(t)$ of a signal modulated by the chemical shift tensor under MAS:

$$g(t) = \frac{1}{8\pi^2}\int_0^{2\pi}\int_0^{\pi}\int_0^{2\pi} exp(\Phi)sin\beta d\alpha d\beta d\gamma$$

where Φ is the phase accumulated by the signal according to $\omega(t)$ from equation 2.10.

$$\Phi = \int_0^t \omega(\alpha,\beta,\gamma,t)dt$$

In practice, one numerically enumerates through a series of Euler angles to compute spectrum.

A very similar analysis is applicable to the heteronuclear dipolar coupling [25]. We'll consider this case now and derive the fitting function used for the DIPSHIFT experiments encountered in Chapter 4. Keeping the real portion of the signal function $g(t)$, it is common to write the evolution of the signal in a normalized fashion as such [94]:

$$\frac{I(t_1)}{I(0)} = \langle cos\ \Phi \rangle_{\alpha,\beta,\gamma} \tag{2.11}$$

where $I(t)$ is the signal intensity and Φ is the phase acquired during over the rotor period t which is powder averaged over the Euler angles α, β, γ as discussed above. Here we consider the evolution under the heteronuclear dipolar coupling and the phase can be calculated assuming the *interaction frame* of the Hamiltonian by:

$$\Phi = \int_0^{t_1} D_{zz}^{LF}(t)dt$$

Where $D_{zz}^{LF}(t)$ is the ZZ component of the dipolar tensor in the lab frame. We can provide the same analysis as we did before with the chemical shift except that $\hat{\mathcal{H}}_{DD}$ is axially symmetric ($\delta_{xx} = \delta_{yy}$):

$$\tilde{\mathbf{D}} = d_{IS} \begin{pmatrix} 1/2 & 0 & 0 \\ 0 & -1/2 & 0 \\ 0 & 0 & 1 \end{pmatrix}$$

This means that the coefficients $S_1, S_2 = 0$ in Table 2.1, simplifying Eqn. 2.5. The dipolar tensor under MAS is then given by:

$$D_{zz} = d_{IS}\Big[-\frac{1}{\sqrt{2}} sin(2\beta) cos(\omega_r t + \gamma) + \frac{1}{2} sin^2(\beta) cos(2\omega_r + 2\gamma))\Big]$$

Again, β and γ and $\omega_r t$ are Euler angles between the laboratory and rotor frame, where now the time-dependence of spinning is taken into account with the spinning frequency ω_r, and d_{IS} is the dipolar coupling constant given by $d_{IS} = -\big(\frac{\mu_0}{4\pi}\big)\big(\frac{\gamma_I \gamma_S \hbar}{r^3}\big)$ for I and S spin separated by distance r. This can be used to evaluate the phase in Eqn 2.11 Φ:

$$\Phi = d_{IS}\Big[-\frac{1}{\sqrt{2}} sin(2\beta) \int_0^{t_1} cos(\omega_r t + \gamma)dt + \frac{1}{2} sin^2(\beta) \int_0^{t_1} cos(2\omega_r + 2\gamma)dt)\Big]$$

coming to:

$$D_{zz} = d_{IS}\Big[-\frac{1}{\sqrt{2}} sin(2\beta)(sin(\omega_r t_1 + \gamma) - sin(\gamma)) + \frac{1}{2} sin^2(\beta)(sin(2\omega_r t_1 + 2\gamma) - sin(2\gamma)))\Big]$$

This defines the fitting function found in the main text of Chapter 4 for the evolution of the heteronuclear dipolar coupling between a CH spin pair is given by:

$$cos\Big[d_{IS}\Big[-\frac{1}{\sqrt{2}}sin(2\beta)(sin(\omega_r t_1+\gamma)-sin(\gamma))+\frac{1}{2}sin^2(\beta)(sin(2\omega_r t_1+2\gamma)-sin(2\gamma))\Big]\Big]$$

Here we replaced $t \rightarrow t_1$ as t_1 is the indirect dimension of the DIPSHIFT experiment. After proper integration over the Euler Angles, we can use this function to extract the dipolar coupling constants.

Chapter 3

^{1}H NMR under Fast MAS

Portions of this chapter were adapted from the following publications:[1]
Damron, J.T. Kersten, K.M. Pandey, M., Nishiyama, Y., Matzger, A.J., Ramamoorthy, A. Role of Anomalous Water constraints in the Efficacy of Pharmaceutical probed by ^{1}H/^{1}H Solid-State NMR. *ChemistrySelect*, 6797-6800 (2017).
Damron, J.T. Kersten, K.M. Pandey, M., Mroue, K.H., Yarava, J.R., Nishiyama, Y., Matzger, A.J., Ramamoorthy, A. Electrostatic Constraints Assessed by ^{1}H/^{1}H MAS NMR Illuminate Differences in Crystalline Polymorphs. *J. Chem. Phys. Lett.* (2017).

As a primer for ^1H detected fast MAS, consider the ^{1}H spectra collected for several crystalline hydrates under 60 kHz MAS shown Figure 3.1. While the spectral linewidths are far form solution-like, a number of chemical features can actually be distinguished in the spectra. Given the relatively low MAS rates (by current standards) the resolution is expected to increase at higher spinning frequencies. This is not, however, always the case. An issue with crystalline solids is that there can additional source of line-broadening that can't be "spun out." This is due to an anisotropy in the magnetic susceptibility, leading to a source of inhomogeous line-broadening [81]. Indeed, for mercaptopurine (the top two spectra) and acetaminophen (*vide infra*) there isn't a significant increase in resolution under 90 kHZ MAS. We may then need to use other "tricks" edit these such spectra, which we will see in the following section.

3.1 RFDR HMQC

Proton detection greatly enhances sensitivity and dramatically reduces experimental times; however, for rigid systems the presence of extremely long T1s under ultrafast MAS speeds can occur. For instance, for the mercaptopurine hydrates shown in Figure 3.1, the average T1 relaxation time

[1]Contributions: Damron, Ramamoorthy, Kersten, and Matzger contributed to the writing of the manuscript. Kersten and Matzger were responsible for sample synthesis and characterization. Damron, Pandey, and Nishiyama performed and analyzed the NMR experiments. Mroue and Yarava aided in the NMR DFT calculations

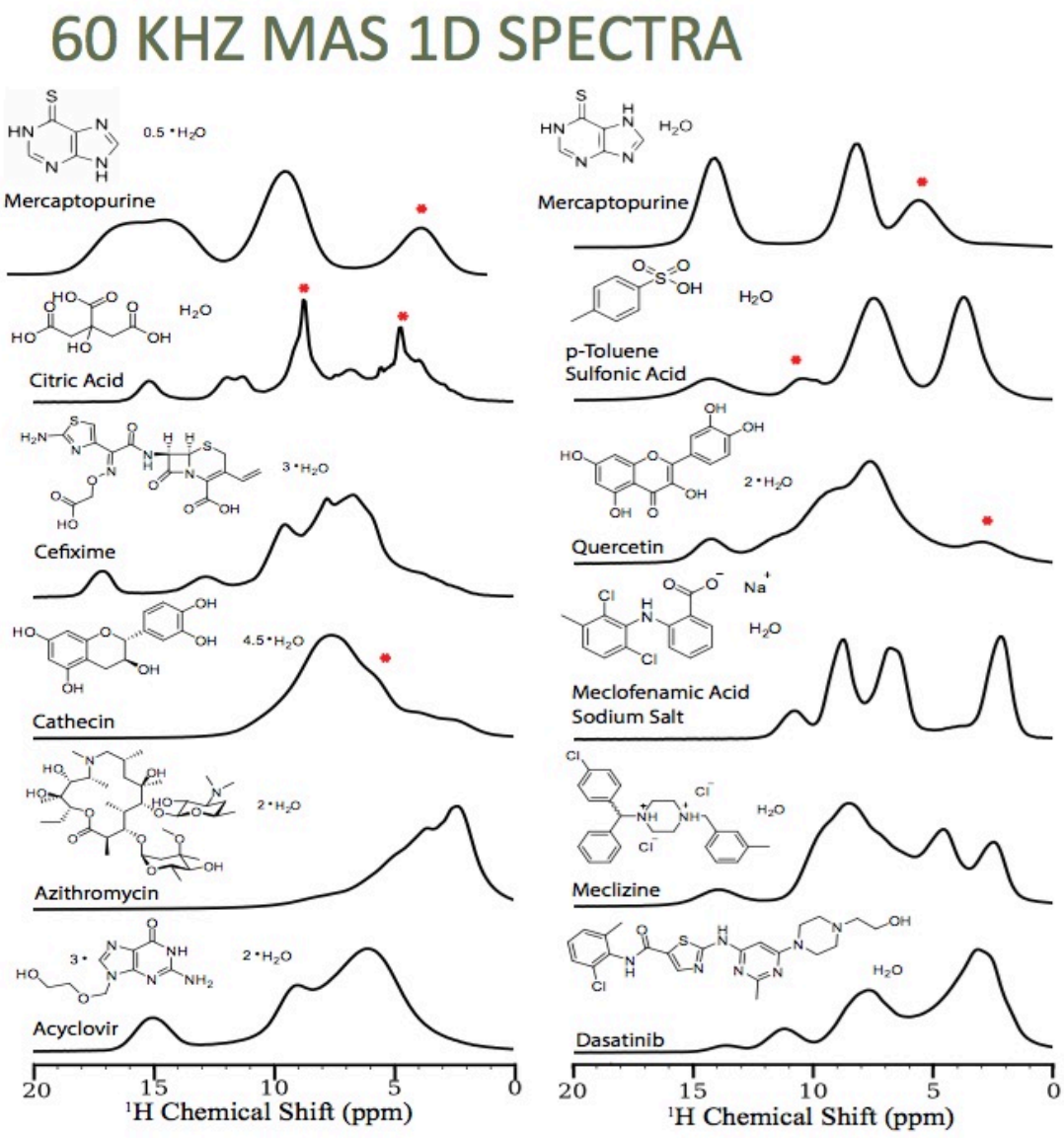

FIGURE 3.1: ^{1}H 1D spin echo spectra under 60 kHz MAS. All specra were collected on a Varian 600 MHz instrument using a 1.2 mm probe. The asterix denotes possible water assignments based on substantially different T_1 relaxation times compared to other resonances.

is around 120s. This is also the case for the monoclinic and orthorhombic polymorphs of acetaminophen. These long T_1 times makes performing multidimensional experiments rather difficult. In addition, challenges persist including inhomogeneous broadening due to anisotropic magnetic susceptibility– particularly relevant to highly periodic systems of small molecules– which limits the effectiveness of ever faster spinning. The deleterious effects of extensive spin diffusion in abundantly populated ^1H systems (spin diffusion, multi-spin couplings, etc.) makes the interpretation of $^1H/^1H$ correlation experiments difficult in practice. These issues motivate the development of additional strategies to simplify proton spectra under ultrafast MAS which could enhance the utility of $^1H/^1H$ correlation experiments for molecular elucidation. The potential use of the ^{14}N nucleus to facilitate this has certain advantages including high natural abundance in addition to being prevalent in a number of important systems. It is then feasible to exploit HMQC based transfer between ^14N and ^1H, which is driven through-bond J-coupling and through-space Dipolar Residual Splittings (DSRs). The approach can also be used to simplify ^{1}H spectra through HMQC magnetization transfer via the abundant ^{14}N nucleus and achieve subsequent correlation thereafter. The simplifies the initial magnetization to ^1H resonances directly bonded to ^{14}N, after which, a spin diffusion block (such as RFDR) can provide information on atomic proximity in a straight-forward manner.

The pulse sequence shown below can achieve this goal. In the initial excitation and reconversion period, ^{1}H magnetization is transferred using HMQC via J-couplings and residual dipolar splittings (RDS). The optimization of efficient transfer must be done empirically as it is hard to know *a priori* the magnitude of both the J-coupling and RDS, simultaneously. After excitation and reconversion, proton magnetization evolves under longitudinal magnetization exchange with enhanced spin diffusion facilitated by fp-RFDR. The rotor synchronized RFDR mixing times can be repeated to extend the time of spin diffusion. After exchange, ^{1}H magnetization is then detected in t_2 preceded by an echo to refocus incoherent background contributions.

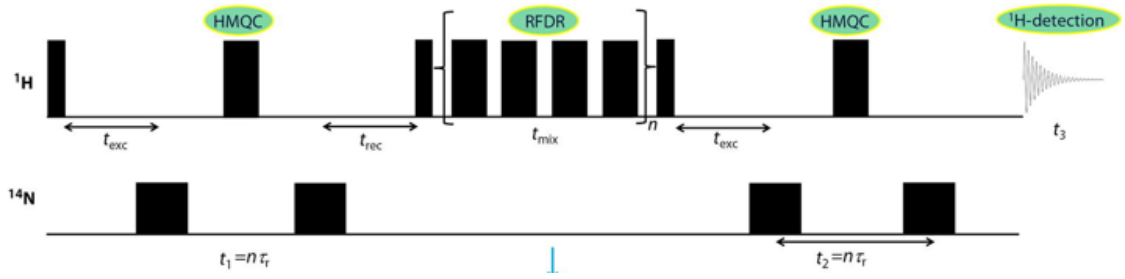

Comparisons of the zero and long mixing times in the bottom left spectrum of Figure 3.2 allows one to assign the emerging downfield peak to the OH resonance at 9.3 ppm for both polymorphs. Due to the severe overlap of the resonances this is difficult to discern otherwise. While chemical

shift behavior of acetaminophen is discussed in detail in the next section, it is noted that this contributed to the resonance assignments made there. By observing which peaks fill in as a function of RFDR mixing time one can make qualitative assessments about the structure. The identity for instance, of the nearest aromatic neighbor to the NH position in acetaminophen (see Figure 3.9) occurs at 5 ppm for the monoclinic and 7 ppm for the orthorhombic. The bottom left spectra, demonstrates a similar utility for the monohydrate form of mercaptopurine (see Figure 3.4). The clear difference in rate of growth for the peak at around 8 ppm confirms the assignment of aromatic group while the most upfield peak belongs to the water (*vide infra*).

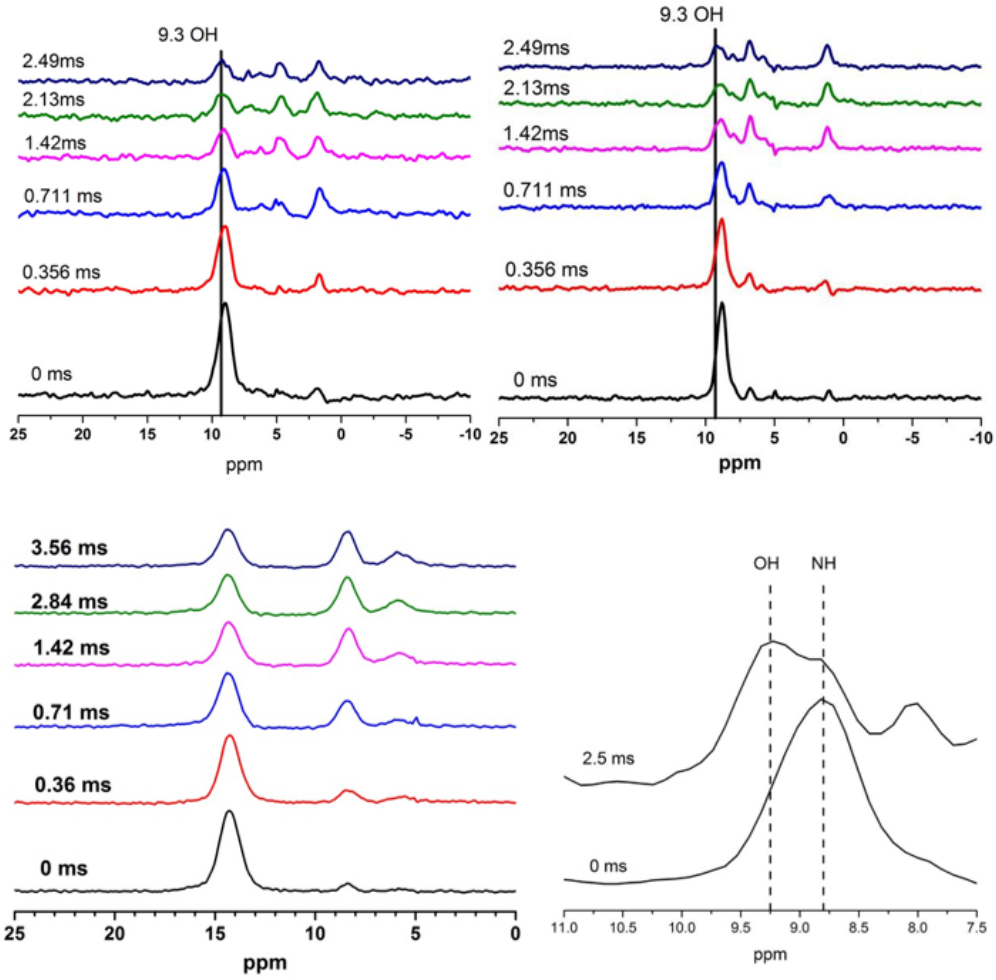

FIGURE 3.2: Spectra of HMQC filtered RFDR. The top two are the full spectra for the monoclinic (left) and orthorombic (right) polymorphs of acetaminophen and the bottom right is a magnification of the NH/OH region. All experiments were performed on a JEOL ECZ600R at 600 MHz ^1H Larmor frequency using a JEOL RESONANCE Inc. 0.75mm double-resonance MAS probe under 90kHz $\pm$ 20Hz MAS at room temperature (25 °C). $XY4_4^1$ phase cycling was used for RFDR with RFDR build up times = 16 tr * number RFDR building blocks ranging from 0 to 2.5ms.

Clearly, under fast MAS ^{1}H magnetization can be manipulated in a similar manner known in the literature and commonly used in solution or slow spinning MAS. It should be emphasized that the previous experiments, although subject to long relaxation times were collected with only 16 scans. This provides remarkably good signal to noise considering the presence of polarization transfer blocks, for which full magnetization transfer is never achieved. In the following section

we will turn our attention to measures that could not be made without fast MAS, namely the achieving ^{1}H isotropic/anistropic chemical shift correlation.

3.2 ^{1}H CSA under Fast MAS

Hydrogen atoms often mediate (de)stabilizing interactions which drive structure, function, and dynamics in numerous chemical systems. While X-ray diffraction is an excellent source of information for systems of periodic structure, it fails to accurately locate hydrogen atoms, leaving important structural determinants, such as the hydrogen bond, poorly defined. In solution, ^{1}H NMR spectroscopy is employed to elucidate the strength of hydrogen bonding interactions and is often used to determine secondary structure in biological macromolecules. Solid-state NMR spectroscopy is suitable for structural and dynamic insights in this regard; however, ^{1}H NMR spectra in the solid state have historically exhibited insufficient resolution due to severe spectral broadening caused by strong homogeneous ^{1}H–^{1}H dipolar interactions. Recent developments in magic angle spinning (MAS) technology have dramatically improved the situation, achieving spinning frequencies (>100 kHz) that can provide atomic resolution even for the most rigid systems [81]. Recent advances in methodology [81] and applications [2, 7, 30, 50, 72, 99] have demonstrated the power of proton-detected techniques. Of notable interest for structural studies are techniques used to measure the ^{1}H chemical shift anisotropy (CSA) tensor as a means to detect the magnetic tensorial contributions arising from the local electronic structure [46, 83, 115, 118]. These experiments quantify the CSA, $\zeta = |\delta_{zz} - \delta_{iso}|$, and the asymmetry parameter $\eta = (\delta_{xx} - \delta_{yy})/\zeta$; where δ_{iso} is the isotropic chemical shift and δ_{ii} are the principal components of the CSA tensor ranked according to $|\delta_{zz} - \delta_{iso}| \geq |\delta_{xx} - \delta_{iso}| \geq |\delta_{yy} - \delta_{iso}|$. The CSA is then the magnetic tensorial value which deviates most from the isotropically averaged frequency (δ_{iso}), and η gives a sense for the shape of the full CSA tensor based on the other components. The CSA is of general interest for structural elucidation as it provides an orientation-dependent metric connecting ^{1}H nuclei and their electronic landscape, which are typically detected independent of one another by neutron and X-ray diffraction. As such, the ^{1}H CSA has the potential to resolve ambiguities from X-ray crystallography– an approach that was successfully demonstrated for the structural refinement of hydrogen bonded atomic positions in L-ascorbic acid [72]. Due to the relative infancy of robust methods to detect the ^{1}H CSA, limited experimental data has been measured to establish trends regarding different structural constraints. The influence of strong hydrogen bonding was explored in earlier work through computation and limited experimental results [85, 90, 97, 102] which have been confirmed by recent measurements [73]. Nevertheless, many open questions remain unaddressed regarding its sensitivity to weak hydrogen bonds, e.g. CH$\cdots$O bonding, and other electrostatic forces such as $\pi - \pi$ interactions, which also participate in structure formation. To explore such questions, determining the ^{1}H CSAs for structurally distinct arrangements of the

same molecule (i.e., polymorphic crystals or hydrates) could establish trends without confounding influences from differences in covalent bonding. This approach is adopted here by employing 2D CSA/CS correlation experiments under 90 kHz MAS to probe structural differences for two polymorphic forms of the drug acetaminophen as well as exploring water in different hydrate forms of pharmaceuticals.

3.2.1 ^{1}H CSA Pulse Sequence Description

The pulse sequence [82, 84] used for CSA/CS correlation depicted in Figure 3.3 is a gamma-encoded symmetry based pulse sequence for selective recoupling of the ^{1}H CSA anisotropy. The notation $R18_8^7(270°90°)$ comes from the symmetry principles for pulse sequence design introduced by Levitt and co-workers [64]. The general notation RN_n^ν refers to N, the number of phase-alternated composite pulses, n the number of rotor periods, and ν determines the phase of the pulses by $\pi\nu/N$. In this case, (270°90°) is a composite 180° pulses whose phase alternates between (70°, 250°) and (-70°, -250°). The proper choice of N, n and ν determine which interactions are retained according to the symmetry of the first-order Hamiltonian.

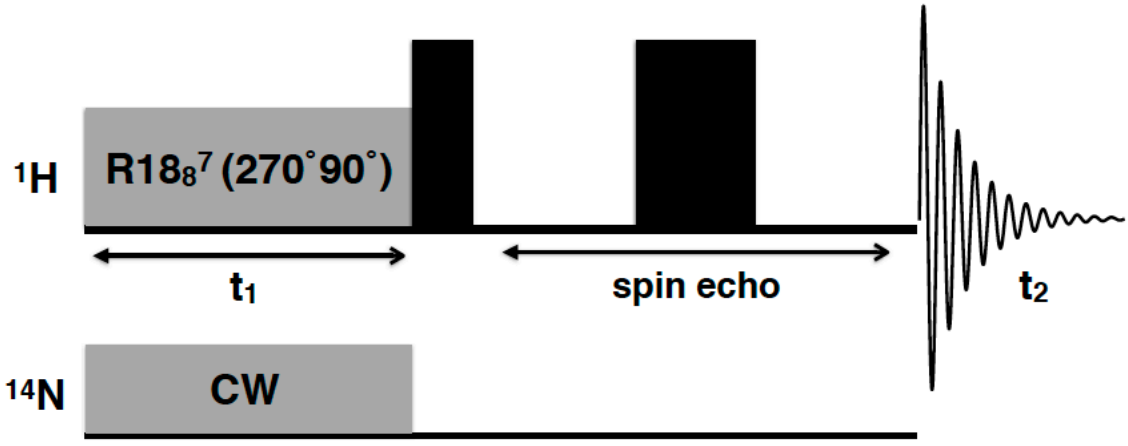

FIGURE 3.3: Schematic of the radio-frequency pulse sequence used for all CS/CSA correlations experiments. The solid black rectangles in the ^{1}H RF channel are 90° and 180° pulses.

In this case, the symmetry of the sequence encodes the CSA and heteronuclear dipolar couplings. It is in general difficult to separately recouple heteronculear dipolar couplings or the CSA. To limit the evolution in t_1 strictly to CSA evolution, heteronuclear decoupling is applied on the ^{14}N channel. It is important to note that this is necessary for any abundant hetero-nuclei, such as ^{14}N. Given the low natural-abundance of ^{13}C and ^{15}N, it is not necessary to apply decoupling on

these RF channels, as only very small fractions of ^{1}H spins are affected. The proton magnetization is then refocused by a spin-echo to suppress background signals and then detected in the t_2 period where the isotropic chemical shift is encoded in the magnetization. The experimentally measured spectrum gives a bimodal line-shape in the t_1 dimension whose splitting is roughly proportional to the magnitude of the CSA, while the shape of the line is related to the asymmetry parameter, or shape of the CSA tensor. The experimentally measured line-shapes are numerically simulated using SIMPSON software to extract the CSA and asymmetry parameters.

3.3 Role of Anomalous Water Constraints in the Efficacy of Pharmaceuticals Probed by ^{1}H Solid-State NMR

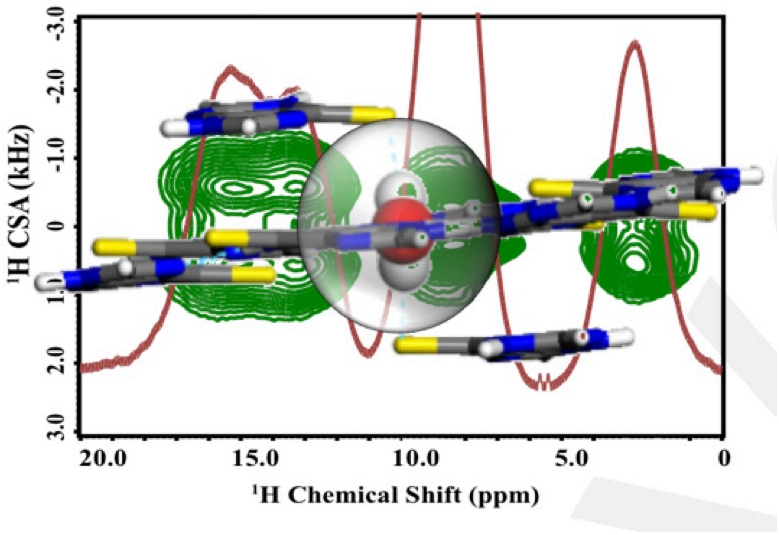

Hydrates are crystalline materials where water molecules occupy a regular space within the crystal structure, whether at an isolated site or within a defined channel [55]. For cases where the crystal structure is lost during application, such as with the dissolution of pharmaceutical hydrates, it might be expected that the presence of water in the solid would have little influence on properties. To the contrary, approximately 20% of the 100 top selling drugs are hydrated forms and their physicochemical properties often differ dramatically from their anhydrous counterparts [55, 106]. Inclusion of water into the crystalline lattice typically decreases the water solubility of that form due to the partial solvation of molecules in the solid state [55]. Reduced solubility of hydrate forms is also regularly accompanied by increased resistance to solid form changes occurring during production and storage [55]. Consequently, the choice of a hydrate form for development

often involves a tradeoff between solubility and stability [35] which can reduce the efficacy of BCS class II and IV drugs where bioavailability can be solubility limited [5]. The increased stability seen in these hydrate forms largely arises from hydrogen bonding throughout the crystal structure between the pharmaceutical and water molecules [77]. Determining the propensity for hydrate formation based on the available number of hydrogen bond donors and acceptors in a molecule [32, 48], as well as predicting the stability of a structure based on the hydrogen bonding motif surrounding the water molecules [34, 77] have been pursued in the literature. Nevertheless, hydrogen bonding is only one of the aspects related to hydrate stability; the participation of other electrostatic interactions and assembly modes merit consideration. The ^{1}H CSA should serve as a direct measure of water binding interactions in hydrate structures to augment the X-ray data. This potentiality is realized here in the context of pharmaceutical hydrates.

One dramatic example of the role of water in pharmaceuticals is the recently discovered hemihydrate form of the anti-leukemia drug, mercaptopurine [54]. This form shows a three fold increase in the bioavailability of the drug over the currently prescribed monohydrate form, a feature that results from a combination of several physical properties. Of the three forms of mercaptopurine, the anhydrate form is the most soluble, as is common with hydrated materials. However, the anhydrate form suffers from conversion to the least soluble (monohydrate) form in aqueous solution within hours, whereas the hemihydrate form is more stable and does not completely convert for several days [54]. The monohydrate has a dehydration temperature of 150 °C, whereas the hemihydrate form shows an exceptionally high dehydration temperature of 240 °C. This value is the highest observed for any non-salt hydrate in the literature [15, 51, 67, 79, 109], and a staggering 90°C higher than the monohydrate form. Consequentially, an ideal balance of stability and solubility is found in the hemihydrate form that is responsible for its increased efficacy. Given the extreme thermal stability, which is generally indicative of high thermodynamic stability, the favorable dissolution and increased bioavailability of the hemihydrate is an exception to typical hydrate behavior. The structural basis for this kinetic behavior is elucidated here and aspects of the thermodynamics leading to the observed physical properties of each form are computed. To probe the factors that contribute to the structural variation of water and its environment, we chose to investigate the local environment of water in the two hydrates of mercaptopurine due to the significant differences in stability and efficacy known for the mono and hemihydrate forms. The combined use of the ^{1}H CSA measured from MAS experiments, IR experiments, and quantum calculations as presented below enabled us to develop a mechanism for the dehydration behavior and functional difference between these two forms of mercaptopurine hydrates. Structural depictions based on the reported crystal structures [54] emphasizing the incorporation of water in the two hydrate forms of mercaptopurine are shown in Figure 3.4. In the monohydrate, water molecules participate in an extended hydrogen bond network with each water bridging three mercaptopurine molecules. The hydrogen bond distances, based on crystal structures with protons normalized to

average neutron scattering positions, for O-H$\cdots$N, O-H$\cdots$S and N-H$\cdots$O are 1.82 Å 2.40 Å and 1.75 Å respectively. In the hemihydrate structure, six mercaptopurine molecules are hydrogen bound through N-H$\cdots$N bonds between the imidazole and pyrimidine moieties forming ring-like structures. The water molecules sit inside the ring with its oxygen weakly interacting with the aromatic ring via C-H$\cdots$O interactions (at H$\cdots$O distances of 2.28 Å and 2.42 Å), while the hydrogens participate in O-H$\cdots$S hydrogen bonds with sulfur atoms in adjacent rings above and below at distances of 2.37 and 2.45 Å (Figure 3.4b). The preference for hydrogen bonding positions are reflected by the electrostatic potential map of mercaptopurine show in Figure 3.4a, where the tautomerization redistributes the charge density across the molecule. X-ray analysis allows one to infer chemical information such as hydrogen bonding based on atomic positions, however, it does not always reflect the exact type or magnitude of the interactions occurring. On the other hand, ^{1}H SSNMR is sensitive to the electrostatic environment of each atom and can provide additional information regarding the type and magnitude of the interactions involved.

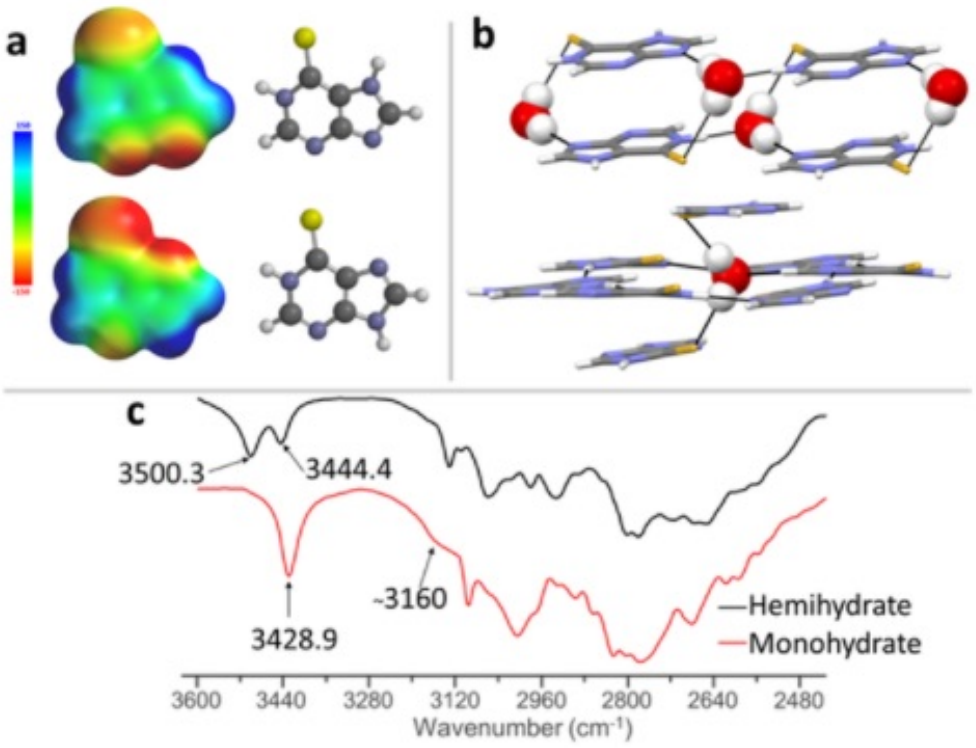

FIGURE 3.4: Effect of tautomerization and hydration on mercaptopurine structure. (a) Electrostatic potential maps of the mercaptopurine tautomers seen in the monohydrate (top) and hemihydrate (bottom) forms. (b) Depictions of the hydrogen bonding motifs within the monohydrate (top) and hemihydrate (bottom) structures. (c) IR spectrum showing the OH stretching frequencies of the two forms of mercaptopurine.

The 2D CS/CSA ^{1}H MAS spectra of both mercaptopurine hydrates, obtained using the pulse sequence given in Figure 3.3 of the introduction, are shown in Figure 3.8 and the corresponding NMR parameters are summarized in Table 3.1. For the hemihydrate, the NH proton signals are resolved at 13.0 and 15.0 ppm, the unresolved aromatic resonances appear at 8.34 ppm, and the water signal is at 2.75 ppm. Discussion of the NMR assignments is given in Appendix A.

In addition, CSA experiments were run without ^{14}N decoupling, allowing the through space ^{14}N–^{1}H heteronuclear dipolar interaction to also contribute the line-shape as well as the CSA. A comparison of the line-splitting with and without decoupling allows for easy identification of the NH resonances. The top half of Figure 3.5 demonstrates this effect where the most downfield resonances in both cases are severely broadened by the lack of decoupling, confirming the NH resonance assignments. The NH resonances are so distorted their lines could not be fit.

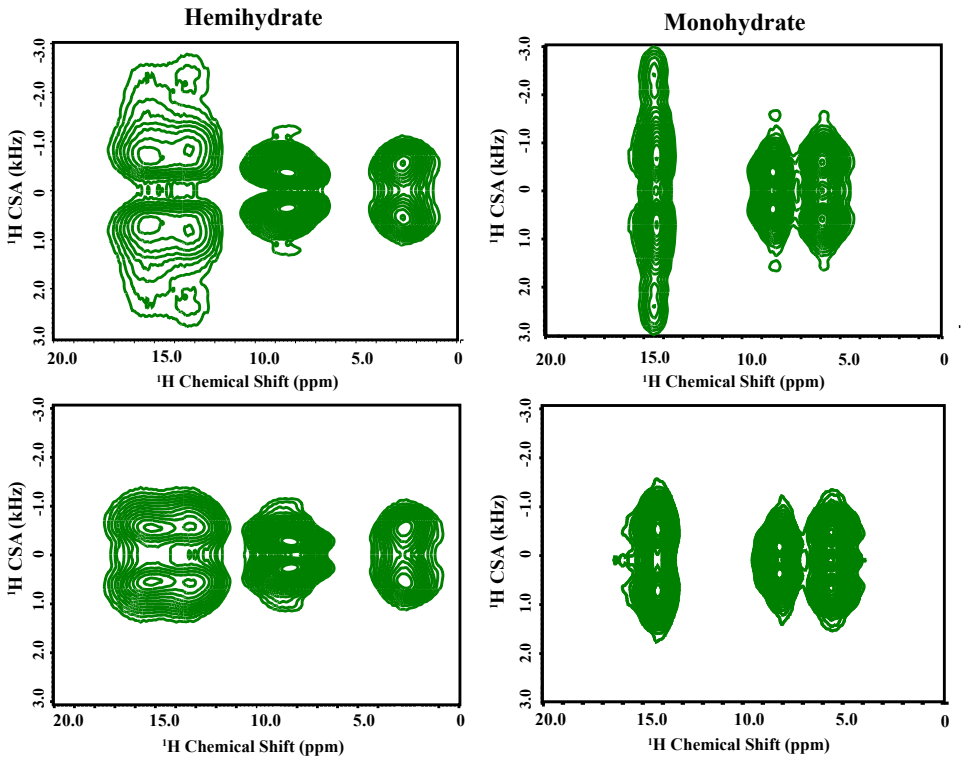

FIGURE 3.5: ^{1}H CS/CSA correlation recorded with (bottom) and without (top) ^{14}N decoupling. The downfield resonances are clearly most influenced by the presence of ^{14}N heteronuclear dipolar interaction identifying those as directly bonded.

For the monohydrate, the water peak appears at 5.9 ppm, the overlapping NH peaks appear at 14.4 ppm, and the aromatic protons at 8.45 ppm. It is typical in a hydrogen bond for the nucleus to be pulled from the center of mass of the electrons of the atom [100], which results in a deshielded nucleus, larger isotropic CS values and an increase in the CSA [85, 90, 97, 102]. Proximate electron rich groups can also cause dramatic CS changes, depending on the atomic species, orientation, etc [93]. Consistent with the X-ray data, stronger hydrogen bonding for the monohydrate water is evidenced by the 0.6 ppm larger CSA and 3 ppm further downfield isotropic CS. The 3 ppm difference in the isotropic CS of the water resonance between the two forms indicates dramatically different local environments for the water. For reference, the CS of pure water at ambient conditions is 4.72 ppm, which is downfield shifted due to transient hydrogen bonding from dilute or "monomeric" values typically around 1 ppm [9, 68, 86]. The rigid hydrogen bonding in the monohydrate results

in even further deshielding by slightly over 1 ppm. On the other hand, a large up-field shift is observed for the hemihydrate, supportive of weaker hydrogen bonding and/or a combination of intermolecular electronic shielding from the immediate solid environment. The hemihydrate water is surrounded by a dense electronic environment of 4 sulfur atoms and neighboring aromatic rings. These sulfur atoms and the neighboring aromatic moieties form a tight "cage" around the water molecules, providing the electronic shielding.

TABLE 3.1: Isotropic and anisotropic chemical shift parameters for protons in hemihydrate and monohydrate forms of mercaptopurine measured from fast magic angle spinning solid-state NMR experiments with and without (denoted as *) ^{14}N decoupling.

Hemihydrate	**NH**	**NH**	**Ar**	**H_2O**
$\delta_{iso}(ppm)$	15.2	13.23	8.3	2.8
$\mid\zeta\mid$(ppm)	10.2	11.6	5.2	9.6
η	0.8	0.8	0.9	0.6
$\mid\zeta\mid$*(ppm)	–	–	6.7	9.9
η*	–	–	0.7	0.7
Monohydrate	**NH**	**Ar**	**H_2O**	
$\delta_{iso}(ppm)$		14.4	8.5	5.9
$\mid\zeta\mid$(ppm)		11.3	5.5	10.2
η	0.7		0.9	0.8
$\mid\zeta\mid$*(ppm)		–	7.1	10.6
$\eta*$	–		0.7	0.8

The differing water environments between the two forms are also implicated by IR spectroscopy. Two OH stretches are observed for the hemihydrate at 3500.3 and 3444.4 cm^{-1} (See Figure 3.6) while only one OH stretch for the monohydrate (3428.9 cm^{-1}) is observed in the 3300-3600 cm^{-1} region (Figure 3.8).

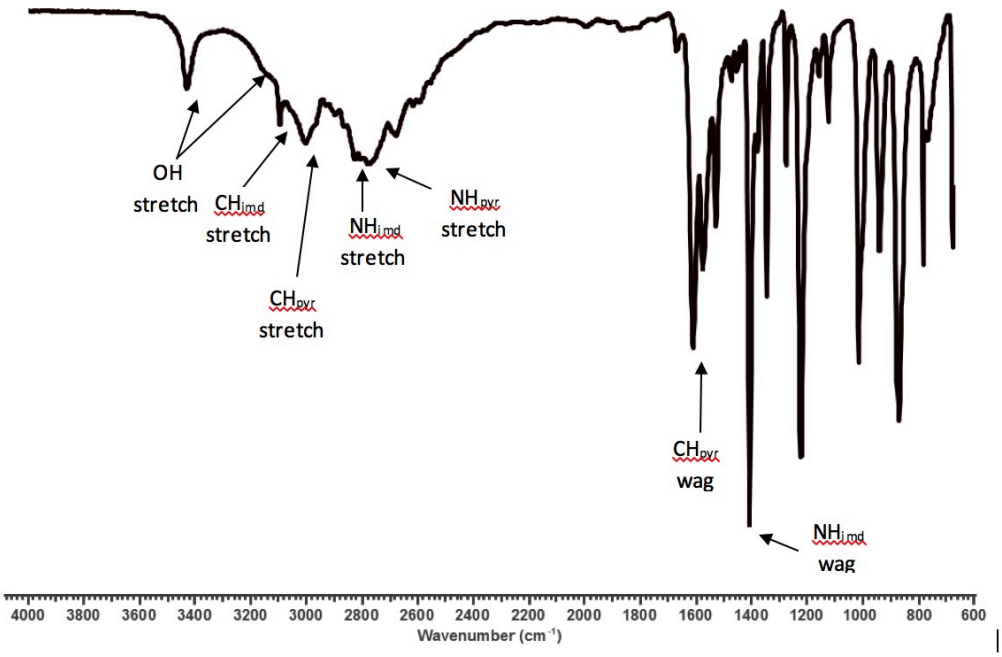

FIGURE 3.6: Experimental IR spectrum of the monohydrate form of mercaptopurine with labels based on computational predictions. [Note: imd=imidazole ring, pyr=pyrimidine ring]

The monohydrate stretch appears at a lower energy which is consistent with the structure having stronger hydrogen bonding [66, 77]. Computational predictions (see appendix A) of the stretching frequencies are in accord with these experimental observations but also detect an additional OH stretch at an even lower energy of 3160 cm^{-1} belonging to the hydrogen bound with the nitrogen. No corresponding stretches are seen in the hemihydrate form. The IR data supports the assertion that the two forms display distinctive hydrogen bonding that is stronger in the monohydrate form.

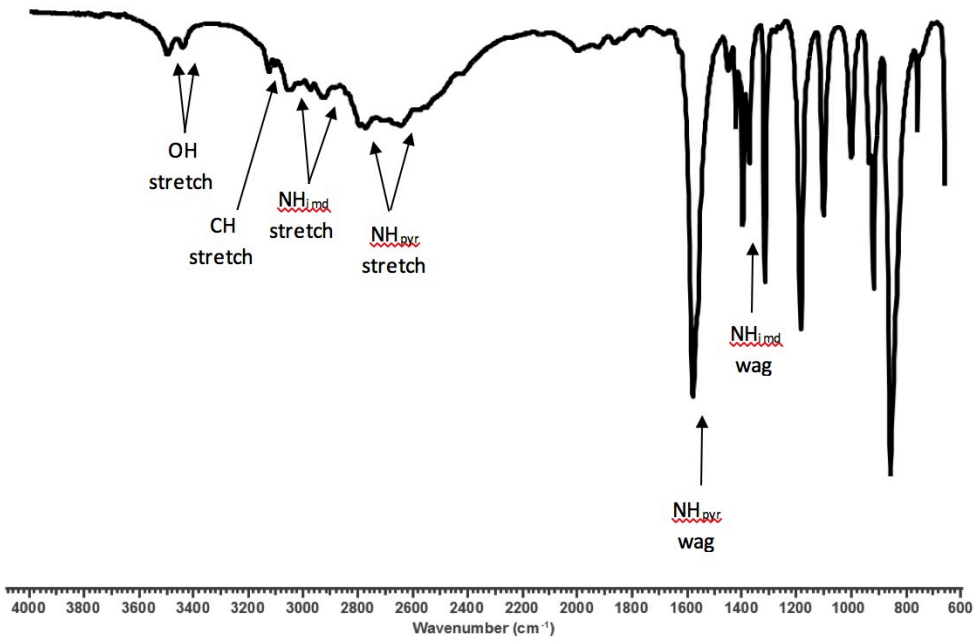

FIGURE 3.7: Experimental IR spectrum of the hemihydrate form of mercaptopurine with labels based on computational predictions. [Note: imd=imidazole ring, pyr=pyrimidine ring]

No clear explanation for the difference in dehydration temperatures, which is much higher for the hemihydrate, can be identified from data above. Consequently, we performed molecular mechanics and DFT calculations taking each of the structures with and without the water molecules present to compute the theoretical desolvation energy for each hydrate form (See appendix A for details). Consistent with the experimental data, the energy of removal per water molecule is higher for the monohydrate (on the order of 10 kcal/mol/water molecule), suggesting that the hydrogen bonding in the monohydrate is the dominant enthalpic factor between the two (see table A.1 in appendix A). Again, neither experimental nor computational data evidence any specific binding interaction accounting for the dramatic stability of the hemihydrate over the monohydrate form. The interpretation we adopt from these results is that the high thermal stability in the hemihydrate water is due to the constrained environment imposed by the electronically dense neighbors mimicking a cage and entrapping the water. Such a cage could explain the upfield 2.75 ppm isotropic chemical shift value. This large upfield shift strongly corroborates a tight electrosteric environment due to magnetic shielding of the cage, despite the presence of hydrogen bonding between the water and the hemihydrate structure.

The above information suggests the following hypothesis for the dehydration mechanism in

each form. Upon heating and water loss, the monohydrate becomes amorphous due to the collapse of the extensive network around the water molecules in the structure [54]. The molecules then undergo tautomerization followed by recrystallization into the anhydrate form. The hemihydrate however, converts immediately to the structurally similar anhydrate upon water loss shortly before decomposition, with no intermediate amorphous phase [54]. This occurs through a thermal loosening of the "cage", which is dependent on the hydrogen bonding between the mercaptopurine molecules themselves and not from a specific interaction of the water molecules within the crystal. Functionally, the electro-steric cage containing weakly interacting water provides only a minor decrease to the solubility of the form compared to the anhydrate, but has a great impact on the stability of the form overall, leading to the hemihydrate being the most efficacious solid form of mercaptopurine.

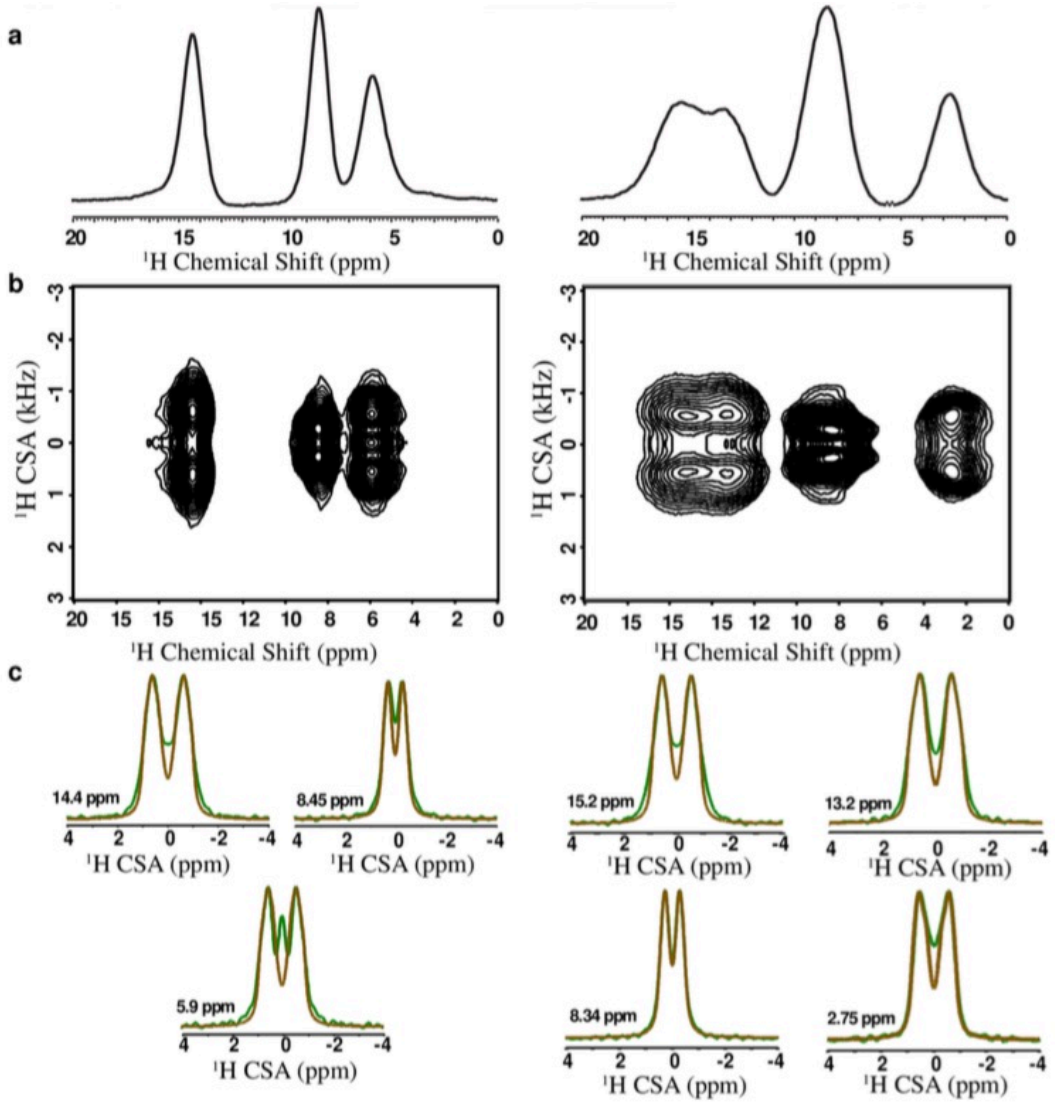

FIGURE 3.8: ^{1}H CSA spectra of monohydrate (left) and hemihydrate (right) of mercaptopurine. (a) 1D isotropic ^{1}H spectra. (b) 2D ^{1}H CS/CSA correlation spectra. (c) ^{1}H CSA lineshapes, extracted from 2D spectra (green), associated with the indicated isotropic chemical shift values, and their simulated best fits obtained using SIMPSON (brown).

3.3.1 Materials and Methods

Further details on NMR experiments, sample preparation and characterization, Infrared Spectroscopy, computational details and further supporting information can be found in appendix A

3.4 Electrostatic Constraints Assessed by ^{1}H MAS NMR Illuminate Differences in Crystalline Polymorphs

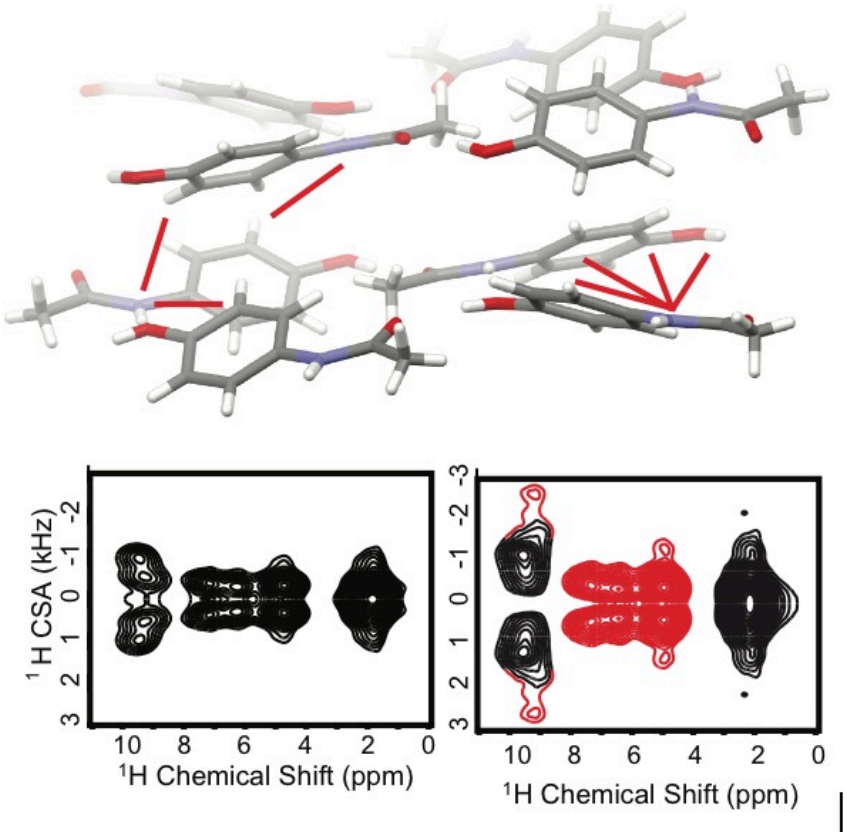

Acetaminophen forms three known polymorphs two of which, the orthorhombic and monoclinic forms, are stable under ambient conditions. The structural differences (see Figure 3.9) between the two polymorphs make acetaminophen a good model to study polymorphism. Acetaminophen contains chemically diverse functional groups, including a hydroxyl, amine, aromatic, and methyl group that exert varying intermolecular effects. Thermodynamically, the two polymorphs have an enantiotropic predicted transition point at -165 °C by DSC, above which the monoclinic form is favored due to a larger entropic contribution [91]. While the thermodynamically stable monoclinic is easily isolated through evaporation of many solvents, pure crystallization of the metastable orthorhombic polymorph is more difficult. Many researchers have focused on finding ways to increase the scale of this polymorphic form through the use of different cooling strategies and by introducing functionalized surfaces or additives to the system [3, 4, 19, 53, 74]. In the course of this study, we discovered a novel technique for consistently producing pure orthorhombic ACM

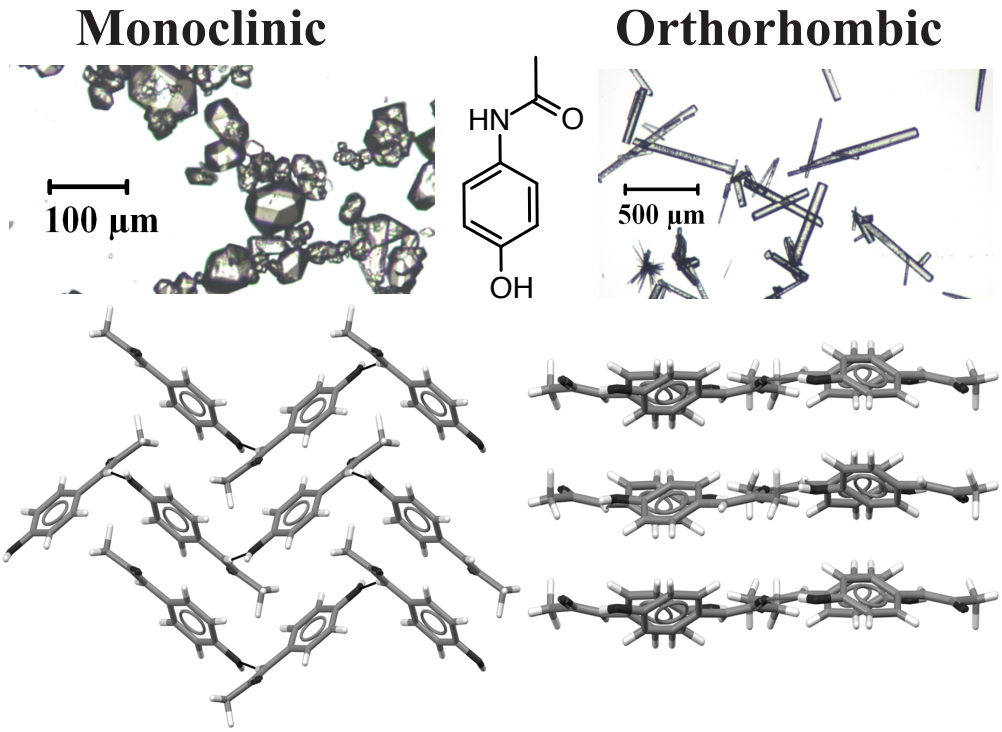

FIGURE 3.9: Crystal structures illustrating packing of monoclinic (left) and orthorhombic (right) polymorphs of acetaminophen. The lines display the intermolecular hydrogen bonding network which is pleated with respect to the molecule for the monoclinic while flat for the orthorhombic in layered planes. FTIR and Raman spectra for both crystalline forms are given in Appendix B

from water at 0 °C, alluding to an Ostwald's rule of stages scenario (see appendix B for details of crystal growth). The primary structural constraint in both forms is the hydrogen bond network composed of the hydroxyl group which serves simultaneously as a donor and acceptor forming OH$\cdots$O=C and NH$\cdots$OH hydrogen bonds. For the orthorhombic form, this network lies in plane with the aromatic groups, forming stacked sheets, whereas in the monoclinic structure, it forms a two-dimensional ribbon causing buckled planes between the aromatic groups. Despite the different geometries, both IR and Raman spectroscopy, common techniques for bonding assessment, resulted in nearly identical spectra (see Appendix B Figures B.2 and B.1). The ^{1}H solid-state NMR spectra (Figures 3.10 and 3.11), on the other hand, are remarkably sensitive to the polymorphic changes. Given that the bond lengths, bond angles, and torsion angles are approximately the same for an individual molecule in each polymorph, we attribute the bulk of the chemical shift differences to intermolecular effects, the interpretation of which is discussed below.

A critical feature of the 2D radiofrequency pulse sequence employed is that it simultaneously

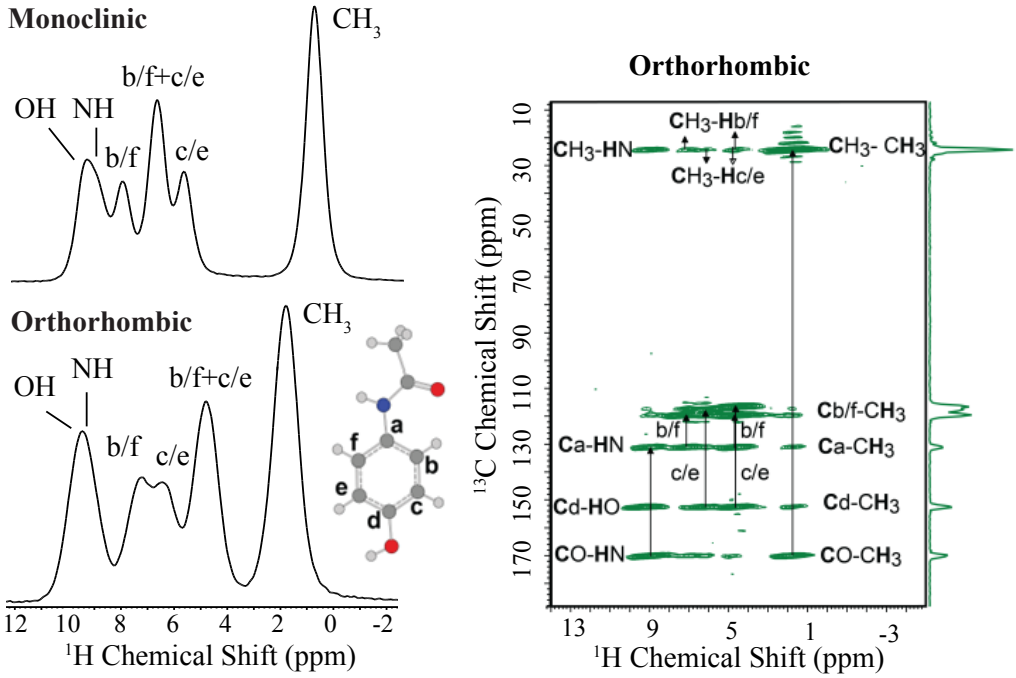

FIGURE 3.10: Left: ^{1}H spin-echo NMR spectra collected under 90 kHz MAS of the two acetaminophen polymorphs with resonance assignments. Significant differences observed in the shape and frequency of spectral lines clearly demonstrate the sensitivity of ^{1}H chemical shift to structural differences between the two crystalline forms. Right: two-dimensional ^{13}C-1H HETCOR spectrum obtained under 70 kHz MAS confirming the resonance assignment of orthorhombic polymorph.

TABLE 3.2: Isotropic and anisotropic chemical shift parameters for protons in the monoclinic and orthorhombic polymorphs of acetaminophen measured from 90 kHz MAS NMR using a 2D CSA/CS pulse sequence with and without (denoted as *) ^{14}N decoupling; the pulse sequence is given in Figure 3.3. CSA values obtained from DFT calculations are denoted by "Calc."

Orthorhombic	**OH**	**b**	**f+c**	**e**	**CH_3**
$\delta_{iso}(ppm)$	9.4	7.1	4.7	6.3	1.8
$\mid\zeta\mid$(ppm)	15.3	6.7	6.3	5.8	3.0
η	0.3	0.6	0.7	0.75	1.0
$\mid\zeta\mid$*(ppm)	16	7.2	6.7	6.1	3.7
η*	0.3	0.65	0.8	0.75	1
Calc. $\delta_{iso}(ppm)$	9.0	8.2	5.6,5.4	7.3	2.4
Calc. $\mid\zeta\mid$(ppm)	-16.1	6.6	4.2,2.9	-4.0	-3.7
Calc. $\mid\zeta\mid$*(ppm)	0.6	0.9	1.0,0.7	0.3	0.8
Monoclinic	**OH**	**b**	**f+c**	**e**	**CH_3**
$\delta_{iso}(ppm)$	9.4	8.0	6.8	5.8	1.1
$\mid\zeta\mid$(ppm)	16.4	7.4	5.6	4.8	5.0
η	0.4	0.6	0.7	1.0	1.0
$\mid\zeta\mid$*(ppm) w/o dec.	16.0	7.2	5.6	4.8	5.0
$\eta*$	0.5	0.6	0.7	1.0	1.0
Calc. $\delta_{iso}(ppm)$	9.0	8.3	7.4,7.6	6.4	1.8
Calc. $\mid\zeta\mid$(ppm)	-14.1	-6.9	4.8,-4.6	-3.9	-5.7
Calc. $\mid\zeta\mid$*(ppm)	0.4	0.6	1.0,0.9	0.6	0.6

recouples the CSA and the through-space heteronuclear dipolar couplings, encoding in the indirect dimension a line shape that contains both contributions. To achieve CSA-only line shapes, heteronuclear decoupling must be applied to all other abundant nuclei in the sample, which is required for ^{14}N nuclei in ACM. Due to the very large magnitude of the ^{14}N quadrupolar interaction, ^{14}N decoupling can be difficult to accomplish experimentally. However, it was recently shown that under conditions of fast spinning and moderately high RF field strengths, the ^{14}N decoupling becomes quite efficient [82]. A comparison of the 2D spectra acquired with (Figure 3.11a) and without (Figure 3.11b) ^{14}N decoupling, however, can be utilized for spectral assignment and qualitative structural assessment. For the second-most downfield peak in both forms, the indirect dimension clearly marks the NH resonance with the appearance of satellite peaks in the undecoupled spectrum. In addition, the CSA values for all other protons in the orthorhombic form are perturbed under heteronuclear dipolar evolution, while the values in the monoclinic, except the NH and OH peaks, are virtually unaffected (see Table 3.2). The apparent stronger ^{14}N–^{1}H dipolar couplings in the orthorhombic form, particularly in the aromatic region, are direct evidence of its denser and/or more rigid structure. Indeed, simulations including the heteronuclear ^{14}N–^{1}H dipolar couplings based on static distances in the crystal structures for the nearest ^{14}N neighbor of each proton demonstrate that the line-shapes should be similarly influenced for both polymorphs in the aromatic region (see Appendix B Figures B.4 and B.5). The implication is that the monoclinic undergoes increased molecular/librational motion on the NMR timescale to reduce the ^{14}N–^{1}H dipolar couplings. Thus, a measure of the CSA with and without ^{14}N decoupling provides a qualitative indication of the dynamic features (or structural disorder) between the two forms, showing that the monoclinic undergoes increased dynamics. While molecular motion also averages the CSA, thereby narrowing the line shape in the observed CSA spectra, without precise, a priori knowledge of the geometry of the electrostatic field defining the CSA, comparing the extent of motional averaging between the two polymorphs is difficult from the CSA alone.

The ^{1}H CSA is known to be quite sensitive to hydrogen bonding as the nuclear and electronic coordinates become distorted in hydrogen bond formation [100], resulting in a less shielded nucleus, larger isotropic CS values, and an increase in the magnitude of the CSA [85, 90, 97, 102, 107]. Typically the CSA in strong hydrogen bonds is negative by the convention reported here [57, 108, 116]. Unfortunately, due to the γ-encoded symmetry based recoupling scheme used, only the magnitude, not the sign, of the CSA can be measured. As such, we performed DFT calculations to support the experimental results (see Appendix B). Between the two forms, the hydrogen bond donor/acceptor distances in the primary hydrogen bond network are only slightly shorter for the monoclinic. For $NH\cdots O_{hydroxyl}$ the heavy atom distances are 2.97 Å and 2.93 Å for the orthorhombic and monoclinic, respectively, while the $OH\cdots O$ donor/acceptor distances are 2.73 Å (ortho) and 2.66 Å (mono). The hydroxyl protons have very similar isotropic CS values, which is consistent with the IR data, despite the 0.13 Å closer donor-acceptor distance. The CSA, however,

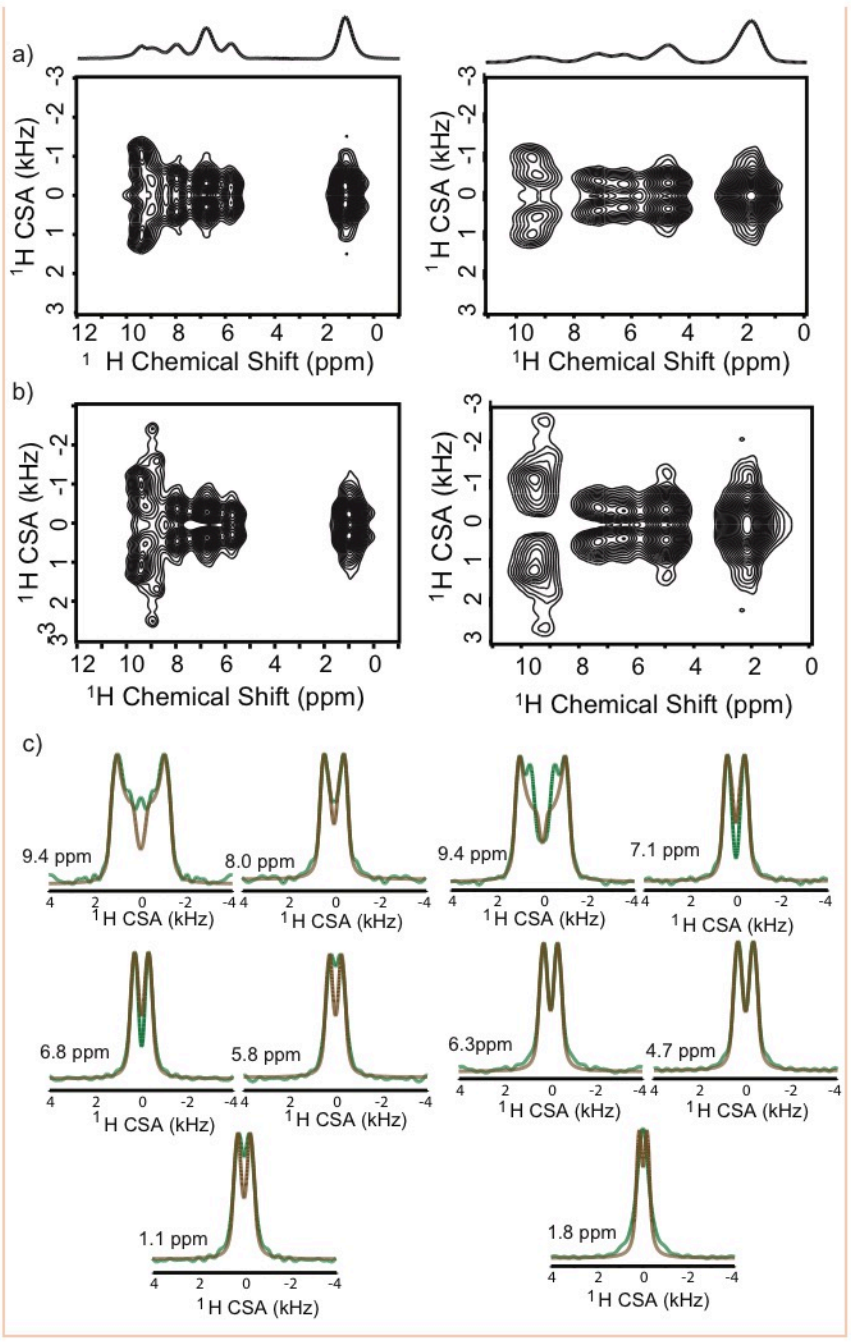

FIGURE 3.11: 2D ^{1}H/^{1}H CSA/CS correlation under 90 kHz MAS with (a) and without (b) ^{14}N decoupling for the orthorhombic (right) and monoclinic (left) polymorphs of acetaminophen. The influence of ^{14}N-^{1}H dipolar couplings are marked by the broadening and appearance of satellite peaks in panel (b). Slices from CSA (or ω_1) dimension and numerically simulated fits using SIMPSON [8] are given in panel (c).

is 0.9 ppm larger for the monoclinic OH suggesting a slightly stronger bond strength. The DFT calculations confirm that the CSA for the two positions is due to hydrogen bonding as they are both negative (see Table 3.2). The result demonstrates that the ^{1}H CSA is capable of measuring minute hydrogen bonding differences.

More substantial differences in hydrogen bonding are found for the aromatic hydrogen atoms. The aromatic protons are well-resolved between the two forms with the largest CSA and most deshielded isotropic chemical shift corresponding to position *b* in both polymorphs. This is closest to the intramolecular carbonyl ($C_{aro} \cdots O_{c=o}$ distances of 2.28 Å in ortho and 2.31 Å for mono) and well within the limits for CH$\cdots$O hydrogen bonding [110]. Monoclinic ACM has an additional intermolecular contact (2.89 Å) to a carbonyl oxygen which could explain its 0.8 ppm downfield CS and 0.7 ppm larger CSA. In addition, the sign of the computed CSA is negative for the monoclinic and positive for the orthorhombic (Table 3.2) supporting a stronger hydrogen bond argument in the monoclinic. A similar effect is found for position *e* where both forms have $C_{aro} \cdots O_{c=o}$ distances at 2.85 Å (ortho) and 2.92 Å (mono), but in the orthorhombic a nitrogen is also nearby at 2.86 Å likely contributing to its downfield shift (both resonances have negative computed CSA values). For both the *b* and *e* aromatic positions, the CS and CSA indicate that a proton in one form but not the other is involved in a ternary bond complex which causes the differences in the NMR parameters.

The aromatic protons are also influenced by ring current effects, which exert a strong influence on nuclear shielding. The interactions of neighboring ring currents are the source for the substantial CS differences at the overlapping *f* and *c* positions between the two polymorphs. The influence of aromatic rings on the CSA tensor depends on the orientation of the ring with respect to the proton: the shielding field is perpendicular while the deshielding is parallel to the plane of the ring. The atypical, upfield 4.7 ppm isotropic value of the *f* and *c* protons in the orthorhombic form suggests that the protons point towards the face of other rings in the shielded orientation. This is exactly what is found in the orthorhombic, with *f* and *c* positioned at distances of 2.70 Å and 2.81 Å to the centroid of neighboring rings. This effect leads to the largest CS difference in the system where the same positions in the monoclinic are 2 ppm downfield and have no close contacts but also have a 0.7 ppm smaller CSA. A similar effect is found for the methyl group where, despite CH_3 rotations, finite CSA contributions can be measured and the isotropic values between the two forms also differ by 0.7 ppm. For the monoclinic, the CH_3 group faces a neighboring aromatic group with the methyl carbon being 3.8 Å from the aromatic centroid. In the orthorhombic, the methyl group is relatively isolated from any neighboring groups.

The NMR results show that the ^{1}H CSA is quite sensitive to differences in the electrostatic fields imposed by different polymorphic arrangements, which help to illuminate the static picture provided by X-ray crystallography. The CSA response to hydrogen bonding, both weak and strong, differentiates the two polymorphs; IR spectroscopy was much less sensitive in this regard.

In addition, the rather strong influence of ring current effects on the CSA provides an excellent metric for $\pi - \pi$ interactions. In full consideration of the data, a justification for the previously reported free energy differences can be proposed. First, the NH$\cdots$OH$\cdots$O hydrogen bonding network is similar in strength, slightly favoring the monoclinic as evidenced by the CSA. In addition, $CH_{aro} \cdots O/N$ bonding was found in both forms, with varying strengths, the strongest of which, based on deshielding and CSA magnitude, involved an intra/intermolecular ternary complex for the CH_b resonance in monoclinic ACM. Despite the comparatively weak nature of CH$\cdots$O hydrogen bonds, it has been shown that they are of structural significance in many crystal structures [104] and are stronger when the acceptor oxygen is also involved in a stronger hydrogen bond [23, 24], as is the case here. The CSA parameters then suggest that the overall hydrogen bond formation in the monoclinic is potentially a bit stronger than orthorhombic ACM. Additional contributions from the aromatic groups were also identified. In the orthorhombic form, the rings within a layer are sandwiched by two other rings on opposite ends, which is reflected in the substantial difference between the CSA parameters for CH_f and CH_c positions. This could account for the stronger contribution of the ^{14}N–^{1}H dipolar couplings in the undecoupled spectra, caused by a more rigid structure. The lack of such a constraint in the monoclinic ACM provides it with more degrees of freedom, consistent with previous findings [91].

3.4.1 Materials and Methods

Full description of the experimental details including NMR experiments and simulations, sample preparation and characterization, Infrared Spectroscopy, computational details and further supporting information can be found in appendix B

3.5 Chapter Summary

The ability to suppress homonuclear dipole/dipole interactions and resolve chemically distinct protons under fast MAS enables one to significantly augment the crystal structures obtained by diffraction techniques. The results of this chapter show that ^{1}H CSA can be effectively measured under fast MAS and is a useful tool to characterize the local environment of small molecules in crystalline systems. Specifically, the ^{1}H CSA was shown to be sensitive to changes in hydrogen bond structures, aromatic electrons constraints, influence of large heteroatoms, and methyl group interactions.

The advantage of directly probing water allowed us test differences in its inclusion in the hydrate forms of mercaptopurine. Large differences in the CSA tensor were detected between the hemihydrate and monohydrate forms, which provided unique information about the role of intermolecular interactions. This led to the surprising conclusion that the outstanding stability of the hemihydrate form of mercaptopurine arises from to a structural cage largely composed of

Sulfur atoms imposed on the contained water molecules rather than any specifically favorable interactions such as hydrogen bonding. A molecular rationale could be proposed for the favorable balance of stability and solubility of the hemihydrate form of mercaptopurine leading to its favorable pharmaceutical properties. In the two polymorphs of acetaminophen the ^{1}H CSA was also quite sensitive to changes in the electrostatic landscape imposed by differences in crystal packing. The results demonstrate the remarkable potential of ^{1}H ultrafast MAS NMR to significantly augment crystal structures obtained by diffraction techniques through the direct measures of hydrogen atoms across a range of chemically distinct groups. In addition, this study has enabled a rationale for the stabilization of the monoclinic structure and the basis for the formation of the metastable orthorhombic forms of ACM.

Chapter 4

Dynamics in Metal Organic Frameworks

Portions of this chapter were adapted from the following work:[1]
Damron, J.T. Ma, J., Kurz, R. Saalwächter, K. Matzger, A.J., Ramamoorthy, R. The Influence of Chemical Modification on Linker Rotational Dynamics in Metal Organic Frameworks. *Angewandte Chemie Int. Ed.* (Submitted).

4.1 Introduction

Metal-organic frameworks (MOFs) are constructed from inorganic clusters bridged by organic linkers and possess ideal architectures for gas storage and mixture separation as well as generating recent interest as nano-devices and molecular machines (see Figure 4.1) [14]. In comparison to traditional inorganic porous materials, MOFs are far more dynamic/flexible due to the incorporation of organic ligands [44, 45, 49]. A key advantage of MOFs is the synthetic ease of chemical modification to the organic moieties without change of framework structure, known as isoreticular synthesis. This allows for many avenues of functional modification including adsorptive selectivity based on favorable ligand-guest interactions [47], changes in pore aperture for separations [43, 95], and shifts in optical behavior [38]. An additional feature of MOFs, which has captured much attention, is the prevalence of framework dynamics which can lead to dramatic structural shifts such as breathing, swelling, and subnetwork displacements [28, 95]. While deformations in the metal cluster have been implicative of dynamic events, the nature of the linker and its functionality is a major contributor to framework dynamics [29], and play a significant role in determining macroscopic functions such as gas storage and separation, ferroelectricity, spin

[1]Contributions: Damron, Ma, Matzger and Ramamoorthy contributed to the writing of the manuscriptt. Ma and Matzger synthesized and characterized the samples as well ass performed the DFT calculations. Damron collected and analyzed all NMR data. Saalwächter and Kurz aided in the setup of the NMR experiments.

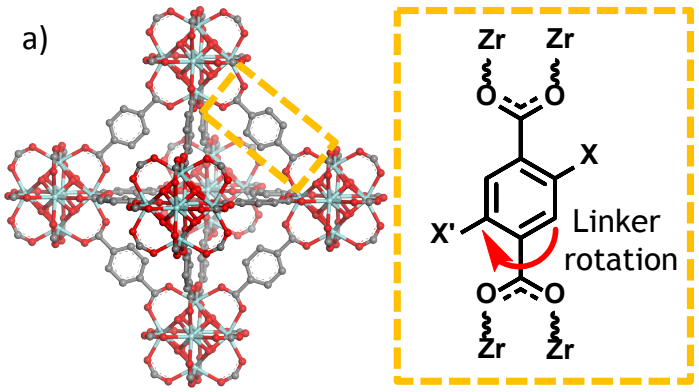

b)

	X	X'
UiO-66	-H	-H
UiO-66-$(CH_3)_2$	-CH_3	-CH_3
UiO-66-$(OH)_2$	-OH	-OH
UiO-66-NH_2	-NH_2	-H
UiO-66-Br	-Br	-H
UiO-67		

FIGURE 4.1: Structure of MOFs. a) UiO-66 structure and scheme of linker rotation. b) A list of UiO type structures investigated in this study

crossover and luminescence in a variety of MOFs [12, 17, 76, 89, 96, 103]. As such, establishing relationships between local dynamics driven by the organic ligands and their chemical modification is of general interest for materials design in MOFs [27, 98]. Though the structural picture of MOFs is most informed by analysis with X-ray diffraction, this yields an essentially static picture, failing to capture the dynamic aspect of the framework. Dynamic measures of crystalline materials are, however, challenging due to the potential of multiple timescales of coordinated motions in the solid state. Many dynamic studies have employed solid-state NMR spectroscopy (ssNMR) through ^{2}H-lineshape analysis to characterize the rotational motion of simple p-phenylene rings within the MOF framework [16, 56, 58, 59, 76, 101]. Separated local field (SLF) solid-state NMR is an alternative, attractive means of dynamic characterization as it utilizes the heteronuclear dipolar coupling as a proxy for molecular dynamics, does not require isotopic labeling, and can be used to characterize motions over a broad dynamic range with atomic resolution [40].

In the following a combination of computation and Dipolar chemical SHIFT correlation (DIPSHIFT) [42, 78] SLF methodology is employed to characterize ligand dynamics in MOFs. For typical heteronuclear dipole-dipole couplings such as ^{13}C–^{1}H and ^{15}N–^{1}H, the experiment is sensitive to a dynamic range spanning 0.1μs-10ms (see Figure 4.2) [18]. Though a number of MOFs are suitable for this approach, we focus on UiO-66 [13] and its derivatives (see Figure 4.1) due to its wide range of potential applications as well as its high thermal and water stability. We demonstrate that the dynamics of the ligands in the framework are heavily impacted by ligand functionalization; specifically, that the variable dynamic behavior arises from differences in interactions with the local chemical environment and is highly responsive to temperature.

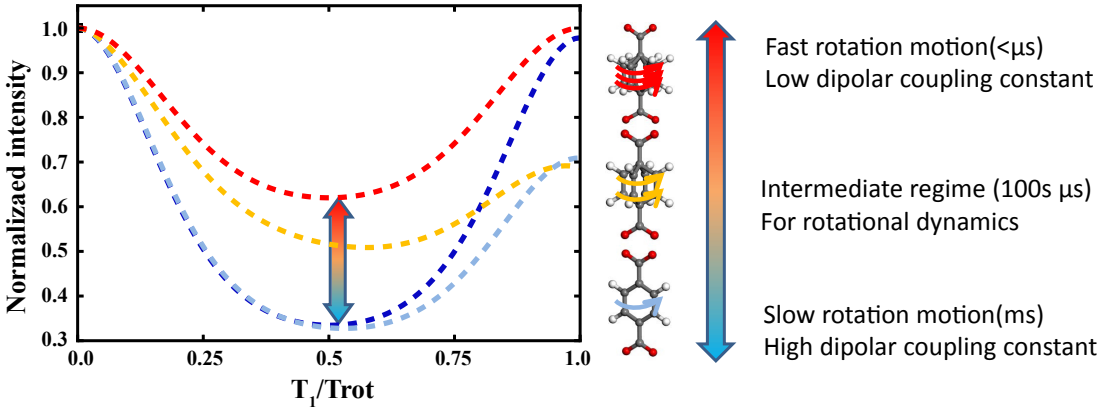

FIGURE 4.2: DIPSHIFT curves as a function of dynamic rate from AW theory (see text). The curves correspond to correlation times (τ_c) of ms or the rigid limit (dark blue), $\tau_c = 350$ μs (light blue), $\tau_c = 5$ μs (yellow), and the fast limit $\tau_c < \mu$s (red).

4.2 DIPSHIFT NMR

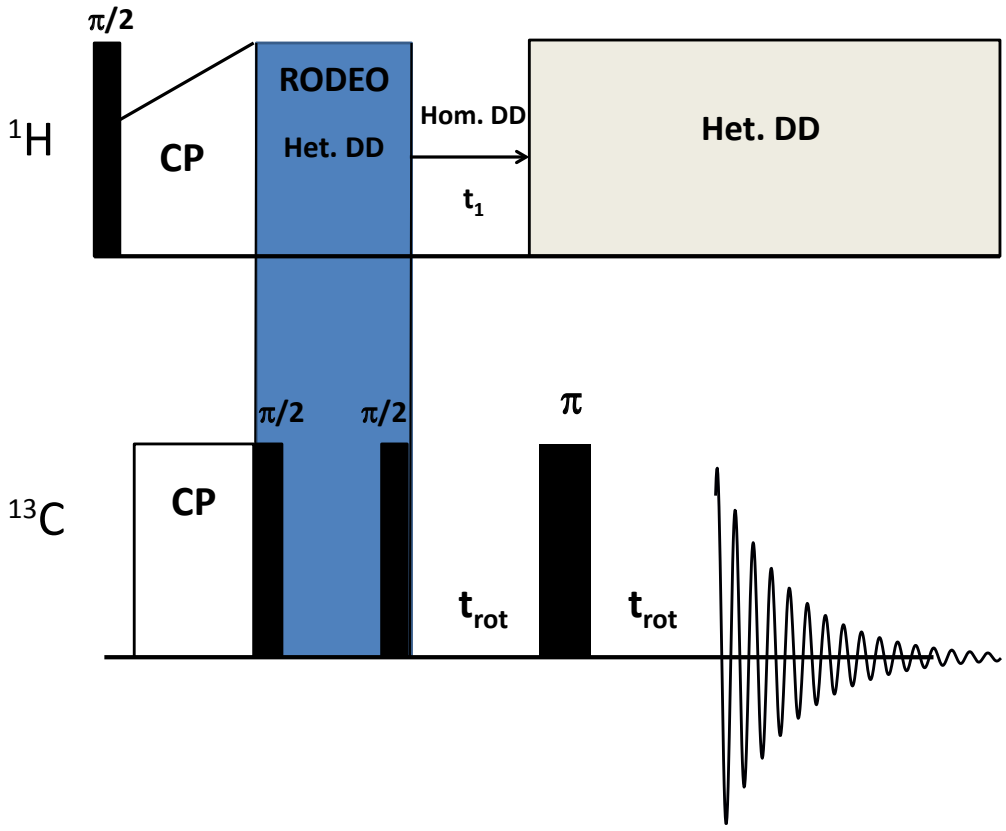

FIGURE 4.3: Radio-frequency pulse sequence for the DIPSHIFT experiment featuring the RODEO delay. See the text for details.

The DIPSHIFT pulse sequence [61, 78] used to measure C-H dipolar couplings is depicted below in Figure 4.3. After preparation of proton magnetization by a $\pi/2$ pulse, it is transferred to carbon-13 nuclei through ramped-CP, which is then followed by an optional z-filter 'rotor directed exchange of orientations' (RODEO) delay [87] to correct for inhomogeneous cross polarization effects when using short CP times [61]. The CH dipolar coupling is then expressed under frequency switched Lee-Goldberg homonuclear decoupling [63] on the proton channel during the t_1 period, ranging from 0 to t_{rot}, where t_{rot} is the rotor period. Heteronuclear decoupling is applied on the ^{1}H channel in the remaining time during the spin-echo (2*t_{rot}) on the ^{13}C channel before acquisition of ^{13}C magnetization. The resultant 2D spectrum correlates the chemical shift with dipolar-dephased intensity mapping out the DIPSHIFT curves. The exhibited DIPSHIFT curves feature well-depths that are roughly proportional to the strength of the C-H dipolar coupling and can be fit with

standard MAS equations to extract the coupling constants. All DIPSHIFT curves in this report were selected from the projections of the aromatic CH group. ^{13}C spectral assignments were given in a previous report [21].

To map the second dimension, the aromatic CH peak is monitored over a regular increment of t_1 to give a 2D correlation between the chemical shift and a modulation in the peak intensity from the heteronuclear ^{13}C–^{1}H dipole-dipole interaction, resulting in the depicted DIPSHIFT curves. The curves can be described by $F(t) = S(t)\exp(-t/T_2)$ with

$$S(t) = cos[\frac{D}{\omega_r}(\frac{1}{4}sin^2\alpha(sin2\gamma(t) - sin2\gamma_0) + \frac{1}{\sqrt{2}}sin2\alpha(sin\gamma(t) - sin\gamma_0)]$$

for the signal under MAS for the dipolar tensor [25, 94]. See Appendix **??** section **??** for more details

T2 is similar to the usual relaxation constant which becomes effective once the motional reorientation of the CH bond is on the order of the inverse coupling constant. $S(t)$ describes the MAS-dependent dipolar fid of an individual CH pair with D the coupling constant, ω_r the MAS frequency, α the angle between the CH bond vector and the rotor axis, and $\gamma(t)$ is the time-dependent angle describing the rotor rotation. γ and α are the Euler angles relating the dipolar tensor the fixed rotor frame. The DIPSHIFT curves can then be fit by F(t) after suitable powder averaging of γ andα between $0 \geq 2\pi$ and $0 \geq \pi$, respectively, along with accounting for the Lee-Goldberg scaling factor in the coupling constant.

4.2.1 Anderson-Weiss Approximation for Diffusive Anisotropic Motions

As shown in detail elsewhere [18, 41], adopting the Anderson-Weiss approximation for anisotropic diffusive motions can be used as an approximate model for the effect molecular motion on dipolar coupled spins under MAS. The dipolar modulated FID accounting for such motions was found to be

$$S(t) = exp[-M_2^{rigid}[S^2(\frac{2}{3}f(\omega_r, 0, t) + \frac{1}{3}(2\omega_r, 0, t) + (1 - S^2)\frac{2}{3}f(\omega_r, 1/\tau_c, t) + \frac{1}{3}(2\omega_r, 1/\tau_c, t)]]$$

with

$$f(\omega_r, 1/\tau_c, t) = \frac{t\tau_c}{1 + (\omega_r\tau_c)^2} - \frac{\tau_c^2[1 - (\omega_r\tau_c)^2]}{[1 - (\omega_r\tau_c)^2]^2} \times [1 - \exp\left(\frac{-t}{\tau_c}\right)cos(\omega_r t)] - \frac{2\omega_r\tau_c^3}{[1 - (\omega_r\tau_c)^2]^2}\exp\left(\frac{-t}{\tau_c}\right)sin(\omega_r t)$$

where τ_c is the correlation time of motion, ω_r the MAS frequency, S^2 is the order parameter defined as $S^2 = M_2^{fast}/M_2^{rigid}$, and M_2 is the second moment of the dipolar field. To approximate τ_c for UiO-66, the parameters were determined with the following procedure. First, M_2^{rigid} was

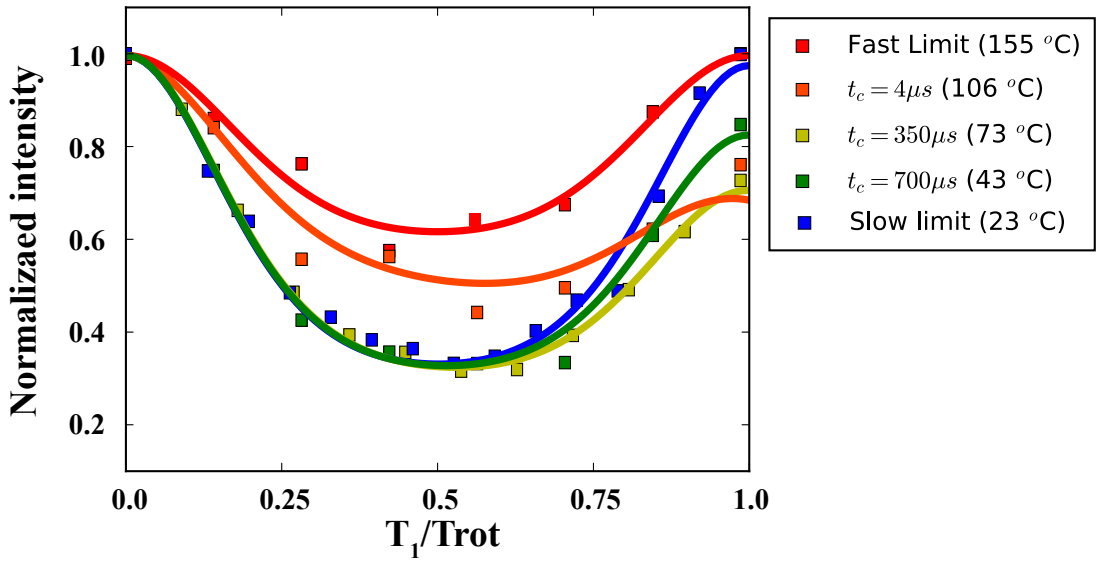

FIGURE 4.4: Model fits of experimentally measure data for UiO-66 at the indicated sample temperature using the Anderson-Weiss formulation for anisotropic diffusive motions.

determined by fitting tc (6ms) and M_2^{rigid} to the 23 °C data (in the slow limit); after which, S^2 was fit to the 155 °C data (fast limit) using the M_2^{rigid} value. These parameters were then used to approximate τ_c for UiO-66 over the temperature range shown in the Figure 4.4 below. As a general comment, M_2^{rigid} and S^2 can be determined *a priori* when the precise geometry and amplitude of motion is known [94]. However, the curve shape is also highly dependent on the distribution of parameters [18] from a mixture in motional modes, such as librations and rotations, making it difficult to model, as was already previously demonstrated for UiO66 [58]. Any attempt to model the precise nature and distribution of motions or extend to the functionalized versions Ui0-66 is outside the scope of this paper. As such, we took an empirical approach for these parameters here, which is sufficient for capturing the general trend.

4.3 Results and Discussion

Terephthalic acid is the most commonly used linker for the construction of MOFs. The phenylene units are symmetric and comprised of four equivalent aromatic ^{13}C-^{1}H bonds making it a suitable candidate for DIPSHIFT measurements. Thus, UiO-66 (Zr6(μ3-O)4(μ3-OH)$_4$(terephthalate)$_6$) (see Figure 4.1) was investigated first to understand the dynamic behavior of a simple phenylene

unit. Using the ^{13}C-^{1}H bond on the phenylene ring as the local field pair, DIPSHIFT measurements were performed on UiO-66 at 23 °C (Figure) resulting in a heteronuclear dipolar coupling constant (D_{CH}) of 16.4 ±0.2 kHz. The experimentally determined DCH value is smaller than the theoretical value for a rigid ^{13}C-^{1}H bond (22 kHz), which is due to dynamic averaging resulting from the motional modes, namely ring rotations and librations, available to p-phenylene within the framework. Given the timescales detected by this approach, the primary event detected is associated with the ring flip although smaller, more rigorous librational modes are also expected to contribute to a lesser degree. By adopting an appropriate model, a correlation time for the motional ring flip can be estimated, which is found to be approximately a few milliseconds falling in "slow" regime dynamics for UiO-66 at 23 °C (see Figure 4.8) and is confirmed by higher temperature experiments (*vide infra*). This result aligns with reports on MIL-53 [60] and MOF-5 [36] both containing p-phenylene units in a sterically unhindered environment. It is notable that the DIPSHIFT data is symmetric around half the rotor period for for UiO-66 at 23 °C, which is a model-free confirmation of slower motional time scales assuming the dynamics are not already in the fast limit. Asymmetries arising from intensity decay due to transverse relaxation effects during the encoding time occur when the molecular motion is accelerated (e.g. temperature induced) to timescales coinciding with the inverse of the coupling constant, known as the 'intermediate motional regime,' as depicted in Figure 4.2 [18].

After establishing the effectiveness of DIPSHIFT based characterization in the UiO-66 sample, we next turned our investigation to ligand functionalized UiO-66 MOFs. Methyl and hydroxyl groups are among the most commonly used functionalities and are particularly relevant for applications such as separations and catalysis [10, 113]. The bulkiness of the methyl group and the hydrogen bonding potential of the hydroxyl groups make them a diametric pair to study their effects on rotational dynamics. Indeed, experiments on UiO-66-$(OH)_2$ (Zr6(μ3-O)4(μ3-OH)4(2,5-dihydroxyterephthalate)6) and UiO-66-$(CH_3)_2$ (Zr6(μ3-O)4(μ3-OH)$_4$(2,5-dimethylterephthalate)$_6$) resulted in dramatically different DIPSHIFT curves from one another (Figure 4.5). UiO-66-$(OH)_2$ gives a higher DCH value (19.0 ±0.5 kHz) than the parent UiO-66 (DCH 16 kHz) indicating reduced mobility; on the other hand, the measured DCH value for UiO-66-$(CH_3)_2$ is only 10 kHz. This stark reduction of the C-H dipolar coupling constant for UiO-66-$(CH_3)_2$ evidences much faster rotary motion than UiO-66, placing it well into the fast regime ($\tau_c < 1$ μs). These simple substitutions cause dramatic changes to the ligand framework interaction which induces 4 orders of magnitude difference in the dynamic rotation. These same trends hold at different temperatures: UiO-66-$(OH)_2$, the least dynamic of the three MOFs, must be heated to 105 °C (60 °C higher than UiO-66) to achieve rotational times on the order of 100 μs (see Figure 4.7. In contrast, the 10 kHz value for the methyl substituent is similar to the plateau value observed for UiO-66 in the fast regime ($\tau_c < \mu$s) at 155 °C (11 kHz). Indeed, when UiO-66-$(CH_3)_2$ is cooled to 6 °C, an asymmetric curve is detected (see Figure 4.12), suggesting that it is in a comparable dynamic

regime to UiO-66 at temperatures 50 °C lower. To complement the experimental results, DFT simulations on a model complex were utilized as a tool to understand the details of rotational dynamics. In the case of UiO-66, a model of $Zr_6O_4(OH)_4(COOH)_{11}(COOC_6H_5)$ bearing a single phenyl rotor was constructed and its geometry was optimized. A relaxed potential energy surface scan was performed with the phenyl ring rotation through its principle axis. A rotational energy barrier of 43.5 kJ/mol was obtained. Despite the simplicity of the model, the obtained activation energy is similar to the one found for MOF-5 [36] and MIL-53 [92]. As with UiO-66, Zr-oxo complexes were constructed and calculations were also performed on models with hydroxyl and methyl functional groups. A high activation energy of 75.3 kJ/mol was found for the model $Zr_6O_4(OH)_4(COOH)_{11}(COOC_6H_5$-o-OH). This is expected to dramatically slow down the ring dynamics which supports the experimental data. A closer inspection of the model shows that the hydroxyl group hydrogen bonds with the carboxylate group, an interaction that must be broken upon rotation (Figure 4.6). The hydrogen bonding explains the high energy barrier and suggests that it is the dominant factor leading to the experimentally observed high C-H dipolar coupling constant and slow rotational dynamics in UiO-66-$(OH)_2$. On the other hand, the model for UiO-66-$(CH_3)_2$ $Zr_6O_4(OH)_4(COOH)_{11}(COOC_6H_5$-o-$CH_3)$ shows a lower activation energy of 33.5 kJ/mol. This reduced energy barrier is attributed to repulsive interactions between the bulky methyl group and the cluster. The simulated energy barrier results are fully consistent with the experimental observations for rotational frequencies: UiO-66-(o-$OH)_2$« UiO-66«UiO-66-(o-$CH_3)_2$.

UiO-66-Br ($Zr_6(\mu3$-$O)_4(\mu3$-$OH)_4$(2-bromoterephthalate$)_6$) and UiO-66-NH_2 ($Zr_6(\mu3$-$O)_4(\mu3$-$OH)_4$(2-aminoterephthalate$)_6$) were also synthesized to test the influence of linker dynamics from another bulky substituent other than a methyl group and a potential hydrogen bond donor. The measured DCH for UiO-66-Br is closer to UiO-66 at 15 kHz but exhibits a slight asymmetry in the curve (Figure 4.5). Despite the higher value than UiO-66-$(CH_3)_2$, the temperature behavior seen in Figure 4.11 of UiO-66-Br also shows that it is in the fast regime limit at room temperature. This suggests that the bromine atom also induces a steric effect which lowers the rotational energy barrier similar to the function brought by methyl groups, but is not as extreme given the higher fast limit value. UiO-66-NH_2 shows a DCH value of 15.3 $\pm$0.3 kHz, value close to UiO-66. However, the temperature behavior is quite constant in a similar temperature range (see Figure 4.9). This behavior could be interpreted as a combination of effects: a balance between a steric effect and the hydrogen bonding potential of the NH2 group. Changing the length of the linker while maintaining the topology, known as isoreticular synthesis, is an important strategy that has been used to increase the surface area of MOFs without altering the topology [117]. Thus UiO-67 ($Zr_6(\mu3$-$O)_4(\mu3$-$OH)_4$(biphenyl-4,4'-dicarboxylate$)_6$) was examined for its larger pore window (9-11 Å) compared to the parent structure UiO-66 (5-7 Å). The measured DCH for UiO-67 is 12.4 $\pm$0.3 kHz, which is smaller than that obtained from UiO-66. The lowering of the rotational energy barrier is attributed to the junction of the biphenyl ring, which has a much lower frictional constraint

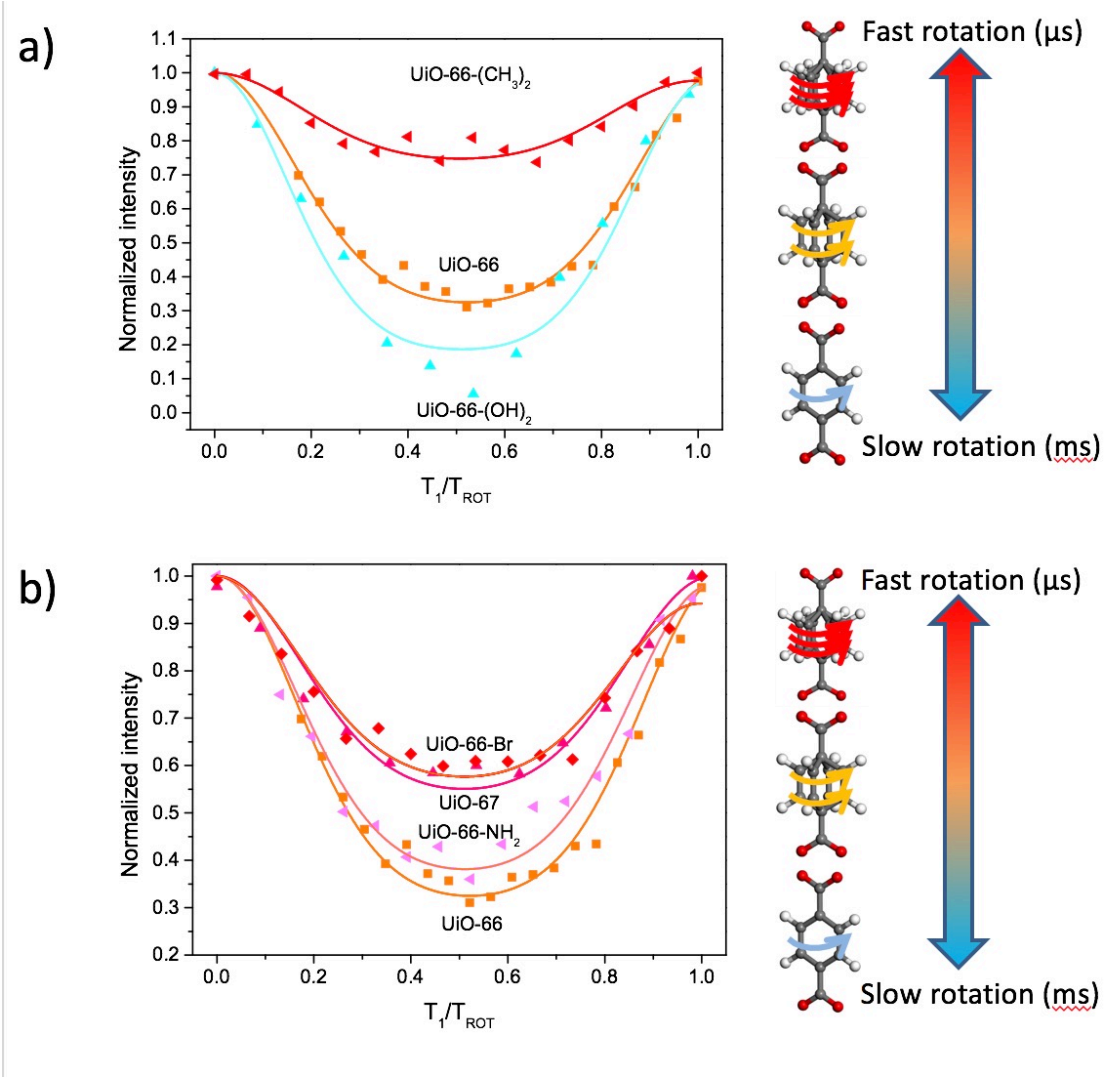

FIGURE 4.5: Effect of substituents on the mobility of phenylene group measured from DIPSHIFT experiments. a) UiO-66, UiO-66-$(OH)_2$ and UiO-66-$(CH_3)_2$; b) UiO-66, UiO-66-NH_2, UiO-66-Br and UiO-67

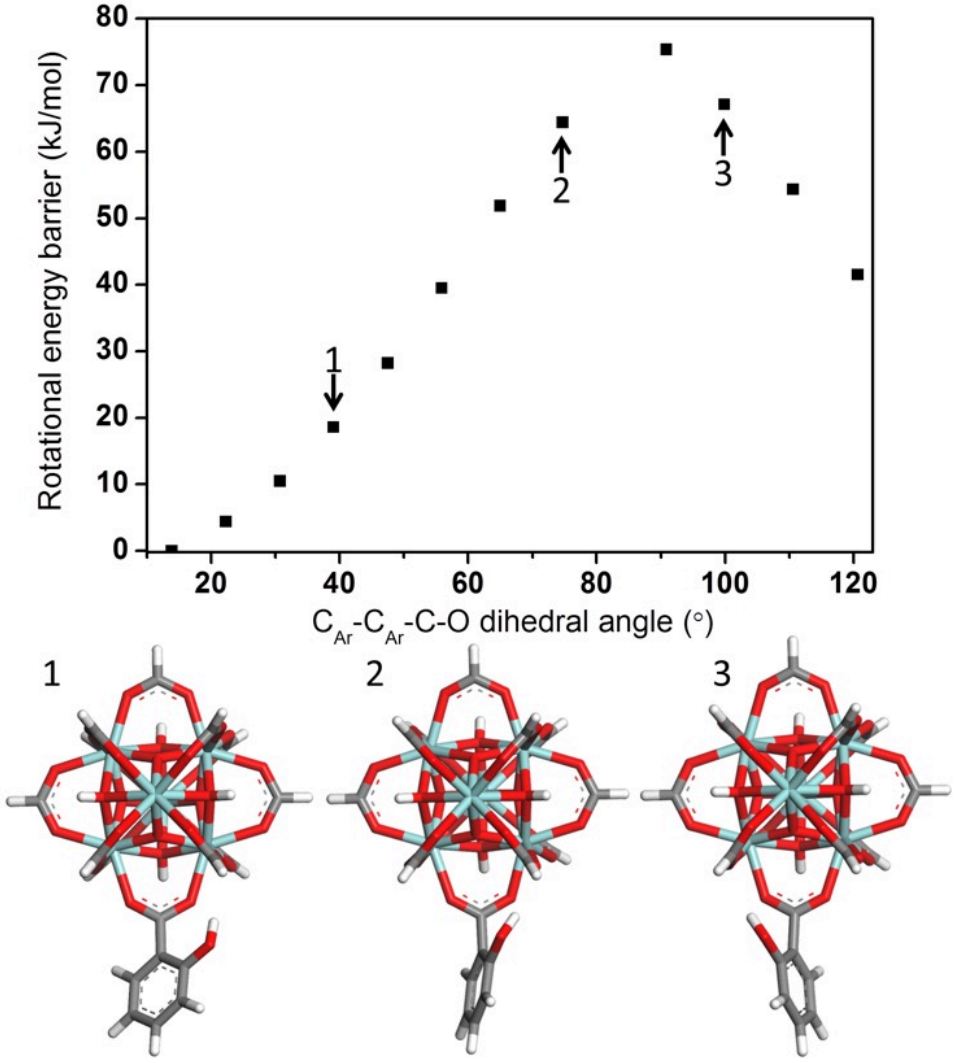

FIGURE 4.6: DFT simulation of rotational dynamics in MOFs. Rotational energy barrier calculation results and snap shot of the model complexes with CAr-CAr-C-O at 40°, 80° and 90°

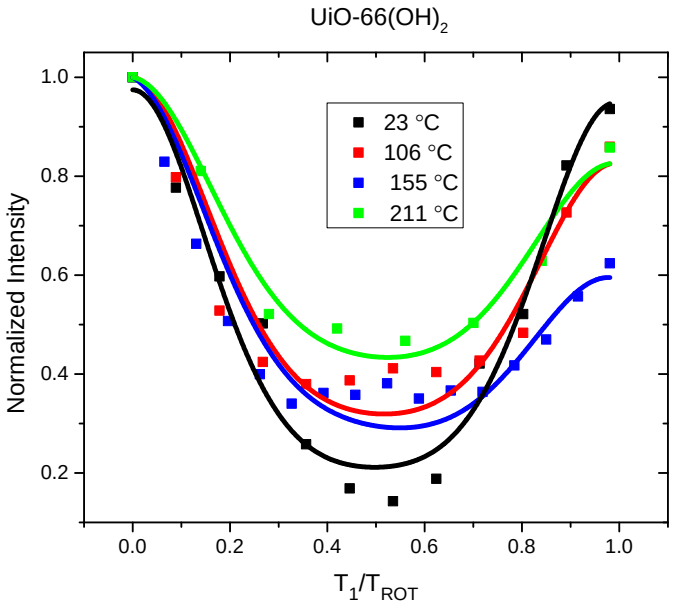

FIGURE 4.7: DIPSHIFT curves for UiO66-$(OH)_2$ at various temperatures spanning most of the intermediate regime. Even at 211 °C the fast limit is not achieved.

vs the Zr cluster interaction. At higher temperature, the depth of the curve decreases substantially, but no intermediate dynamics are detected (Figure 4.10). This is possible in the fast limit regime when the reorientational angle of motion increases; it is plausible that the increased length and biphenyl junction could contribute additional bending modes to facilitate such behavior.

4.3.1 Temperature Dependent DIPSHIFT Measurements

DIPSHIFT curves as a function of temperature were measured for different samples. For UiO-66 and UiO-66-$(OH)_2$. The curves display typical asymmetric behavior marking 'intermediate' dynamic timescales coinciding with the coupling constants upon heating. For UiO66 the intermediate regime is immediately achieved upon heating to 43 °C and is pushed into the fast limit by 155 °C. The intermediate regime for UiO-66-$(OH)_2$, however, does not begin until 100 °C and up to 211 °C is still not quite achieved the fast limit as marked by some residual T2 relaxation at this temperature. For UiO66-(CH_3) and UiO66-Br, only upon cooling is the intermediate regime obtained suggesting fast limit dynamics at room temperature.

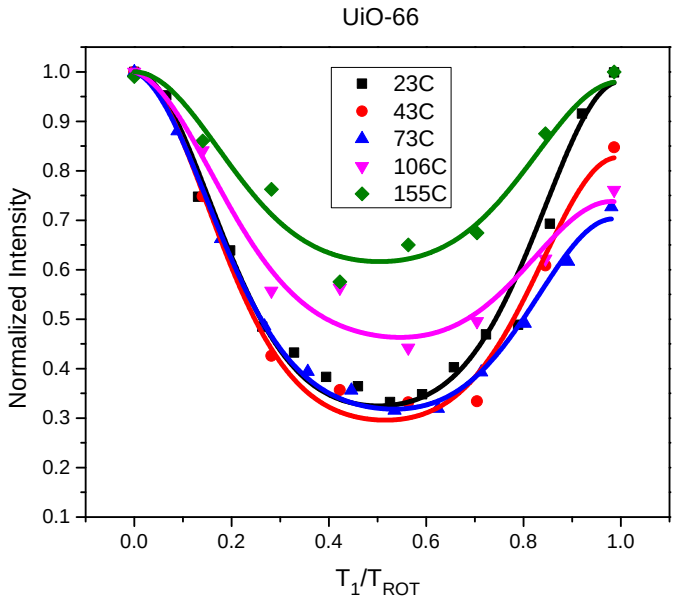

FIGURE 4.8: DIPSHIFT curves for UiO66 at various temperatures spanning the intermediate regime.

4.4 Conclusions

In summary, DIPSHIFT solid-state NMR experiments performed on a series of Zr MOFs with various structural modifications showed different ligand dynamics. The presence of functional groups such as methyl or hydroxyl groups can greatly speed or slow down the rotational motion of the linker in the Zr MOFs. Insights from DFT simulation reveals that such dynamics changes arise from the local chemical interactions such as hydrogen bonding or steric repulsion. It is also found that isoreticular structure expansion and factors such as temperature also influence the ligand dynamics. The insights gained are relevant to applications, where dynamics of the ligands are heavily involved, such as gas separations and kinetically limited processes such as molecular sieving.

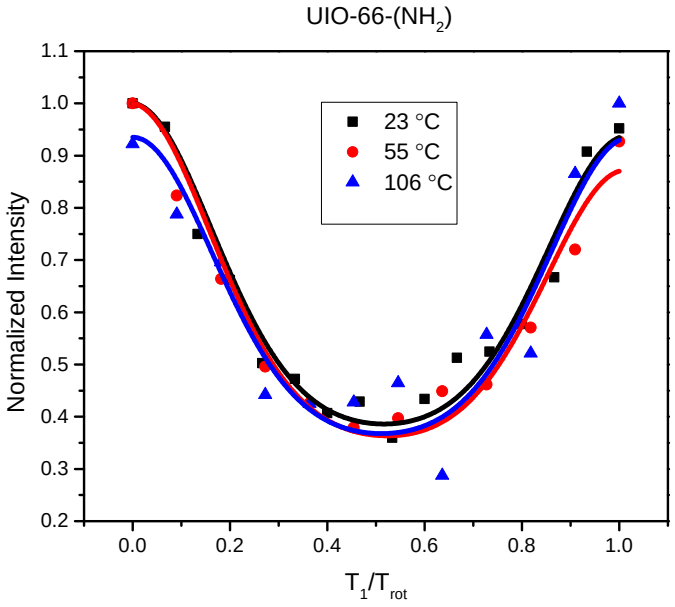

FIGURE 4.9: DIPSHIFT curves for UiO-66-NH_2 at various temperatures. The DIP-SHIFT curves are fairly constant over a wide temperature range.

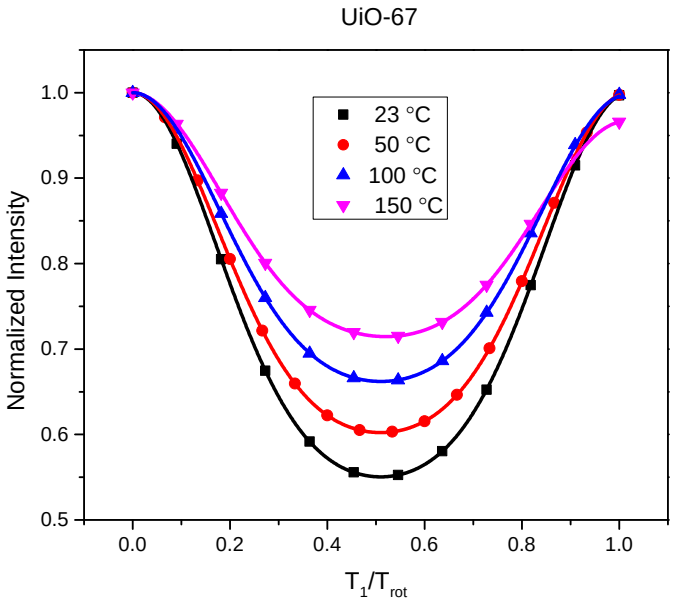

FIGURE 4.10: DIPSHIFT curves of UiO-67 at elevated temperatures. It is particularly notable that the curves depths decrease dramatically from a corresponding 12 kHz D_{ch} at ambient conditions to 9 kHz at 150 °C without exhibiting intermediate motions.

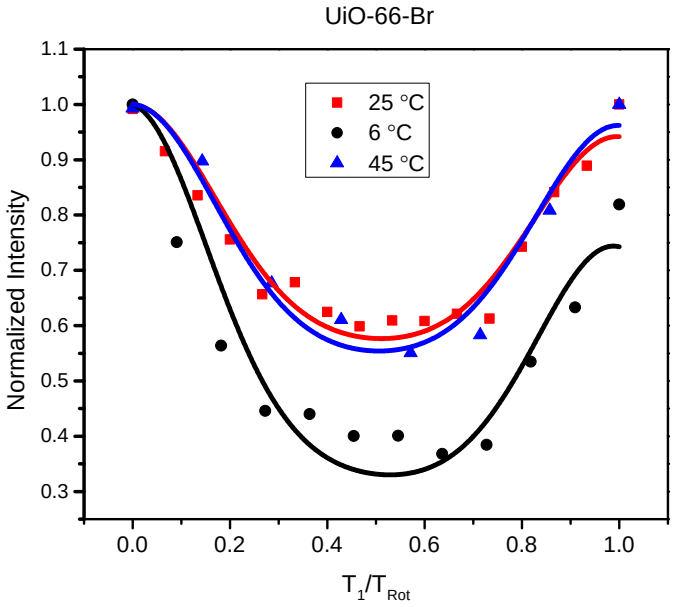

FIGURE 4.11: DIPSHIFT curves for UiO-66-Br at various temperatures. Upon cooling, the curve displays typical intermediate dynamic behavior.

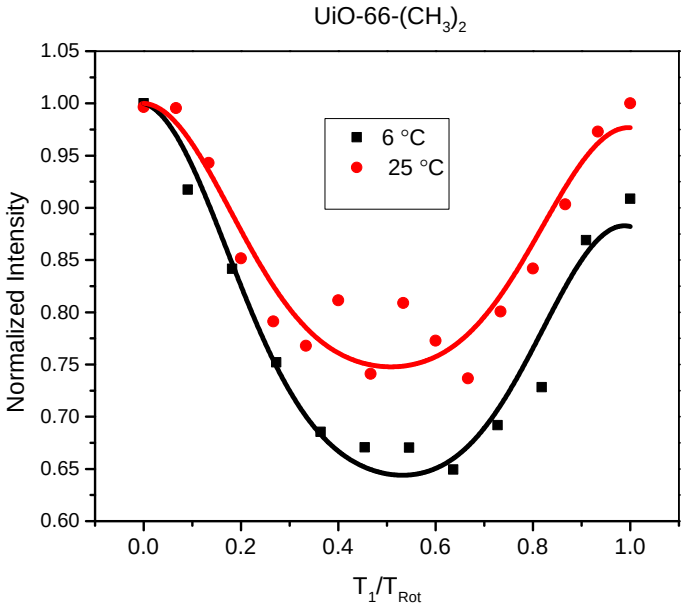

FIGURE 4.12: DIPSHIFT curves for UiO-66-CH_3 at various temperatures. Upon cooling, the curve displays typical intermediate dynamic behavior.

Chapter 5

Conclusions and Future Directions

In this dissertation, current advances in MAS NMR was presented with an emphasis on new methodology and applications. The work utilized MAS spinning frequencies approaching 100+ kHz, which opens up many avenues for ^{1}H based experiments in the solid state. Applications to small crystalline solids were the primary focus of the fast MAS work which demonstrated the ability to achieve atomic resolution in such systems and gain complementary information to X-ray crystallography structures. Polarization transfer from ^{1}H to ^{14}N was shown as a filtering method to greatly simplify the ^{1}H NMR spectra and aid in qualitatively resonance assignment. Advanced recoupling techniques were employed to determine the ^{1}H CSA which was diagnostic of distinct polymorphic arrangements of acetaminophen and hydrate structures in mercaptopurine. The ^{1}H CSA was shown to be highly sensitive to the subtle structural changes including hydrogen bonding and π–π interactions. This provided complementary information to the x-ray crystallography structures further revealing the molecular forces which stabilize and determine the specific structures. These experiments can be used to guide and encourage future experiments in this direction. In particular, with the continued increases in available magnetic field strengths and MAS spinning frequencies, these techniques could prove to be a potent means of molecular exploration. Given that the CSA scales with increasing magnetic fields and the resolution of isotropic resonances increases, subtle trends in inter and intramolecular interactions could be revealed through its determination in an analogous way to this work.

The second portion of the dissertation focused on dynamic measures in the low MAS realm. It was demonstrated that the ^{13}C-^{1}H heteronuclear dipolar interaction is a sensitive probe to characterize dynamic modulations on the μs timescale in MOF structures. A key feature to these experiments was the exploitation of the intermediate motional regime (100 μs timescale), which is difficult to characterize by other methods. Using a particular experiment DIPSHIFT to quantify the dipolar couplings, a series of isoreticular but chemically modified UiO66 MOF structures were interrogated. It was found that that framework dynamics are highly dependent on the nature of

the chemical modification of the framework structure as well as being quite sensitive to temperature. Future directions could utilize this methodology to probe material properties of this system including guest adsorption/diffusion and determine the role that the framework dynamics may play in these properties. Such information could aid in the design of tailored materials for material or technological applications.

This dissertation demonstrates the power of MAS NMR to gain unique information with atomic resolution in solid-state systems. It highlights the key advantages of fast (~60 kHz) and ultrafast (~100 kHz) MAS over other techniques including the ability to probe systems of any molecular size and a variety of solids, and to gain different types of information pertaining to structural or dynamic features. In addition, by utilizing recoupling sequences, MAS allows one to toggle the portions of the spin Hamiltonians to selectively probe those NMR parameters that aren't available in the liquid state.

Appendix A

Experimental Procedures for Mercaptopurine

A.1 Materials

Mercaptopurine monohydrate, deuterated methanol (MeOD), and D_2O were obtained from Acros. Methanol was obtained from Fisher Scientific. All reagents were used without further purification. The purity of the material, from which the hydrates were made, as received from the distributor is 99.5%. Crystals of the monohydrate form were grown from methanol solutions (4 mg/mL) heated to 80 ^{circ}C to dissolve all solids. Solutions were passed through a syringe filter (9 mL) into a 20 mL vial containing 5 mL H_2O. Vials were sealed and yellow block-shaped crystals grew after two days at room temperature. Crystals of the hemihydrate form were grown from methanol solutions (4 mg/mL) heated to 80 ^{circ}C to dissolve all solids. Solutions were passed through a syringe filter (4.5 mL) into a 20 mL vial containing 0.5 mL H_2O. Vials were sealed and yellow needle crystals grew after two days at room temperature. Samples of both the monohydrate and hemihydrate forms were also created using MeOD and D_2O to crystallize samples with deuterated nitrogens and water molecules (See Figure **??**).

A.2 Infrared Spectroscopy

Fourier transform infrared spectroscopy analyses were performed on the hemihydrate and monohydrate forms of mercaptopurine using an attenuated total reflectance accessory (ATR; ThermoNicolet Avatar model 360-FTIR). The scan range was 680 to 4000 cm^{-1}, employing 512 scans with a resolution of 4 cm^{-1}. Samples were analyzed on the ATR stage and the empty stage was used as the blank.

The theoretical IR stretches for both the monohydrate and hemihydrate forms of mercaptopurine were calculated using DFT calculations in Materials Studio 7.0. The same geometry optimizations were performed following the desolvation energy calculations above; first by using Molecular Mechanics (Forcite with COMPASS II) and then DFT (Dmol3) to get an optimized structure of each form. The frequency values of each form were then calculated using DFT methods by way of medium frequency analysis as a property in the Dmol3 calculation using the GGA-PW91 theory. Vibrational analysis was performed, the modes were calculated, and the frequencies were animated to determine the appearance of OH stretches of each hydrate form.

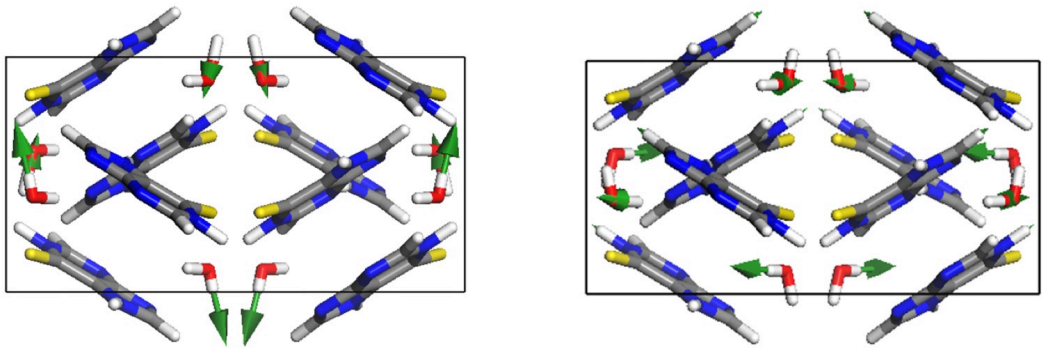

FIGURE A.1: Structural depiction of the calculated stretching for the OH hydrogen bound to sulfur (left, 3428.9 cm^1 experimentally) and the OH hydrogen bound to nitrogen (right, 3160 cm^1 experimentally) for the monohydrate form of mercaptopurine.

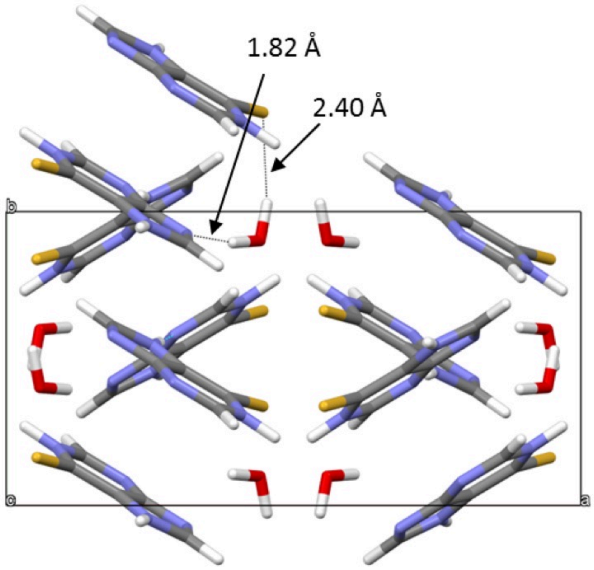

FIGURE A.2: Structural depiction of the experimental unit cell of the monohydrate form of mercaptopurine with the OH hydrogen bonds highlighted (OH$\cdots$S is 2.40 Å, OH$\cdots$N is 1.82 Å).

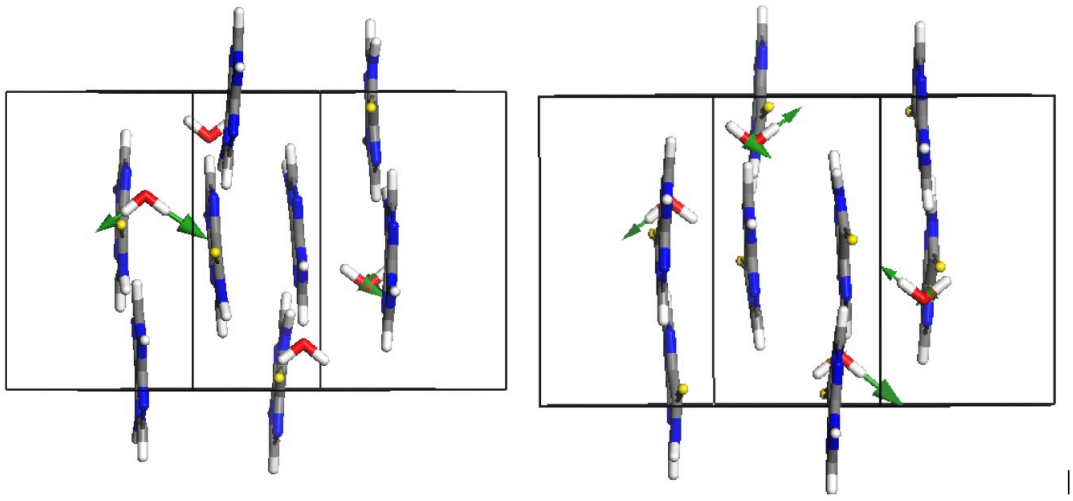

FIGURE A.3: Structural depiction of the symmetric OH stretching (left, 3444.4 cm^1 experimentally) and asymmetric OH stretching (right, 3500.3 cm^1 experimentally) calculated for the hemihydrate form of mercaptopurine.

A.2.1 Charge Density Maps

Computation of the charge density maps of the two tautomeric forms of mercaptopurine were performed in Spartan '14 V 1.1.2. The energy of the initial structure was minimized using molecular mechanics (MMFF). The equilibrium geometry was calculated using density functional theory B3LYP with the basis set 6-31G* in the gas phase. The electrostatic potential map surface was calculated and then displayed. Geometry optimization was first performed on all structures where all atoms except hydrogen were held at a constant position. The unit cell parameters were also held constant, and the calculations were performed using an ultra-fine quality with the COMPASS II force field assigned, which is parameterized for the functional groups present. This initial optimization gave the total energy for the initial crystal structures containing the water molecules. For both the hemi and monohydrate systems, the water molecules were deleted and energy calculations were performed again using the COMPASS II force field assigned to give a total energy for the system after theoretical water loss. Density functional theory calculations were also performed before and after deletion of the water molecules for each structure using two different modules. Preoptimization of the structures was performed using the only H free molecular mechanics method above. For the CASTEP module, ultrafine energy calculations were then performed using the GGA-PW91 theory. This gave the energy for the system containing water molecules. The water molecules were then deleted and energy calculations were performed again using the GGA-PW91 theory to give the energy for the system after theoretical water loss. For the Dmol3 module, fine geometry optimization calculations with the GGA-PW91 theory were performed on the preoptimized structures using the only H free molecular mechanics method above. The water molecules were then deleted and fine energy calculations were performed again using the GGA-PW91 theory to determine the energy for the system after theoretical water loss. Figure A.6 and Table A.1 show the above-mentioned free energy values and the method and results for the calculation of theoretical desolvation energies for each form.

A.3 NMR Spectroscopy

All mercaptopurine CSA/CS data were acquired on a JEOL ECZ600R at 600 MHz ^{1}H Larmor frequency using a JEOL RESONANCE Inc. 0.75 mm double-resonance MAS probe under 90 kHz $\pm$ 20 Hz MAS at room temperature (25 ^{circ}C). Six scans were used with a recycle delay of 120 s and 32 t_1 points in all experiments. The decoupled spectra were obtained with ^{14}N-^{1}H decoupling (99W/117 kHz) using an on-resonance ^{14}N irradiation during the ^{1}H CSA recoupling t_1 period to avoid the reintroduction of ^{14}N-^{1}H dipolar interactions.

For mercaptopurine, additional experiments were performed for resonance assignment. First, the hydrates were prepared using MeOD and D_2O, which replace the water molecules as well as exchange the NH protons revealing only the aromatic resonances in the ^{1}H spectrum. Figure **??** (c

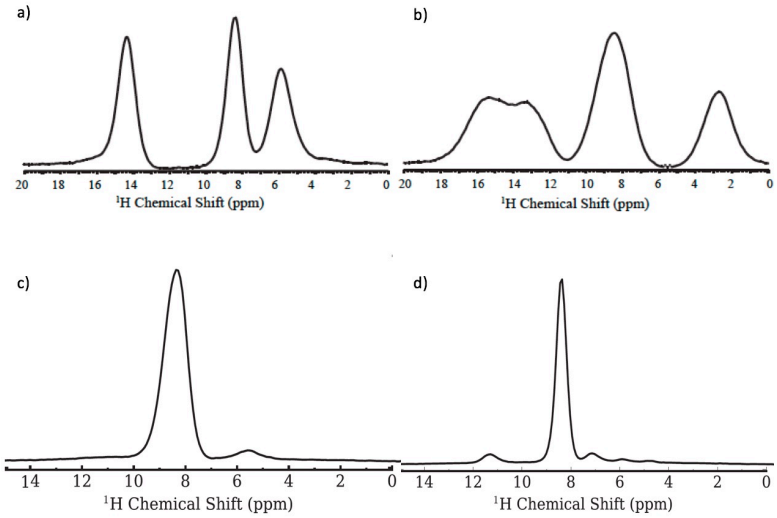

FIGURE A.4: ^{1}H spin-echo of mercaptopurine: (a) monohydrate with H_2O, (b) hemihydrate with H_2O, (c) monohydrate with MeOD/D_2O and (d) hemihydrate with MeOD/D_2O. The H/D exchange was used for confirmation of exchangeable peaks. By this method, all NH and OH hydrogens are replaced with deuterium.

and d) shows the deuterated samples, confirming the aromatic position at slightly above 8 ppm for both hydrate forms. For comparison, the fully protonated 1D spectra are shown in the top part of Figure **??**.

A.4 Theoretical Desolvation Energy Calculations

The crystal structure for the monohydrate form was taken from the Cambridge Structural Database (RefCode: MERPUM) [37]. The crystal structure for the hemihydrate form was solved in house. All modules used were part of the Materials Studio 7.0 suite. Bonds were calculated if necessary and correct bond orders were assigned based on the crystal structures. The following procedures were optimized based on previous literature [75]. Using the concept that the energy of the desolvation process is products – reactants, this gives the following two equations:

$$4H_2O + E2 - E1 = E_{hemidesolv}$$

$$8H_2O + E4 - E3 = E_{monodesolv}$$

Solving for water in the first equation gives:

$$4H_2O = E_{hemidesolv} - (E2 - E1)$$

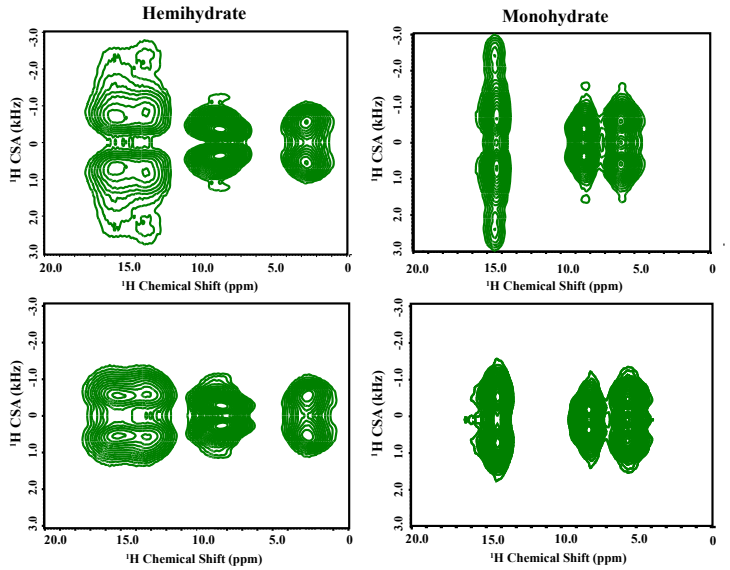

FIGURE A.5: ^{1}H CS/CSA correlation recorded with (bottom) and without (top) 14N decoupling. The downfield resonances are clearly most influenced by the presence of ^{14}N heteronuclear dipolar interaction identifying those as directly bonded.

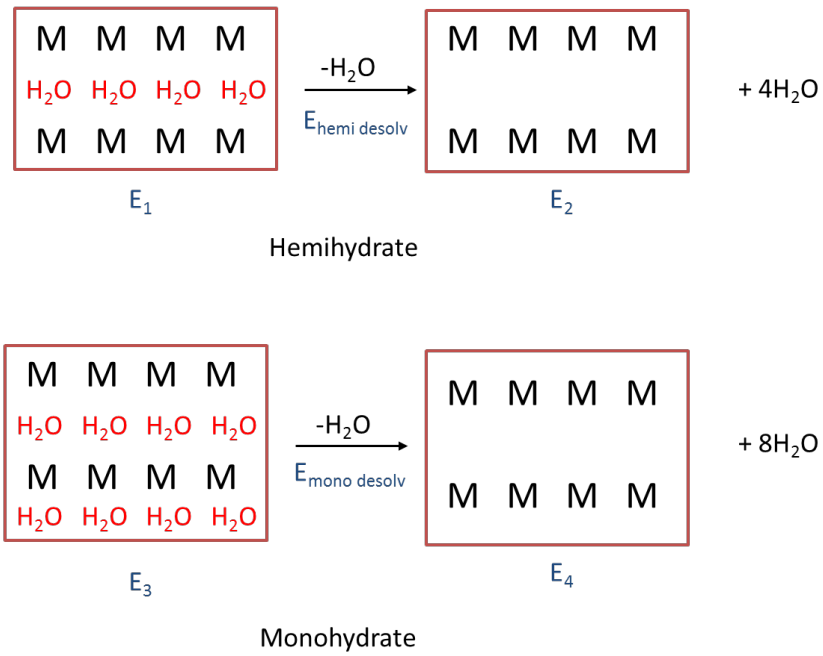

FIGURE A.6: Depiction of how the theoretical desolvation energy calculations were derived.

TABLE A.1: Geometry optimization and energy calculations for the two hydrate forms of mercaptopurine using three different computational methods.

Method	Forcite (E1)	Forcite (E2)	CASTEP (E1)	CASTEP (E2)	Dmol3 (E1)	Dmol3 (E2)
Energy	402.5	164.5	-449,930	406,551	4,259,328	4,067,404
	Forcite (E3)	Forcite (E4)	CASTEP (E3)	CASTEP (E4)	Dmol3 (E3)	Dmol3 (E4)
Energy	637	272	-493,311	-406,483	4,451,283	4,067,335

TABLE A.2: Difference ($E_{monodesolv} - 2E_{hemidesolv}$ in theoretical desolvation energies calculated from the values in table A.1

Computational Method	Forcite	CASTEP	Dmol3
Energy/Unit Cell (kcal/mol)	111	70.6	100
Energy/water (kcal/mol)	14	9	12.6

Multiplying the above equation by a factor of 2 allows one to combine the two equations for hydrates to achieve:

$$E4 + (2[E_{hemidesolv} - E2 + E1]) - E3 = E_{monodesolv}$$

or

$$E4 - E3 - 2E2 + 2E1 = E_{monodesolv} - 2E_{hemidesolv}$$

Table A.1 shows the energies for each structure (E1-E4) calculated by each of the three computational methods. The results of equation 5 for each method are shown in Table S5. The magnitude of each calculation is different, which shows that each computational method takes different interactions into account. However, each method shows that the monohydrate has a higher theoretical desolvation energy, indicating that the water molecules are held in more tightly from an energetic standpoint (i.e. more strongly hydrogen bound) than the water molecules in the hemihydrate.

Appendix B

Experimental Procedures for Acetaminophen

B.1 Sample Preparation/Crystallization

Methanol was purchased from Fisher Scientific. Acetaminophen was purchased from MP Biomedicals.Crystals of the monoclinic form were grown from methanol solutions (100 mg/mL) dissolved at room temperature. Solutions were passed through a syringe filter into a 20 mL vial and colorless block crystals were formed upon evaporation of the solvent at room temperature.

Crystals of the orthorhombic form were grown from DI water solutions (25 mg/mL) heated to 65 °C for 1 hour to dissolve all solids. Solutions were passed through a syringe filter (2 mL) into a 4 mL vial and allowed to cool to room temperature. One vial at a time was placed in a recirculating bath containing a 50:50 mixture of ethylene glycol and water held at 0 °C. After 4 hours, the vial was removed and tapped on the benchtop. This disturbance initiates nucleation, and the vial was placed back in the chiller for another hour. Colorless needles were formed and must be isolated (by pipetting dropwise onto filter paper to remove excess solution quickly) to prevent transformation to the monoclinic polymorph.

B.2 Infrared Spectroscopy

Fourier transform infrared spectroscopy experiments were performed on the monoclinic and orthorhombic forms of acetaminophen using an attenuated total reflectance accessory (ATR; ThermoNicolet Avatar model 360-FTIR). The scan range was 680 to 4000 cm^{-1}, employing 512 scans with a resolution of 4 cm^{-1}. Samples were analyzed on the ATR stage and the empty stage was used as the blank.

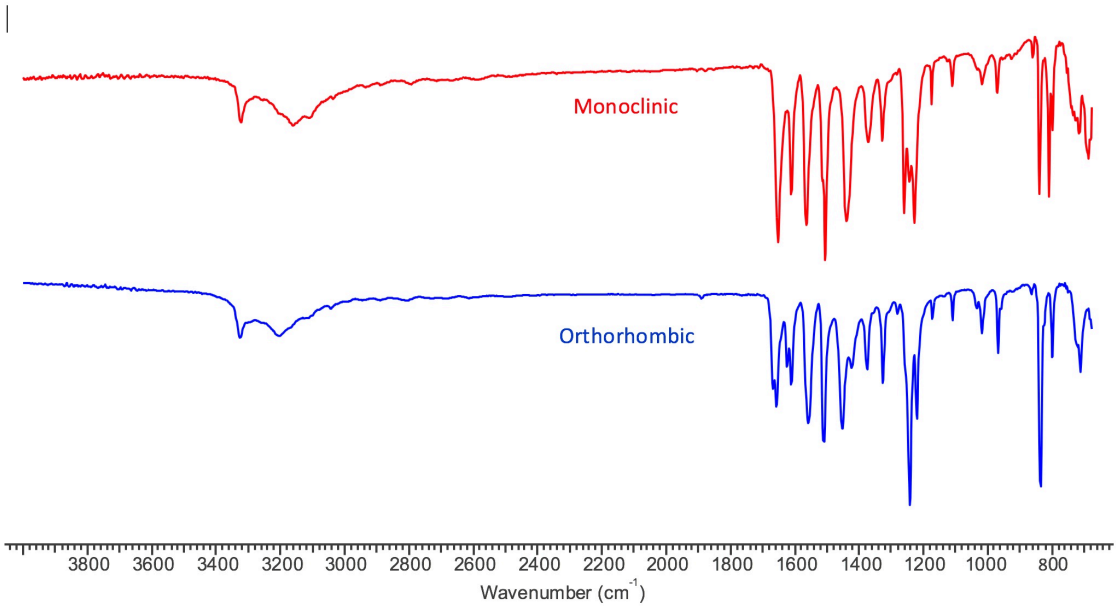

FIGURE B.1: IR spectra of monoclinic (top) and orthorhombic (bottom) forms of acetaminophen.

B.3 Raman Spectroscopy

Raman spectra were collected using a Renishaw inVia Raman Microscope equipped with a Leica microscope, 633 nm laser, 1800 lines/mm grating, 50 μm slit, and a RenCam CCD detector. Spectra were collected in extended scan mode with a range of 100-3200 cm^{-1} and then analyzed using the WiRE 3.4 software package (Renishaw). Calibration was performed using a silicon standard.

B.4 Solid-State NMR

All NMR experiments were conducted at 14.1 T on a 600-MHz JEOL solid-state NMR spectrometer (JEOL ECA600II) operating at ^{1}H and ^{13}C Larmor frequencies of 600.17 MHz and 150.91 MHz, respectively, using either a 0.75-mm double-resonance Ultrafast MAS probe or a 1.0-mm double-resonance Ultrafast MAS probe (JEOL RESONANCE Inc., Tokyo, Japan). All measurements were carried out at ambient temperature using about one mg of acetaminophen samples packed separately into ultrafast MAS zirconia rotors. One-dimensional (1D)^{1}H MAS spectra were recorded in 3 scans using a rotor-synchronized spin-echo (τ_r-π-τ_r) pulse sequence with a $\pi/2$ ^{1}H pulse of 0.8 μs and a recycle delay of 120 s at multiple 90 kHz MAS frequency. The 1D ^{13}C CP MAS NMR spectrum of the orthorhombic acetaminophen was recorded in 416 scans under 70 kHz MAS

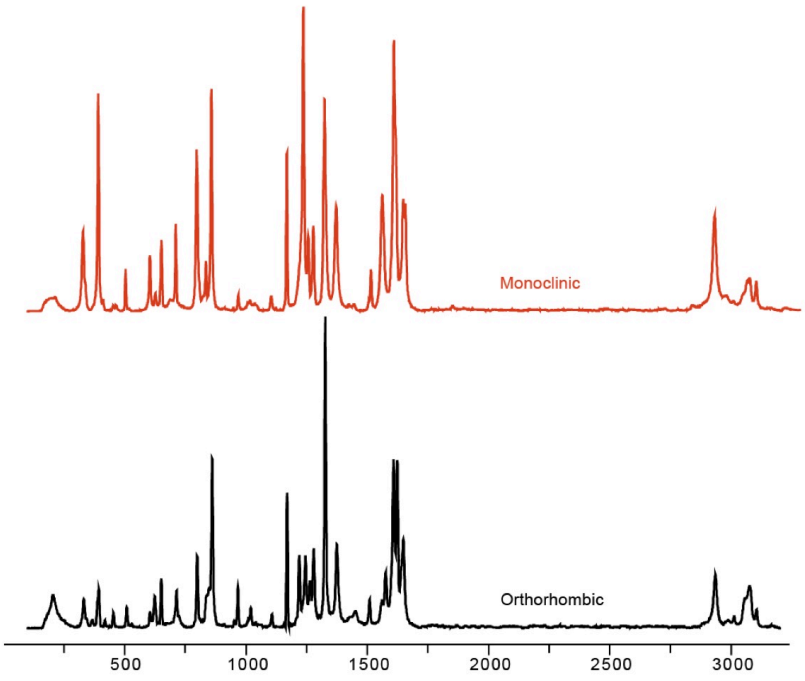

FIGURE B.2: Raman spectra of monoclinic (top) and orthorhombic (bottom) forms of acetaminophen

with a ^{1}H excitation pulse of 1.5 μs and a recycle delay of 250 s using a ramped-amplitude cross-polarization (Ramp-CP)[71] pulse sequence during an acquisition period of 54 ms with a 2.6 ms cross-polarization contact time. The^{1}H-detected ^{13}C–^{1}H 2D HETCOR spectrum of the orthorhombic acetaminophen was recorded at 70 kHz MAS with a 1.2 μs $\pi/2$ ^{1}H pulse using a recycle delay of 140 s and 128 t_1 increments (t_1 max = 3.392 ms) with 8 scans per increment during a t_2 acquisition time of 20.48 ms. Contact times of 2.6 and 0.5 ms were respectively used for the ^{1}H to ^{13}C and ^{13}C to ^{1}H ramped CP steps. The HORROR condition was applied for a duration of 5 ms with 36.15 kHz^{1}H RF amplitude to remove all the residual transverse magnetization on protons.

The 2D ^{1}H/^{1}H CSA/CS correlation spectra for the monoclinic and orthorhombic forms of acetaminophen were collected using a γ-encoded $R18_8^7(270°90°)$ symmetry-based pulse sequence depicted in Chapter 2 Figure 3.3 and introduced in detail there. The 2D CS/CSA NMR data were acquired using an acquisition time of 10.24 ms with 1024 t_2 complex points. Six scans for every t_1 point with a total of 32 t_1 increments were used to obtain the amplitude-modulated signal at every period. Prior to the application of symmetry-based ^{1}H CSA recoupling pulses, a relaxation delay of 120 s was used for both samples. The decoupled spectra were obtained with ^{14}N-^{1}H decoupling (99W/117 kHz) using an on-resonance (121 ppm / 5.25 kHz) ^{14}N continuous wave irradiation during the^{1}H CSA recoupling t_1 period to avoid the reintroduction of ^{14}N-^{1}H dipolar interactions. The ^{14}N shifts (on-resonance conditions) were measured from 2D ^{14}N/^{1}H HMQC correlation experiments for both polymorphs. 2D ^{1}H/^{1}H CSA/CS correlation data were processed using Delta NMR software (JEOL RESONANCE Inc., Tokyo, Japan) by applying a Fourier transform after zero-filling in the direct frequency domain. A DC balance (the average of the final 1/8th points of the FID in the t_1 dimension is subtracted from the total data points) prior to zero-filling followed by a real Fourier transform in the indirect frequency domain to get rid of the DC offset effects that result in a narrow center peak with a significant intensity, which affects the^{1}H CSA line shapes through the wiggles originating from this center peak.

B.4.1 Simulations

Numerical simulations using SIMPSON [8] were carried out for a single ^{1}H spin system in the absence of RF field inhomogeneity to fit the experimental ^{1}H CSA line shapes obtained from the spectral slices parallel to the^{1}H CSA dimension at ^{1}H isotropic chemical shift values of monoclinic and orthorhombic forms of acetaminophen. In these simulations, powder averaging was achieved using 678 (α, β) orientations and 26 γ angles at a ^{1}H Larmor frequency of 600 MHz under 90 kHz MAS by implementing γ-encoded symmetry-based sequence $R18_8^7(270°90°)$. To get the best fit, the simulated^{1}H CSA line shapes were adjusted by applying a vertical intensity scaling and single exponential line-broadening function.

B.4.2 Resonance Assignment

The ^{1}H and ^{13}C NMR resonance assignments for the monoclinic form were previously reported by Zhou and Rienstra under 40 kHz MAS [119]. In a similar fashion, the assignments of proton and carbon resonances in the orthorhombic form can be performed. To this end, we measured the 2D ^{1}H-detected ^{1}H–^{13}C HETCOR NMR spectrum under MAS of 70 kHz for the orthorhombic polymorph as well as the ^{1}H–^{13}C cross polarization spectrum, which are shown in Figure B.3. Shown also in Figure B.3 (A and B) are the 1D ^{1}H MAS NMR spectra of the two forms under 90 kHz MAS. Figure B.3 (C and D) shows the assignments of the proton and carbon atoms in the orthorhombic form of acetaminophen. The resonance at 170 ppm in the ^{13}C dimension of the HETCOR spectrum corresponds to the carbonyl carbon, reflected by its strong cross-peak with the methyl protons, which in turn exhibit a cross-peak with the methyl carbon at (2.0, 24.3) ppm. The amide proton is assigned to 9.0 ppm based on its cross-peaks with the carbonyl carbon and the aromatic quartenary carbon *a*, which is in turn assigned to 131 ppm. Based on their cross-peak with carbon *a*, the aromatic protons *b* and *f* are assigned to 7.2 and 4.9 ppm, respectively. The OH proton is assigned to 9.4 ppm as it shares a single cross-peak with the quartenary carbon *d* at (9.4, 152.4) ppm, which in turn shares a cross-peak with protons *c* and *e* at 4.9 and 6.5 ppm. According to the crystal structure of the orthorhombic acetaminophen, the carbonyl group lies closely in the plane of the phenyl group, and therefore is spatially closer to either proton *b* or *f*. From DFT calculations, we confirm that the closest phenyl proton is in fact the most downfield shifted. If we take the orientation of the molecule presented in Figure B.3, then proton *b* is the most downfield phenyl proton. Accordingly, the assignment for the phenyl protons would most likely be *b* at 7.2 ppm, *e* at 6.5 ppm, and *c/f* at 4.9 ppm.

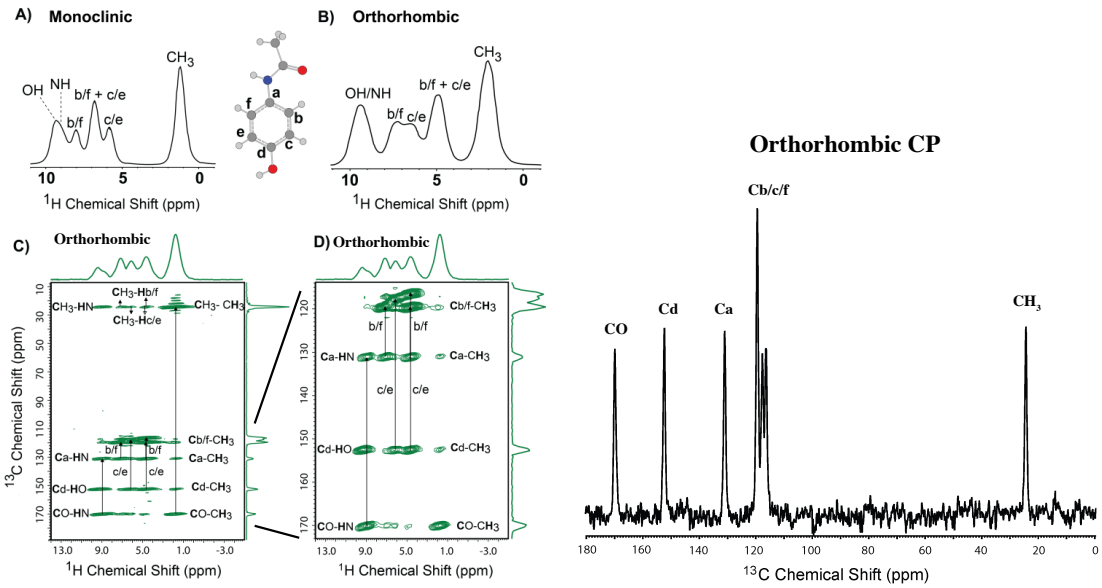

FIGURE B.3: A) and B) ^{1}H MAS NMR spectra of both polymorphic forms with assignments. C) ^{13}C–^{1}H Two-dimensional HETCOR NMR spectrum of orthorhombic and D) the HETCOR spectrum for the aromatic region alone. Right is the ^{13}C CP-MAS NMR spectrum of the orthorhombic obtained at 70 kHz MAS.

B.4.3 The Role of ^{14}N–^{1}H Heteronuclear Dipolar couplings

SIMPSON simulations of the CSA line-shapes were performed including the^{1}H–^{14}N heteronuclear couplings from the nearest neighbor for each resonance and compared to CSA-only line-shapes using the experimentally determined CSA parameters for the orthorhombic (Figure B.4) and the monoclinic (Figure B.5). The dipolar coupling constants used were computed from the crystal structure based on the static distances between the nuclei. The influence of the heteronuclear couplings, to a greater or lesser extent, causes distortions by smoothing the line-shapes. This is the source of the erroneous CSA fits described in the main text without decoupling. In both polymorphs, the aromatic resonances are more influenced by the inclusion of the couplings in the simulations. Experimentally, however, the influence is found to be more prevalent for the orthorhombic, which we attribute to differing contributions of the molecular dynamics. A more rigid orthorhombic crystal (or more dynamic monoclinic molecule) explains this behavior. It is important to note that the line-shapes below are a simplification given that they do not account for longer range effects of even other close by ^{14}N interactions. As such, they should not reflect the exact line-shape of the experiment but give the general influence of the interaction. A rather

broad coupling was found for the NH resonance and shown in the bottom right of Figures B.4 and B.5 confirming that the satellite peaks in main text are indeed from the NH spin pair.

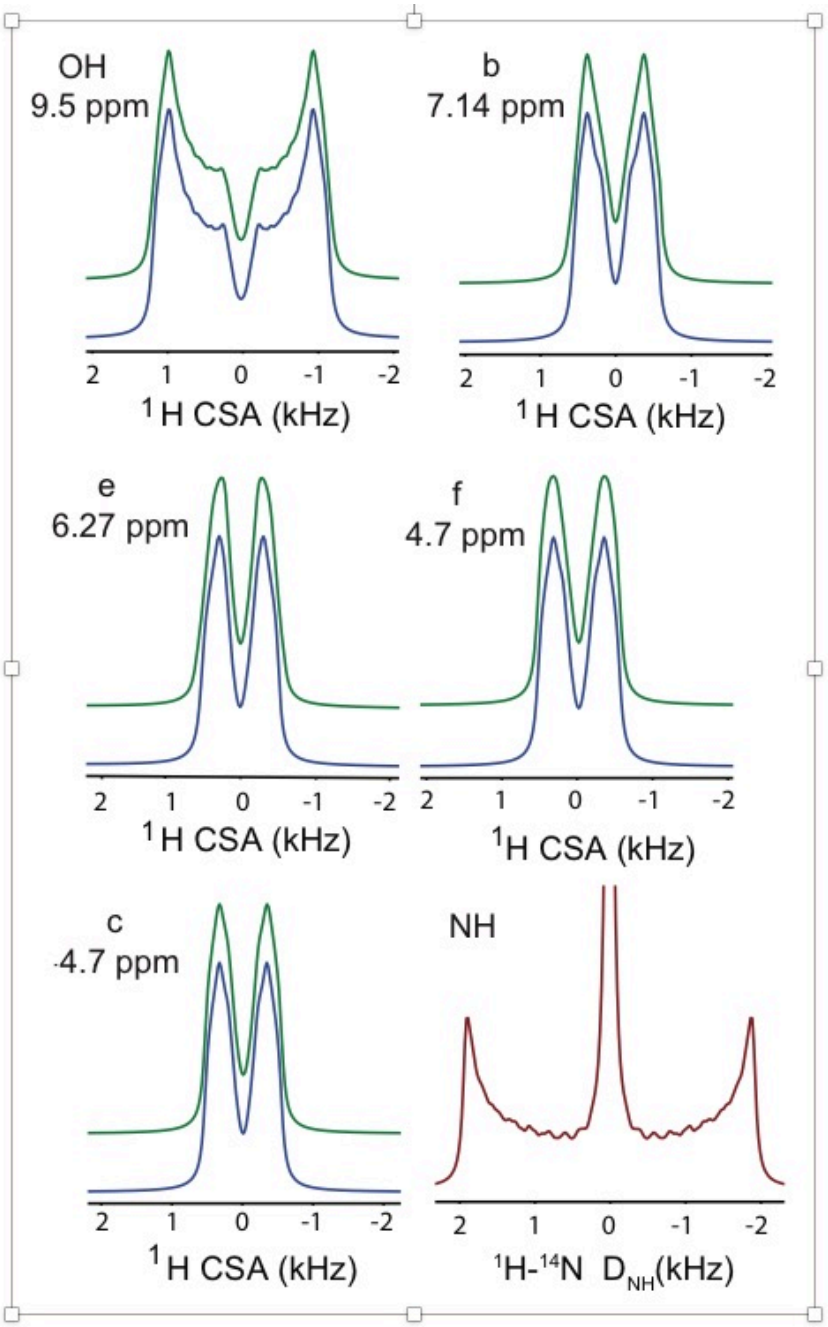

FIGURE B.4: SIMPSON simulations comparing ^{1}H CSA line-shapes with (green) and without (blue) ^{1}H-^{14}N heteronuclear couplings for the orthorhombic polymorph of acetaminophen. The spectrum for the dipolar coupling alone is included in the bottom right for the NH resonance.

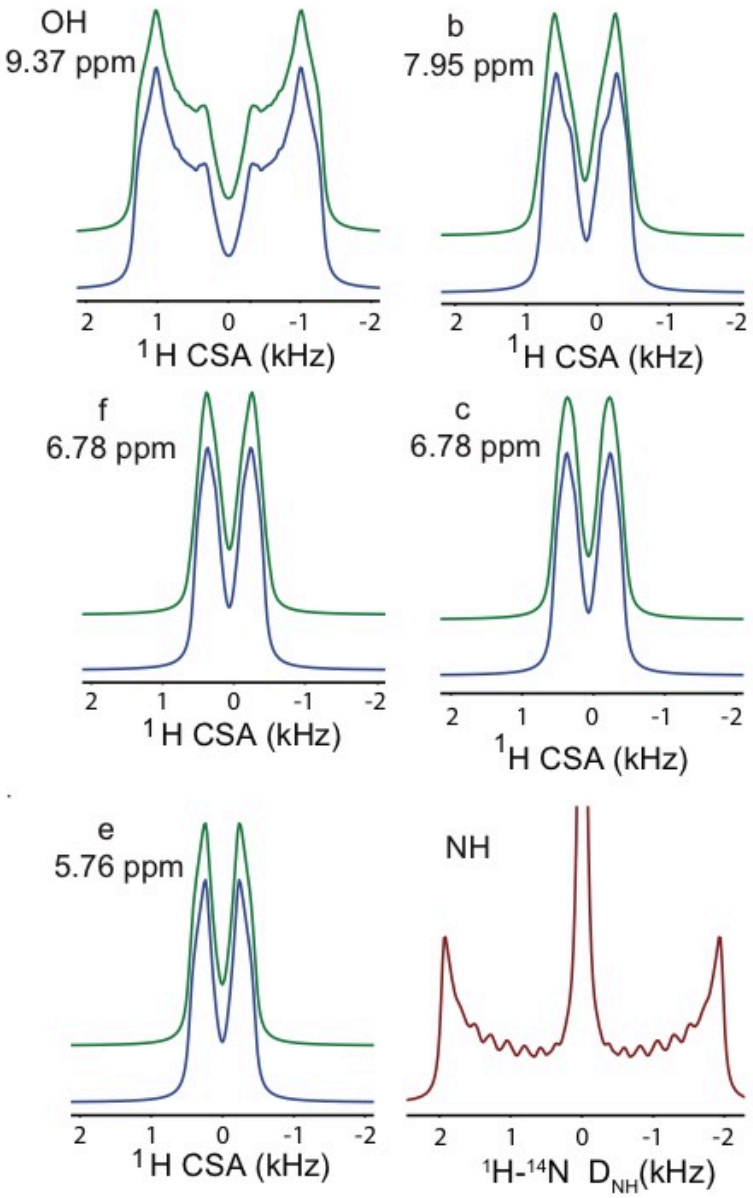

FIGURE B.5: SIMPSON simulations comparing ^{1}H CSA line-shapes with (green) and without (blue) ^{1}H-^{14}N heteronuclear couplings for the monoclinic polymorph of acetaminophen. The spectrum for the dipolar coupling alone is included in the bottom right for the NH resonance.

B.4.4 Computational Details

Quantum chemical calculations were performed using Gaussian 09 program [31]. Calculations of the ^{1}H magnetic shielding tensors were carried out on molecular clusters constructed using atomic coordinates from the single-crystal X-ray crystal structure for each polymorph [80]. For each polymorph, this cluster consists of 15 molecules (a total of 300 atoms), where a central acetaminophen molecule is surrounded by its nearest neighbors up to a distance of 15 Å. The hydrogen atom positions were optimized with density functional theory (DFT) using the Becke-Lee-Yang-Parr three-parameter exchange-correlation functional (B3LYP)[11, 62] and the 6-31G(d,p) basis function for all atoms. The proton magnetic shielding tensors were calculated for the optimized structures with DFT at the B3LYP/6-311G(d,p) level for all atoms using the Gauge-Including Atomic Orbital (GIAO) method [22, 114]. The magnetic shielding tensor components of the protons in the central molecule, as calculated in Gaussian 09, were converted to chemical shift tensor components using the isotropic shielding constant of a fully optimized tetramethylsilane (TMS) calculated at the same level of theory $\delta_{ii}^{calc} = \sigma_{iso}^{TMS} - \sigma_{ii}^{calc}$.

Appendix C

Experimental Procedures for UiO66

C.1 Sample Preparation and Synthesis

C.1.1 Reagents

Zirconium tetrachloride (Stem, sublimed grade), terephthalic acid acid (Fisher Scientific, 98%), 2-aminoterephthalic acid (Acros Organics, $\geq$99%), 2-bromoterephthalic acid (Acros Organics, 95%), 2,5-dimethylterephthalic acid (TCI, $\geq$97%), 2,5-dihydroxylterephthalic acid, biphenyl-4,4'-dicarboxylic acid (Acros Organics, 98%), dimethylformamide (DMF, Fisher Scientific, $\geq$99.5%) and concentrated HCl (Fisher Scientific, ACS grade) were used as received.

C.1.2 MOF Synthesis

All UiO series MOFs in this paper were synthesized according to a published procedure [52].

C.1.3 Powder X-ray Diffraction

The powder X-ray data of all activated MOFs were collected with a Bruker D8 advance diffractometer equipped with a 60 mm sealed Göbel mirror and a LynxEye linear position sensitive detector, depicted in Figure C.1 and Figure C.2 The Cu-Kα X-ray source was operated at 40 kV and 40 mA. Samples were evenly dispersed on a low-background quartz plate before measurements.

C.1.4 Gas Sorption Measurements

Gas sorption experiments (Figure C.3 were carried out at 77 K using a NOVA 4200 by Quantachrome Instruments (Boynton Beach, Florida, USA). Ultra-high purity N_2 (99,999%) was purchased from Cryogenic Gasses and used as received. The obtained isotherm was analyzed using NOVAwin software. The relative pressure range for calculating the surface area satisfies the criteria for applying BET theory [111].

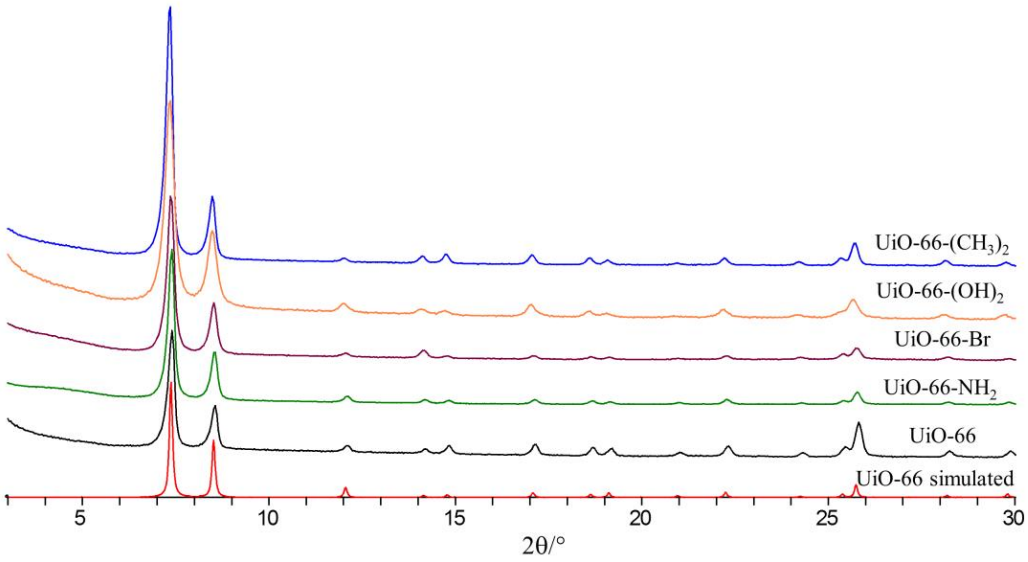

FIGURE C.1: Simulated and experimental powder X-ray diffraction patterns for the UiO-66 MOF series investigated in this study.

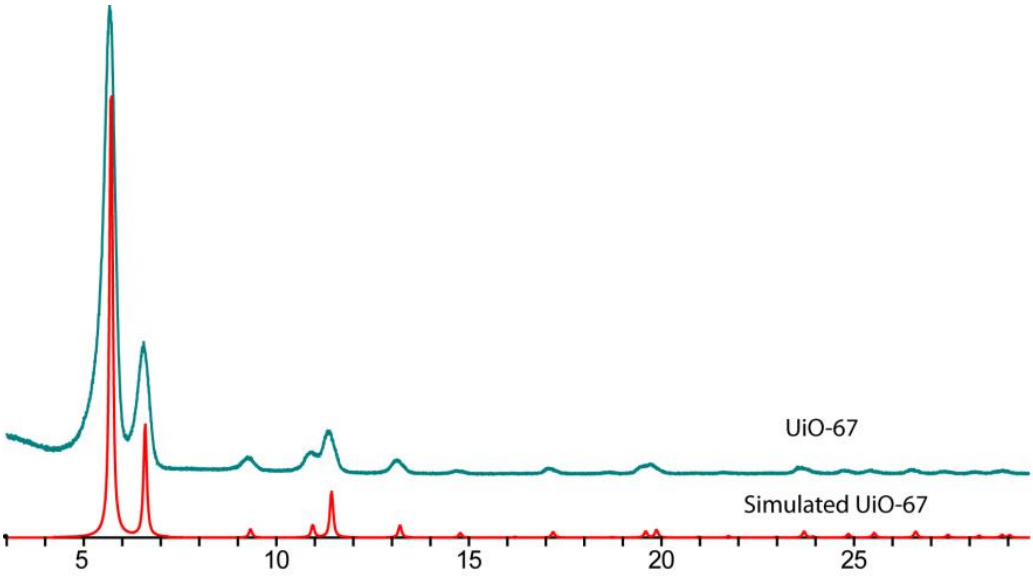

FIGURE C.2: Simulated and experimental powder X-ray diffraction patterns for UiO-67.

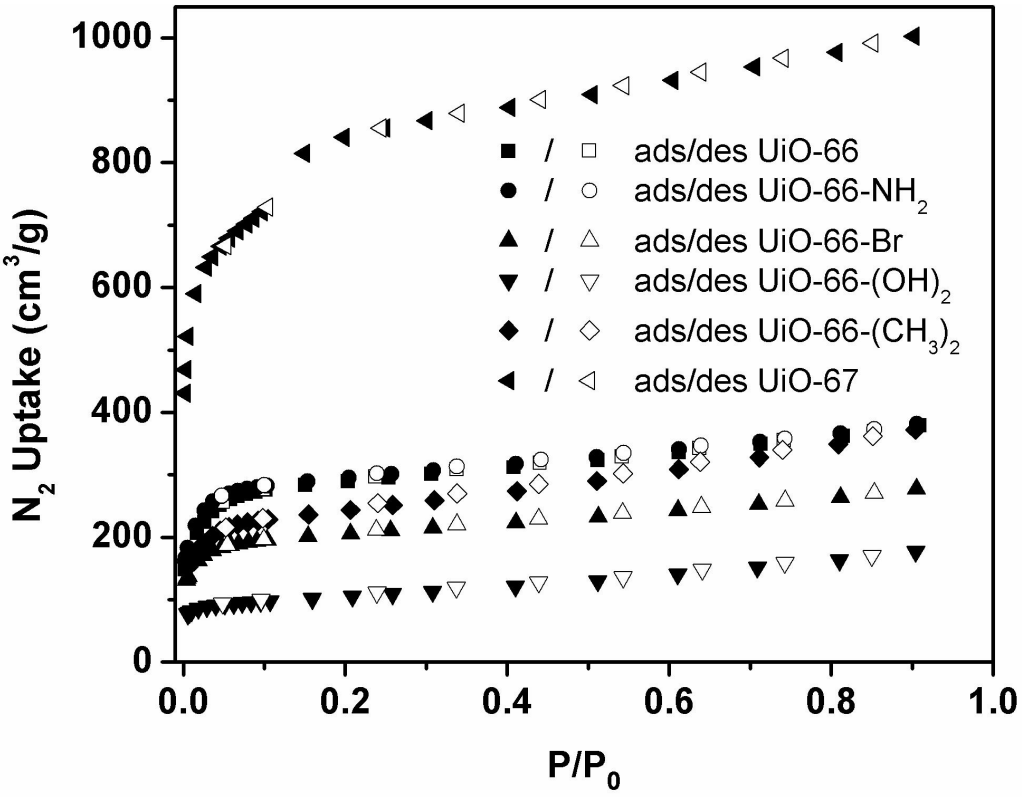

FIGURE C.3: N_2 isotherm plot for UiO series of MOFs used in this study

C.2 DFT Calculations

All DFT calculations were performed using Gaussian 09 with B3LYP functions and the LANL2DZ basis set. All model complexes were initially constructed by modifying a UiO-66 crystal structure leaving only one Zr_6 cluster and a single phenyl rotor with a general formula $Zr_6O_4(OH)_4(COOH)_{11}(COOC_6H_5)$. Functional groups were then added to the phenyl rotor if required.

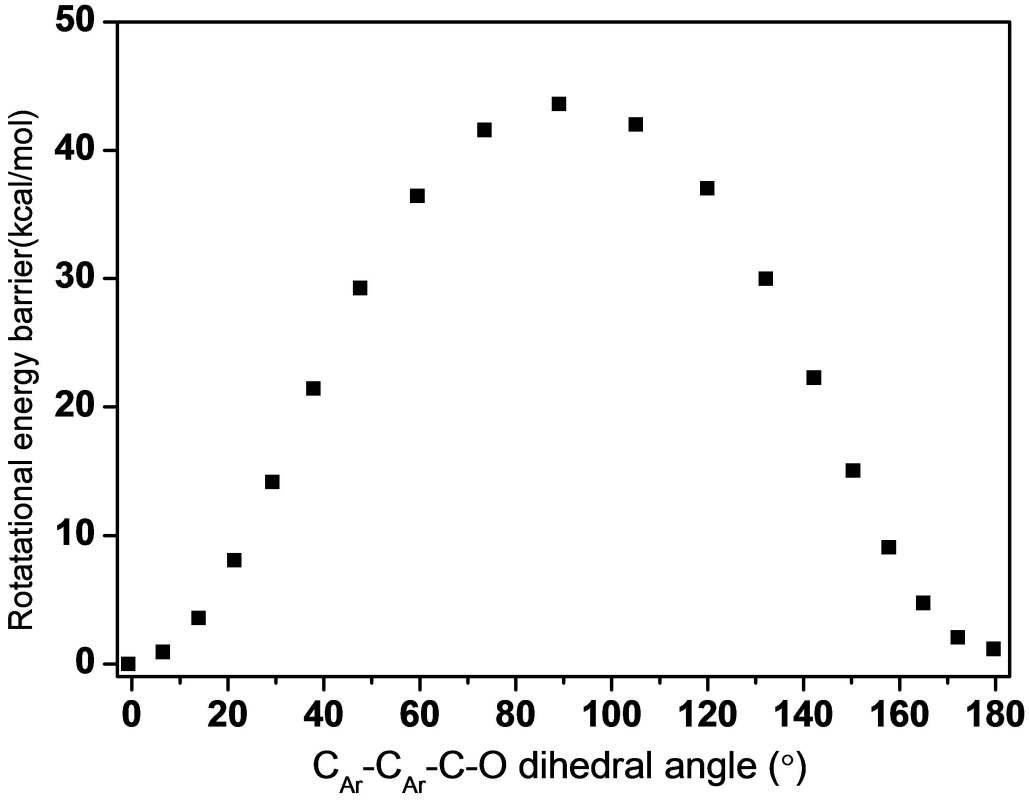

FIGURE C.4: Rotational energy barrier calculation results for $Zr_6O_4(OH)_4(COOH)_{11}(COOC_6H_5)$.

The model structure was geometry optimized and used as the starting conformation for energy surface scan calculation. Potential energy surfaces were constructed by varying one CAr-CAr-C-O dihedral angle 10° a step while allowing the remaining coordinates to relax.

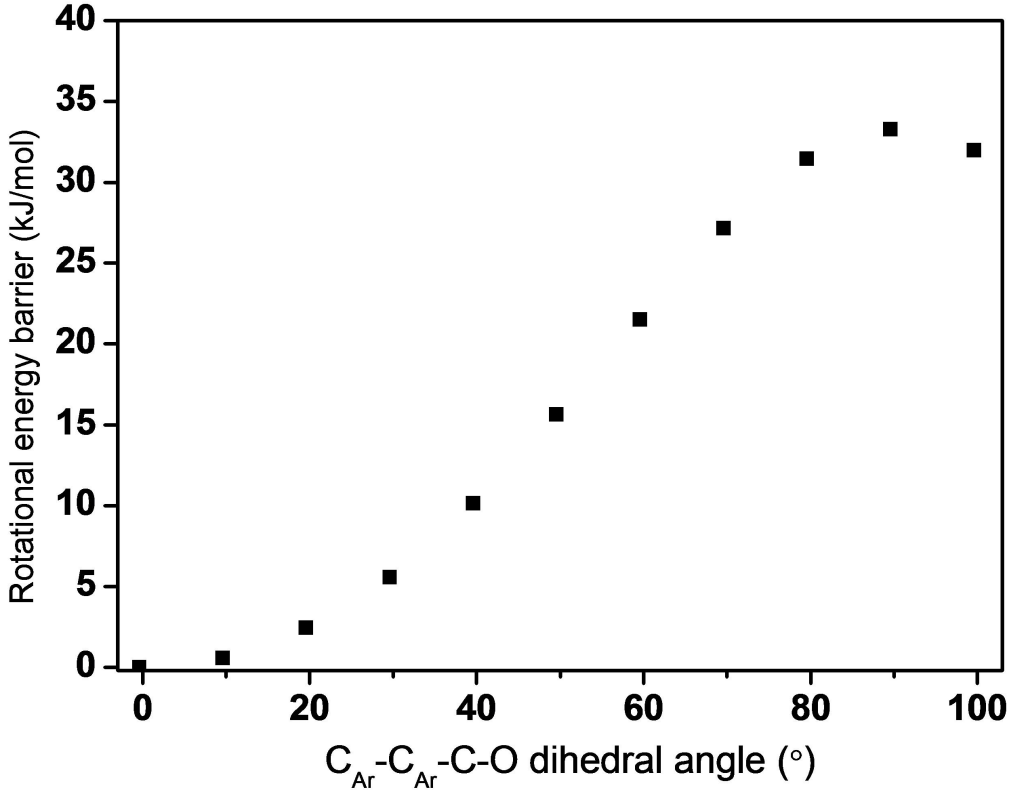

FIGURE C.5: Rotational energy barrier calculation results for $Zr_6O_4(OH)_4(COOH)_{11}(COOC_6H_4\text{-o-}CH_3)$.

C.3 NMR Measurements

The NMR measurements were performed on a Bruker Avance III spectrometer at 400 MHz ^{1}H Larmor frequency with a 4 mm Bruker double-resonance MAS probe, using $\pi/2$ pulse lengths of 3.5 μs for ^1H and 4.0 μs for ^{13}C under 5 kHz MAS. The UiO-66-$(CH_3)_2$ and UiO-66-Br data were collected on a Bruker Avance III spectrometer at 500 MHz ^1H Larmor frequency with a 3.2 mm Bruker triple-resonance MAS probe, using $\pi/2$ pulse lengths of 2.8 μs for ^1H and 4.0 μs for ^{13}C under 5.5 kHz and 6.5 kHz MAS, respectively to avoid overlap with spinning sidebands. Temperature calibrations were done with $PbNO_3$. For all samples, cross polarization times were kept under 1 ms to avoid the loss of magnetization due to T1 relaxation. Due to spectral overlap in certain cases, shorter CP times were used to filter out magnetization from non-CH bonded resonances. For UiO-66-$(CH_3)_2$ and UiO-66-Br it was kept to 500 μs, which was the shortest reasonable time for signal intensity. For UiO-66-$(OH)_2$, the aromatic CH and quaternary aromatic carbon are also

overlapped, but the rigid nature of this sample required a very short CP filter (< 100 μs depending on temperature) as can be seen in Figure C.6.

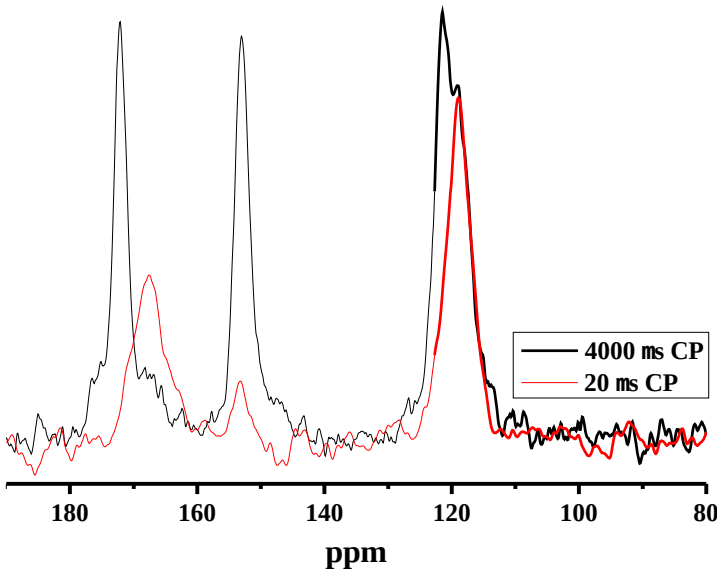

FIGURE C.6: ^{13}C CPMAS spectra of UiO-66-$(OH)_2$ employing long and short CP times to extract the CH resonance only for UiO-66-$(OH)_2$

A side-effect of such short CP times is the induction of inhomogeneous cross polarization effects distorting the DIPSHIFT curves, requiring the RODEO delay. For all other samples, the usual DIPSHIFT sequence without the RODEO period was employed. ^1H and ^{13}C assignments were previously reported for the samples [21]. We note that while the short CP times mostly select for CH bonded carbons, this process may not be completely selective and some small contributions from other carbons could artificially reduce the extracted dipolar coupling value. This is one reason why comparing the intermediate T2 regime is so important as it gives a secondary dynamic metric regardless of the absolute dipolar coupling value.

Bibliography

[1] Anatole Abragam. *Principles of Nuclear Magnetism*. Oxford: Oxford University Press, 1961.

[2] Vipin Agarwal et al. "De novo 3D structure determination from sub-milligram protein samples by solid-state 100 kHz MAS NMR spectroscopy". In: *Angewandte Chemie International Edition* 53.45 (Nov. 2014), pp. 12253–12256. ISSN: 15213773. DOI: 10.1002/anie.201405730. URL: http://doi.wiley.com/10.1002/anie.201405730.

[3] Lauren R. Agnew et al. "Continuous Crystallization of Paracetamol (Acetaminophen) Form II: Selective Access to a Metastable Solid Form". In: *Crystal Growth & Design* 17.5 (May 2017), pp. 2418–2427. ISSN: 1528-7483. DOI: 10.1021/acs.cgd.6b01831. URL: http://pubs.acs.org/doi/abs/10.1021/acs.cgd.6b01831.

[4] N. Al-Zoubi, I. Nikolakakis, and S. Malamataris. "Crystallization conditions and formation of orthorhombic paracetamol from ethanolic solution". In: *Journal of Pharmacy and Pharmacology* 54.3 (Mar. 2002), pp. 325–333. ISSN: 00223573. DOI: 10.1211/0022357021778565. URL: http://doi.wiley.com/10.1211/0022357021778565.

[5] Gordon L. Amidon et al. "A Theoretical Basis for a Biopharmaceutic Drug Classification: The Correlation of in Vitro Drug Product Dissolution and in Vivo Bioavailability". In: *Pharmaceutical Research* 12.3 (1995), pp. 413–420. ISSN: 1573904X. DOI: 10.1023/A:1016212804288. arXiv: 0005074v1 [astro-ph].

[6] E. R. ANDREW, A. BRADBURY, and R. G. EADES. "Nuclear Magnetic Resonance Spectra from a Crystal rotated at High Speed". In: *Nature* 182.4650 (Dec. 1958), pp. 1659–1659. ISSN: 0028-0836. DOI: 10.1038/1821659a0. URL: http://www.nature.com/doifinder/10.1038/1821659a0.

[7] Sam Asami and Bernd Reif. "Proton-detected solid-state NMR spectroscopy at aliphatic sites: Application to crystalline systems". In: *Accounts of Chemical Research* 46.9 (Sept. 2013), pp. 2089–2097. ISSN: 00014842. DOI: 10.1021/ar400063y. URL: http://pubs.acs.org/doi/abs/10.1021/ar400063y.

[8] Mads Bak, Jimmy T Rasmussen, and N C Nielsen. "SIMPSON: a general simulation program for solid-state NMR spectroscopy." In: *Journal of Magnetic Resonance* 147.2 (2000), pp. 296–330. ISSN: 1090-7807. DOI: 10.1006/jmre.2000.2179. URL: http://www.ncbi.nlm.nih.gov/pubmed/11097821.

[9] Vytautas Balevicius and K Aidas. "Temperature dependence of 1H and 17O NMR shifts of water: Entropy effect". In: *Applied Magnetic Resonance* 32.3 (2007), pp. 363–376. ISSN: 09379347. DOI: 10.1007/s00723-007-0021-4.

[10] Elisa Barea, Fabrizio Turra, and Jorge A. Rodriguez Navarro. "Separation and Purification of Gases by MOFs". In: *Metal-Organic Frameworks*. Weinheim, Germany: Wiley-VCH Verlag GmbH & Co. KGaA, July 2011, pp. 69–97. ISBN: 9783527635856. DOI: 10.1002/9783527635856.ch4. URL: http://doi.wiley.com/10.1002/9783527635856.ch4.

[11] Axel D. Becke. "Density-functional thermochemistry. III. The role of exact exchange". In: *The Journal of Chemical Physics* 98.7 (Apr. 1993), pp. 5648–5652. ISSN: 0021-9606. DOI: 10.1063/1.464913. URL: http://aip.scitation.org/doi/10.1063/1.464913.

[12] A Cadiau et al. "A metal-organic framework-based splitter for separating propylene from propane." In: *Science (New York, N.Y.)* 353.6295 (July 2016), pp. 137–40. ISSN: 1095-9203. DOI: 10.1126/science.aaf6323. URL: http://www.ncbi.nlm.nih.gov/pubmed/27387945.

[13] Jasmina Hafizovic Cavka et al. "A new zirconium inorganic building brick forming metal organic frameworks with exceptional stability". In: *Journal of the American Chemical Society* 130.42 (2008), pp. 13850–13851. ISSN: 00027863. DOI: 10.1021/ja8057953. URL: https://s3.amazonaws.com/academia.edu.documents/44630692/A_new_zirconium_inorganic_building_brick20160411-7676-1i0khxc.pdf?AWSAccessKeyId=AKIAIWOWYYGZ2Y53UL3A&Expires=1508860319&Signature=8s0%2F8A1ka38nVUwnMQmbHRp2pr8%3D&response-content-disposition=inlin.

[14] Ze Chang et al. "Flexible metal-organic frameworks: Recent advances and potential applications". In: *Advanced Materials* 27.36 (2015), pp. 5432–5441. ISSN: 15214095. DOI: 10.1002/adma.201501523.

[15] Heather D. Clarke et al. "Structure-stability relationships in cocrystal hydrates: Does the promiscuity of water make crystalline hydrates the nemesis of crystal engineering?" In: *Crystal Growth and Design* 10.5 (2010), pp. 2152–2167. ISSN: 15287483. DOI: 10.1021/cg901345u.

[16] Angiolina Comotti et al. "Fast molecular rotor dynamics modulated by guest inclusion in a highly organized nanoporous organosilica". In: *Angewandte Chemie - International Edition* 49.10 (2010), pp. 1760–1764. ISSN: 14337851. DOI: 10.1002/anie.200906255.

[17] François Xavier Coudert. "Responsive metal-organic frameworks and framework materials: Under pressure, taking the heat, in the spotlight, with friends". In: *Chemistry of Materials* 27.6 (2015), pp. 1905–1916. ISSN: 15205002. DOI: 10.1021/acs.chemmater.5b00046.

[18] Eduardo Ribeiro deAzevedo et al. “Intermediate motions as studied by solid-state separated local field NMR experiments”. In: *The Journal of Chemical Physics* 128.10 (Mar. 2008), p. 104505. ISSN: 0021-9606. DOI: 10.1063/1.2831798. URL: http://aip.scitation.org/doi/10.1063/1.2831798.

[19] Thomas Delmas et al. “Crystallisation of the orthorhombic form of acetaminophen: Combined effect of surface topography and chemistry”. In: *Powder Technology* 236 (Feb. 2013), pp. 24–29. ISSN: 00325910. DOI: 10.1016/j.powtec.2012.05.053. URL: http://linkinghub.elsevier.com/retrieve/pii/S0032591012003804.

[20] Michaël Deschamps. “Ultrafast Magic Angle Spinning Nuclear Magnetic Resonance”. In: *Annual Reports on NMR Spectroscopy* 81 (Jan. 2014), pp. 109–144. ISSN: 0066-4103. DOI: 10.1016/B978-0-12-800185-1.00003-6. URL: https://www.sciencedirect.com/science/article/pii/B9780128001851000036.

[21] Sabine Devautour-Vinot et al. “Structure and dynamics of the functionalized MOF type UiO-66(Zr): NMR and dielectric relaxation spectroscopies coupled with DFT calculations”. In: *Chemistry of Materials* 24.11 (2012), pp. 2168–2177. ISSN: 08974756. DOI: 10.1021/cm300863c.

[22] Robert Ditchfield. “Self-consistent perturbation theory of diamagnetism”. In: *Molecular Physics* 27.4 (Apr. 1974), pp. 789–807. ISSN: 0026-8976. DOI: 10.1080/00268977400100711. URL: http://www.tandfonline.com/doi/abs/10.1080/00268977400100711.

[23] Jovan Lj. Dragelj et al. “C–H/O Interactions of Aromatic CH Donors within Proteins: A Crystallographic Study”. In: *Crystal Growth and Design* 16.4 (Apr. 2016), pp. 1948–1957. ISSN: 1528-7483. DOI: 10.1021/acs.cgd.5b01543. URL: http://pubs.acs.org/doi/abs/10.1021/acs.cgd.5b01543.

[24] Jovan Lj Dragelj et al. “Crystallographic and ab initio study of pyridine CH–O interactions: linearity of the interactions and influence of pyridine classical hydrogen bonds”. In: *CrystEngComm* 15 (2013), p. 10481. DOI: 10.1039/c3ce40759d. URL: www.rsc.org/crystengcomm.

[25] Melinda J. Duer. “Dipolar coupling. Its measurement and uses”. In: *Solid-State NMR Spectroscopy Principles and Applications*. Oxford, UK: Blackwell Science Ltd, Dec. 2002, pp. 111–178. ISBN: 9780470999394. DOI: 10.1002/9780470999394.ch3. URL: http://doi.wiley.com/10.1002/9780470999394.ch3.

[26] Richard R. Ernst, Geoffrey Bodenhausen, and Alexander Wokaun. *Principles of Nuclear Magnetic Resonance in One and Two Dimensions*. Oxford: Oxford Universtiy Press, 1997.

[27] Gérard Férey. “Hybrid porous solids: past, present, future”. In: *Chem. Soc. Rev.* 37.1 (2008), pp. 191–214. ISSN: 0306-0012. DOI: 10.1039/B618320B. URL: http://xlink.rsc.org/?DOI=B618320B.

[28] Gérard Férey and Christian Serre. “Large breathing effects in three-dimensional porous hybrid matter: facts, analyses, rules and consequences”. In: *Chemical Society Reviews* 38.5 (Apr. 2009), p. 1380. ISSN: 0306-0012. DOI: 10.1039/b804302g. URL: http://xlink.rsc.org/?DOI=b804302g.

[29] Gérard Férey and Christian Serre. “Large breathing effects in three-dimensional porous hybrid matter: facts, analyses, rules and consequences”. In: *Chemical Society Reviews* 38.5 (2009), p. 1380. ISSN: 0306-0012. DOI: 10.1039/b804302g. URL: http://xlink.rsc.org/?DOI=b804302g.

[30] Pascal Fricke et al. “Backbone assignment of perdeuterated proteins by solid-state NMR using proton detection and ultrafast magic-angle spinning”. In: *Nature Protocols* 12.4 (2017), pp. 764–782. ISSN: 1754-2189. DOI: 10.1038/nprot.2016.190. URL: http://www.nature.com/doifinder/10.1038/nprot.2016.190.

[31] M. J. Frisch et al. *Gaussian 09*. 2009. DOI: 111.

[32] Katharina Fucke and Jonathan W. Steed. “X-ray and Neutron Diffraction in the Study of Organic Crystalline Hydrates”. In: *Water* 2.3 (2010), pp. 333–350. ISSN: 2073-4441. DOI: 10.3390/w2030333. URL: http://www.mdpi.com/2073-4441/2/3/333/.

[33] B. C. (Bernard C.) Gerstein and C. R. Dybowski. *Transient techniques in NMR of solids : an introduction to theory and practice*. Academic Press, 1985, p. 295. ISBN: 0122811801. URL: https://inis.iaea.org/search/search.aspx?orig_q=RN:19080225.

[34] Amy L. Gillon et al. “Hydration in molecular crystals - A Cambridge Structural Database analysis”. In: *Crystal Growth and Design* 3.5 (2003), pp. 663–673. ISSN: 15287483. DOI: 10.1021/cg034088e.

[35] D. Giron et al. “Solid state characterizations of pharmaceutical hydrates”. In: *Journal of Thermal Analysis and Calorimetry* 68.2 (2002), pp. 453–465. ISSN: 14182874. DOI: 10.1023/A:1016031517430.

[36] Stephanie L Gould et al. “The Amphidynamic Character of Crystalline MOF-5 : Rotational Dynamics in a Free-Volume Environment”. In: *Journal of the American Chemical Society* 130.Figure 3 (2008), pp. 3246–3247. DOI: 10.1021/ja077122c.

[37] Colin R. Groom et al. “The Cambridge Structural Database”. In: *Acta Crystallographica Section B Structural Science, Crystal Engineering and Materials* 72.2 (Apr. 2016), pp. 171–179. ISSN: 2052-5206. DOI: 10.1107/S2052520616003954. URL: http://scripts.iucr.org/cgi-bin/paper?S2052520616003954.

[38] Kevin Hendrickx et al. “Understanding Intrinsic Light Absorption Properties of UiO-66 Frameworks: A Combined Theoretical and Experimental Study”. In: *Inorganic Chemistry* 54.22 (Nov. 2015), pp. 10701–10710. ISSN: 1520510X. DOI: 10.1021/acs.inorgchem.5b01593. URL: http://pubs.acs.org/doi/10.1021/acs.inorgchem.5b01593.

[39] Jacek W. Hennel and Jacek Klinowski. “Magic-Angle Spinning: a Historical Perspective”. In: *New Techniques in Solid-State NMR*. Ed. by Jacek Klinowski. Berlin, Heidelberg: Springer Berlin Heidelberg, 2005, pp. 1–14. ISBN: 978-3-540-31473-8. DOI: 10.1007/b98646. URL: https://doi.org/10.1007/b98646.

[40] R. K. Hester et al. “Separated Local Field Spectra in NMR: Determination of Structure of Solids”. In: *Physical Review Letters* 36.18 (May 1976), pp. 1081–1083. ISSN: 0031-9007. DOI: 10.1103/PhysRevLett.36.1081. URL: https://link.aps.org/doi/10.1103/PhysRevLett.36.1081.

[41] Jérôme Hirschinger. “A simple analytical model to describe dynamic magic-angle spinning experiments”. In: *Concepts in Magnetic Resonance Part A* 28A.5 (Sept. 2006), pp. 307–320. ISSN: 1546-6086. DOI: 10.1002/cmr.a.20064. URL: http://doi.wiley.com/10.1002/cmr.a.20064.

[42] M Hong, J D Gross, and R G Griffin. “Site-resolved determination of peptide torsion angle phi from the relative orientations of backbone N-H and C-H bonds by solid-state NMR”. In: *Journal of Physical Chemistry B* 101.30 (1997), pp. 5869–5874. ISSN: 1520-6106. DOI: 10.1021/jp970887u.

[43] Patricia Horcajada et al. “How linker’s modification controls swelling properties of highly flexible iron(III) dicarboxylates MIL-88”. In: *Journal of the American Chemical Society* 133.44 (2011), pp. 17839–17847. ISSN: 00027863. DOI: 10.1021/ja206936e.

[44] Satoshi Horike, Satoru Shimomura, and Susumu Kitagawa. *Soft porous crystals*. 2009. DOI: 10.1038/nchem.444.

[45] Satoshi Horike et al. “Dynamic Motion of Building Blocks in Porous Coordination Polymers”. In: *Angewandte Chemie International Edition* 45.43 (Nov. 2006), pp. 7226–7230. ISSN: 14337851. DOI: 10.1002/anie.200603196. URL: http://doi.wiley.com/10.1002/anie.200603196.

[46] Guangjin Hou et al. “A magic-angle-spinning NMR spectroscopy method for the site-specific measurement of proton chemical-shift anisotropy in biological and organic solids”. In: *Israel Journal of Chemistry* 54.1-2 (2014), pp. 171–183. ISSN: 18695868. DOI: 10.1002/ijch.201300099.

[47] Yuting Huang et al. “Enhanced stability and CO2 affinity of a UiO-66 type metal–organic framework decorated with dimethyl groups”. In: *Dalton Transactions* 41.31 (July 2012), p. 9283. ISSN: 1477-9226. DOI: 10.1039/c2dt30950e. URL: http://xlink.rsc.org/?DOI=c2dt30950e.

[48] Lourdes Infantes, László Fábián, and W. D. Sam Motherwell. "Organic crystal hydrates: what are the important factors for formation". In: *CrystEngComm* 9.1 (2007), pp. 65–71. ISSN: 1466-8033. DOI: 10.1039/b612529h.

[49] Munehiro Inukai et al. "Control of Molecular Rotor Rotational Frequencies in Porous Coordination Polymers Using a Solid-Solution Approach". In: *Journal of the American Chemical Society* 137.38 (2015), pp. 12183–12186. ISSN: 15205126. DOI: 10.1021/jacs.5b05413.

[50] Mukul G. Jain et al. "Selective 1H– 1H Distance Restraints in Fully Protonated Proteins by Very Fast Magic-Angle Spinning Solid-State NMR". In: *The Journal of Physical Chemistry Letters* 8.11 (June 2017), pp. 2399–2405. ISSN: 1948-7185. DOI: 10.1021/acs.jpclett.7b00983. URL: http://pubs.acs.org/doi/abs/10.1021/acs.jpclett.7b00983.

[51] Maheswararao Karanam and Angshuman Roy Choudhury. "Structural landscape of pure enrofloxacin and its novel salts: Enhanced solubility for better pharmaceutical applicability". In: *Crystal Growth and Design* 13.4 (2013), pp. 1626–1637. ISSN: 15287483. DOI: 10.1021/cg301831s.

[52] Michael J. Katz et al. "A facile synthesis of UiO-66, UiO-67 and their derivatives". In: *Chemical Communications* 49.82 (Sept. 2013), p. 9449. ISSN: 1359-7345. DOI: 10.1039/c3cc46105j. URL: http://xlink.rsc.org/?DOI=c3cc46105j.

[53] Sukhvir Kaur Bhangu, Muthupandian Ashokkumar, and Judy Lee. "Ultrasound Assisted Crystallization of Paracetamol: Crystal Size Distribution and Polymorph Control". In: *Crystal Growth and Design* 16.4 (Apr. 2016), pp. 1934–1941. ISSN: 15287505. DOI: 10.1021/acs.cgd.5b01470. URL: http://pubs.acs.org/doi/abs/10.1021/acs.cgd.5b01470.

[54] Kortney M. Kersten and Adam J. Matzger. "Improved pharmacokinetics of mercaptopurine afforded by a thermally robust hemihydrate". In: *Chem. Commun.* 52.30 (2016), pp. 5281–5284. ISSN: 1359-7345. DOI: 10.1039/C6CC00424E. URL: http://xlink.rsc.org/?DOI=C6CC00424E.

[55] Rajendra K. Khankari and David J.W. Grant. "Pharmaceutical hydrates". In: *Thermochimica Acta* 248.C (Jan. 1995), pp. 61–79. ISSN: 00406031. DOI: 10.1016/0040-6031(94)01952-D. URL: http://linkinghub.elsevier.com/retrieve/pii/004060319401952D.

[56] Alexander E. Khudozhitkov et al. "Metal-Cation-Independent Dynamics of Phenylene Ring in Microporous MOFs: A ² H Solid-State NMR Study". In: *The Journal of Physical Chemistry C* 119.50 (Dec. 2015), pp. 28038–28045. ISSN: 1932-7447. DOI: 10.1021/acs.jpcc.5b09435. URL: http://pubs.acs.org/doi/10.1021/acs.jpcc.5b09435.

[57] Mikhail Kibalchenko et al. "Distinguishing hydrogen bonding networks in α-d-galactose using NMR experiments and first principles calculations". In: *Chemical Physics Letters* 498.4-6 (2010), pp. 270–276. ISSN: 00092614. DOI: 10.1016/j.cplett.2010.08.077. URL: http://www.sciencedirect.com/science/article/pii/S0009261410011838.

[58] D. I. Kolokolov et al. “Probing the dynamics of the porous Zr terephthalate UiO-66 framework using 2H NMR and neutron scattering”. In: *Journal of Physical Chemistry C* 116.22 (June 2012), pp. 12131–12136. ISSN: 19327447. DOI: 10.1021/jp3029193. URL: http://pubs.acs.org/doi/abs/10.1021/jp3029193.

[59] Daniil I. Kolokolov, Alexander G. Stepanov, and Hervé Jobic. “Guest controlled rotational dynamics of terephthalate phenylenes in metal-organic framework MIL-53(Al): Effect of different xylene loadings”. In: *Journal of Physical Chemistry C* 118.29 (2014). ISSN: 19327455. DOI: 10.1021/jp506010p.

[60] Daniil I Kolokolov et al. “Dynamics of benzene rings in MIL-53(Cr) and MIL-47(V) frameworks studied by2H NMR spectroscopy”. In: *Angewandte Chemie - International Edition* 49.28 (2010), pp. 4791–4794. ISSN: 14337851. DOI: 10.1002/anie.201001238.

[61] Ricardo Kurz et al. “Avoiding bias effects in NMR experiments for heteronuclear dipole-dipole coupling determinations: Principles and application to organic semiconductor materials”. In: *ChemPhysChem* 14.13 (2013), pp. 3146–3151. ISSN: 14394235. DOI: 10.1002/cphc.201300255.

[62] Chengteh Lee, Weitao Yang, and Robert G. Parr. “Development of the Colle-Salvetti correlation-energy formula into a functional of the electron density”. In: *Physical Review B* 37.2 (Jan. 1988), pp. 785–789. ISSN: 01631829. DOI: 10.1103/PhysRevB.37.785. URL: http://www.ncbi.nlm.nih.gov/pubmed/9944570.

[63] Moses Lee and Walter I. Goldburg. “Nuclear-magnetic-resonance line narrowing by a rotating rf field”. In: *Physical Review* 140.4A (Nov. 1965), A1261–A1271. ISSN: 0031899X. DOI: 10.1103/PhysRev.140.A1261. URL: https://link.aps.org/doi/10.1103/PhysRev.140.A1261.

[64] Malcolm H Levitt. “Symmetry-based pulse sequences in magic-angle spinning solid-state NMR”. In: *Encyclopedia of Nuclear Magnetic Resonance* 9 (2002), pp. 165–196. ISSN: 0931-7597. DOI: 10.1002/9780470034590. URL: http://eu.wiley.com/WileyCDA/WileyTitle/productCd-0471490822.html.

[65] I. J. Lowe. “Free Induction Decays of Rotating Solids”. In: *Physical Review Letters* 2.7 (Apr. 1959), pp. 285–287. ISSN: 0031-9007. DOI: 10.1103/PhysRevLett.2.285. URL: https://link.aps.org/doi/10.1103/PhysRevLett.2.285.

[66] Heinz Dieter Lutz. “Bonding and Structure of Water Molecules in Solid Hydrates. Correlation of Spectroscopic and Structural Data”. In: *Solid Materials*. Berlin, Heidelberg: Springer, 1988. Chap. Bonding an, pp. 97–125. DOI: 10.1007/3-540-18790-1{_}3.

[67] Nathalie Mahé et al. “Solid-state properties and dehydration behavior of the active pharmaceutical ingredient potassium guaiacol-4-sulfonate”. In: *Crystal Growth and Design* 13.7 (2013), pp. 3028–3035. ISSN: 15287483. DOI: 10.1021/cg400427v.

[68] Vladimir G. Malkin et al. “Solvent Effect on the NMR Chemical Shieldings in Water Calculated by a Combination of Molecular Dynamics and Density Functional Theory”. In: *Chemistry - A European Journal* 2.4 (Apr. 1996), pp. 452–457. ISSN: 09476539. DOI: 10.1002/chem.19960020415. URL: http://doi.wiley.com/10.1002/chem.19960020415.

[69] M. Matti Maricq and J. S. Waugh. “NMR in rotating solids”. In: *The Journal of Chemical Physics* (1979). ISSN: 00219606. DOI: 10.1063/1.437915.

[70] Michael. Mehring. *Principles of High Resolution NMR in Solids*. Springer Berlin Heidelberg, 1983. ISBN: 9783642687587.

[71] G. Metz, X.L. Wu, and S.O. Smith. “Ramped-Amplitude Cross Polarization in Magic-Angle-Spinning NMR”. In: *Journal of Magnetic Resonance, Series A* 110.2 (1994), pp. 219–227. ISSN: 10641858. DOI: 10.1006/jmra.1994.1208. URL: http://www.sciencedirect.com/science?_ob=ArticleListURL&_method=list&_ArticleListID=-1211974141&_sort=r&_st=13&view=c&md5=247a4f3b31993d4c9864e0e2c4bc6b7b&searchtype=ahttp://www.sciencedirect.com/science/article/pii/S1064185884712083%5Cnhttp://linkinghub.

[72] Habeeba K. Miah et al. “1H CSA parameters by ultrafast MAS NMR: Measurement and applications to structure refinement”. In: *Solid State Nuclear Magnetic Resonance* (Feb. 2017). ISSN: 09262040. DOI: 10.1016/j.ssnmr.2017.02.002. URL: http://linkinghub.elsevier.com/retrieve/pii/S0926204016301515.

[73] Habeeba K. Miah et al. “Measuring proton shift tensors with ultrafast MAS NMR”. In: *Journal of Magnetic Resonance* 235 (2013), pp. 1–5. ISSN: 10907807. DOI: 10.1016/j.jmr.2013.07.005.

[74] M. A. Mikhailenko. “Growth of large single crystals of the orthorhombic paracetamol”. In: *Journal of Crystal Growth* 265.3-4 (May 2004), pp. 616–618. ISSN: 00220248. DOI: 10.1016/j.jcrysgro.2004.02.091. URL: http://linkinghub.elsevier.com/retrieve/pii/S0022024804002684.

[75] Katie R. Mitchell-Koch and Adam J. Matzger. “Evaluating computational predictions of the relative stabilities of polymorphic pharmaceuticals”. In: *Journal of Pharmaceutical Sciences* 97.6 (2008), pp. 2121–2129. ISSN: 00223549. DOI: 10.1002/jps.21127.

[76] Florian Moreau et al. “Tailoring porosity and rotational dynamics in a series of octacarboxylate metal-organic frameworks.” In: *Proceedings of the National Academy of Sciences of the United States of America* 114.12 (Mar. 2017), pp. 3056–3061. ISSN: 1091-6490. DOI: 10.1073/pnas.1615172114. URL: http://www.ncbi.nlm.nih.gov/pubmed/28280097http://www.pubmedcentral.nih.gov/articlerender.fcgi?artid=PMC5373404.

[77] Kenneth R. Morris and Nair Rodriguez-Hornedo. "Hydrates". In: *Encyclopedia of Pharmaceutical Technology*. Ed. by James Swarbrick and James C Boylan. New York: Marcel Dekker Inc., 1993, pp. 393–440.

[78] M G Munowitz et al. "Two-Dimensional Rotational Spin-Echo Nuclear Magnetic Resonance in Solids: Correlation of Chemical Shift and Dipolar Interactions". In: *Journal of the American Chemical Society* 103.10 (1981), pp. 2529–2533. ISSN: 15205126. DOI: 10.1021/ja00400a007.

[79] Thi Nhat Phuong Nguyen and Kwang Joo Kim. "Transformation of monohydrate into anhydrous form of risedronate monosodium in methanol-water mixture". In: *Industrial and Engineering Chemistry Research* 49.10 (2010), pp. 4842–4849. ISSN: 08885885. DOI: 10.1021/ie901677n.

[80] Gary Nichols and Christopher S. Frampton. "Physicochemical characterization of the orthorhombic polymorph of paracetamol crystallized from solution". In: *Journal of Pharmaceutical Sciences* 87.6 (June 1998), pp. 684–693. ISSN: 00223549. DOI: 10.1021/js970483d. URL: http://linkinghub.elsevier.com/retrieve/pii/S002235491550590X.

[81] Yusuke Nishiyama. "Fast magic-angle sample spinning solid-state NMR at 60–100 kHz for natural abundance samples". In: *Solid State Nuclear Magnetic Resonance* 78 (2016), pp. 24–36. DOI: 10.1016/j.ssnmr.2016.06.002.

[82] Manoj Kumar Pandey and Yusuke Nishiyama. "Determination of NH proton chemical shift anisotropy with 14N-1H heteronuclear decoupling using ultrafast magic angle spinning solid-state NMR". In: *Journal of Magnetic Resonance* 261 (2015), pp. 133–140. ISSN: 10960856. DOI: 10.1016/j.jmr.2015.10.015.

[83] Manoj Kumar Pandey and Yusuke Nishiyama. "Determination of relative orientation between 1H CSA tensors from a 3D solid-state NMR experiment mediated through 1H/1H RFDR mixing under ultrafast MAS". In: *Solid State Nuclear Magnetic Resonance* 70 (2015), pp. 15–20. ISSN: 09262040. DOI: 10.1016/j.ssnmr.2015.05.001. URL: http://dx.doi.org/10.1016/j.jmr.2015.06.012.

[84] Manoj Kumar Pandey et al. "Composite-180° pulse-based symmetry sequences to recouple proton chemical shift anisotropy tensors under ultrafast MAS solid-state NMR spectroscopy". In: *Journal of Magnetic Resonance* 250 (2015), pp. 45–54. ISSN: 10960856. DOI: 10.1016/j.jmr.2014.11.002.

[85] Laura L. Parker, Andrew R. Houk, and Jan H. Jensen. "Cooperative hydrogen bonding effects are key determinants of backbone amide proton chemical shifts in proteins". In: *Journal of the American Chemical Society* 128.30 (2006), pp. 9863–9872. ISSN: 00027863. DOI: 10.1021/ja0617901.

[86] Bernd G Pfrommer, Francesco Mauri, and Steven G Louie. "NMR Chemical Shifts of Ice and Liquid Water: The Effects of Condensation". In: *Jounal of American Chemical Society* 122 (2000), pp. 123–129. ISSN: 00027863. DOI: 10.1021/ja991961k.

[87] Jésus Raya et al. "Chemical shift powder spectra obtained by using ROtor-Directed Exchange of Orientations Cross-Polarization (RODEO-CP)". In: *Chemical Physics Letters* 508.1-3 (2011), pp. 155–164. ISSN: 00092614. DOI: 10.1016/j.cplett.2011.04.013.

[88] W-K. Rhim, A. Pines, and J. S. Waugh. "Time-Reversal Experiments in Dipolar-Coupled Spin Systems". In: *Physical Review B* 3.3 (Feb. 1971), pp. 684–696. ISSN: 0556-2805. DOI: 10.1103/PhysRevB.3.684. URL: https://link.aps.org/doi/10.1103/PhysRevB.3.684.

[89] J. Alberto Rodríguez-Velamazán et al. "A Switchable Molecular Rotator: Neutron Spectroscopy Study on a Polymeric Spin-Crossover Compound". In: *Journal of the American Chemical Society* 134.11 (Mar. 2012), pp. 5083–5089. ISSN: 0002-7863. DOI: 10.1021/ja206228n. URL: http://pubs.acs.org/doi/10.1021/ja206228n.

[90] Celeste McMichael Rohlfing, Leland C Allen, and Robert Ditchfield. "Proton chemical shift tensors in hydrogen-bonded dimers of RCOOH and ROH". In: *The Journal of Chemical Physics* 79.10 (1983), pp. 4958–4966. ISSN: 00219606. DOI: 10.1063/1.445589. URL: http://link.aip.org/link/JCPSA6/v79/i10/p4958/s1&Agg=doi.

[91] M. Sacchetti. "Thermodynamic Analysis of DSC Data for Acetaminophen Polymorphs". In: *Journal of Thermal Analysis and Calorimetry* 63.2 (2001), pp. 345–350. ISSN: 14182874. DOI: 10.1023/A:1010180123331. URL: http://link.springer.com/10.1023/A:1010180123331.

[92] Fabrice Salles et al. "Molecular dynamics simulations of breathing MOFs: Structural transformations of MIL-53(Cr) upon thermal activation and CO2 adsorption". In: *Angewandte Chemie - International Edition* 47.44 (Oct. 2008), pp. 8487–8491. ISSN: 14337851. DOI: 10.1002/anie.200803067. URL: http://doi.wiley.com/10.1002/anie.200803067.

[93] J. Schmidt et al. "Bulk chemical shifts in hydrogen-bonded systems from first-principles calculations and solid-state-NMR". In: *Journal of Physical Chemistry B* 110.46 (2006), pp. 23204–23210. DOI: 10.1021/jp0640732.

[94] K. Schmidt-Rohr and H. W. Spiess. *Multidimensional Solid-State NMR and Polymers*. Academic Press, 2012, pp. 1–478. ISBN: 9780126266306. DOI: 10.1016/C2009-0-21335-3.

[95] A. Schneemann et al. "Flexible metal–organic frameworks". In: *Chem. Soc. Rev.* 43.16 (2014), pp. 6062–6096. ISSN: 0306-0012. DOI: 10.1039/C4CS00101J. URL: http://xlink.rsc.org/?DOI=C4CS00101J.

[96] Wataru Setaka and Kentaro Yamaguchi. "Thermal modulation of birefringence observed in a crystalline molecular gyrotop." In: *Proceedings of the National Academy of Sciences of the United States of America* 109.24 (June 2012), pp. 9271–5. ISSN: 1091-6490. DOI: 10.1073/pnas.1114733109. URL: http://www.ncbi.nlm.nih.gov/pubmed/22645371http://www.pubmedcentral.nih.gov/articlerender.fcgi?artid=PMC3386105.

[97] Yugal Sharma et al. "An Ab initio study of amide proton shift tensor dependence on local protein structure". In: *Journal of the American Chemical Society* 124.2 (2002), pp. 327–335. ISSN: 00027863. DOI: 10.1021/ja016859d.

[98] A. G. Slater and A. I. Cooper. "Function-led design of new porous materials". In: *Science* 348.6238 (2015), p. 988. ISSN: 0036-8075. DOI: 10.1126/science.aaa8075. URL: http://www.sciencemag.org/content/348/6238/aaa8075.full.html.

[99] Jan Stanek et al. "NMR Spectroscopic Assignment of Backbone and Side-Chain Protons in Fully Protonated Proteins: Microcrystals, Sedimented Assemblies, and Amyloid Fibrils". In: *Angewandte Chemie - International Edition* 55.50 (Dec. 2016), pp. 15504–15509. ISSN: 15213773. DOI: 10.1002/anie.201607084. URL: http://doi.wiley.com/10.1002/anie.201607084.

[100] Thomas Steiner. "The Hydrogen Bond in the Solid State". In: *Angew. Chem. Int. Ed.* 41 (2002), pp. 48–76. ISSN: 15213773. DOI: 10.1002/1521-3773(20020104)41:1<48::AID-ANIE48>3.0.CO;2-U. URL: http://www3.interscience.wiley.com/journal/89012417/abstract.

[101] Andre Sutrisno and Yining Huang. "Solid-state NMR: A powerful tool for characterization of metal-organic frameworks". In: *Solid State Nuclear Magnetic Resonance* 49-50 (2013), pp. 1–11. ISSN: 09262040. DOI: 10.1016/j.ssnmr.2012.09.003. URL: http://dx.doi.org/10.1016/j.ssnmr.2012.09.003.

[102] Yu Suzuki et al. "Intra- and intermolecular effects on 1H chemical shifts in a silk model peptide determined by high-field solid state 1H NMR and empirical calculations". In: *Journal of Physical Chemistry B* 113.29 (2009), pp. 9756–9761. ISSN: 15206106. DOI: 10.1021/jp903020p.

[103] Alok S. Tayi et al. "Supramolecular ferroelectrics". In: *Nature Chemistry* 7.4 (Mar. 2015), pp. 281–294. ISSN: 1755-4330. DOI: 10.1038/nchem.2206. URL: http://www.nature.com/doifinder/10.1038/nchem.2206.

[104] Robin Taylor. "It Isn't, It Is: The C-H···X (X = O, N, F, Cl) Interaction Really Is Significant in Crystal Packing". In: *Crystal Growth and Design* 16.8 (2016), pp. 4165–4168. ISSN: 15287505. DOI: 10.1021/acs.cgd.6b00736.

[105] Kent R. Thurber and Robert Tycko. "Measurement of sample temperatures under magic-angle spinning from the chemical shift and spin-lattice relaxation rate of 79Br in KBr powder". In: *Journal of Magnetic Resonance* 196.1 (Jan. 2009), pp. 84–87. ISSN: 10907807. DOI: 10.1016/j.jmr.2008.09.019. URL: http://www.sciencedirect.com/science/article/pii/S1090780708003091.

[106] Fang Tian et al. "Factors affecting crystallization of hydrates". In: *Journal of Pharmacy and Pharmacology* 62.11 (2010), pp. 1534–1546. ISSN: 00223573. DOI: 10.1111/j.2042-7158.2010.01186.x.

[107] Nico Tjandra and Ad Bax. "Solution NMR measurement of amide proton chemical shift anisotropy in 15N-enriched proteins. Correlation with hydrogen bond length". In: *Journal of the American Chemical Society* 119.34 (1997), pp. 8076–8082. ISSN: 00027863. DOI: 10.1021/ja970876e. URL: http://pubs.acs.org/doi/abs/10.1021/ja970876e.

[108] P. Van Hecke et al. "Determination of the proton chemical shielding tensor in anhydrous α-oxalic acid by multiple pulse NMR". In: *The Journal of Chemical Physics* 60.4 (Feb. 1974), pp. 1668–1670. ISSN: 0021-9606. DOI: 10.1063/1.1681244. URL: http://aip.scitation.org/doi/10.1063/1.1681244.

[109] Narayan Variankaval et al. "Water activity-mediated control of crystalline phases of an active pharmaceutical ingredient". In: *Organic Process Research and Development* 11.2 (2007), pp. 229–236. ISSN: 10836160. DOI: 10.1021/op600277t.

[110] Dusan Z Veljkovi, Goran V Janjic, and Snezana D Zaric. "Are C–H/O interactions linear? The case of aromatic CH donors". In: *CrystEngComm* 13 (2011), p. 5005. ISSN: 1466-8033. DOI: 10.1039/c1ce05065f.

[111] Krista S. Walton and Randall Q. Snurr. "Applicability of the BET method for determining surface areas of microporous metal-organic frameworks". In: *Journal of the American Chemical Society* 129.27 (2007), pp. 8552–8556. ISSN: 00027863. DOI: 10.1021/ja071174k. URL: http://pubs.acs.org/doi/abs/10.1021%2Fja071174k.

[112] J. S. Waugh, L. M. Huber, and U. Haeberlen. "Approach to High-Resolution nmr in Solids". In: *Physical Review Letters* 20.5 (Jan. 1968), pp. 180–182. ISSN: 0031-9007. DOI: 10.1103/PhysRevLett.20.180. URL: https://link.aps.org/doi/10.1103/PhysRevLett.20.180.

[113] Lik Hong Wee et al. "Metal-Organic Frameworks as Catalysts for Organic Reactions". In: *Metal-Organic Frameworks*. Weinheim, Germany: Wiley-VCH Verlag GmbH & Co. KGaA, July 2011, pp. 191–212. ISBN: 9783527635856. DOI: 10.1002/9783527635856.ch9. URL: http://doi.wiley.com/10.1002/9783527635856.ch9.

[114] Krzysztof Wolinski, James F. Hinton, and Peter Pulay. "Efficient implementation of the gauge-independent atomic orbital method for NMR chemical shift calculations". In: *Journal of the American Chemical Society* 112.23 (Nov. 1990), pp. 8251–8260. ISSN: 0002-7863. DOI: 10.1021/ja00179a005. URL: http://pubs.acs.org/doi/abs/10.1021/ja00179a005.

[115] C. H. Wu et al. "Simultaneous Characterization of the Amide 1H Chemical Shift, 1H-15N Dipolar, and 15N Chemical Shift Interaction Tensors in a Peptide Bond by Three-Dimensional Solid-State NMR Spectroscopy". In: *Journal of the American Chemical Society* 117.22 (June 1995), pp. 6148–6149. ISSN: 0002-7863. DOI: 10.1021/ja00127a039. URL: http://pubs.acs.org/doi/abs/10.1021/ja00127a039.

[116] Gang Wu, Christopher J. Freure, and Elodie Verdurand. "Proton chemical shift tensors and hydrogen bond geometry: A 1H-2H dipolar NMR study of the water molecule in crystalline hydrates". In: *Journal of the American Chemical Society* 120.50 (1998), pp. 13187–13193. ISSN: 00027863. DOI: 10.1021/ja983126t. URL: http://pubs.acs.org/doi/abs/10.1021/ja983126t.

[117] Omar M. Yaghi et al. "Reticular synthesis and the design of new materials". In: *Nature* 423.6941 (June 2003), pp. 705–714. ISSN: 00280836. DOI: 10.1038/nature01650. URL: http://www.nature.com/doifinder/10.1038/nature01650.

[118] Rongchun Zhang, Kamal H. Mroue, and Ayyalusamy Ramamoorthy. "Proton chemical shift tensors determined by 3D ultrafast MAS double-quantum NMR spectroscopy". In: *Journal of Chemical Physics* 143.14 (Oct. 2015), p. 144201. ISSN: 00219606. DOI: 10.1063/1.4933114. URL: http://scitation.aip.org/content/aip/journal/jcp/143/14/10.1063/1.4933114.

[119] Donghua H. Zhou and Chad M. Rienstra. "Rapid Analysis of Organic Compounds by Proton-Detected Heteronuclear Correlation NMR Spectroscopy with 40kHz Magic-Angle Spinning". In: *Angewandte Chemie International Edition* 47.38 (Sept. 2008), pp. 7328–7331. ISSN: 14337851. DOI: 10.1002/anie.200802108. URL: http://doi.wiley.com/10.1002/anie.200802108.